UNIVERSITÀ DELLA CALABRIA

**Università della Calabria**

Dipartimento di Fisica

**Dottorato di Ricerca in**

Scienze e Tecnologie Fisiche, Chimiche e dei Materiali

**CICLO**

XXXIII

# The complex structure of astrophysical plasmas: turbulence, coherent structures and particle transport

**Settore Scientifico Disciplinare FIS/05**

**Coordinatore:** Ch.ma Prof.ssa Gabriella Cipparrone

Firma oscurata in base alle linee guida del Garante della privacy

**Supervisore:** Ch.mo Prof. Sergio Servidio

Firma oscurata in base alle linee guida del Garante della privacy

**Supervisore:** Dott.ssa Antonella Greco

Firma oscurata in base alle linee guida del Garante della privacy

**Dottorando:** Dott. Francesco Pecora

Firma oscurata in base alle linee guida del Garante della privacy

# Abstract

Plasma turbulence is a ubiquitous phenomenon that characterizes the universe. From black holes to fusion devices, complex plasma effects are present to a variety of scales. In this PhD thesis, some relevant aspects of astrophysical plasmas will be covered, tackling long-standing problems via synergistic, different approaches. We will make use of (I) plasma theory, (II) numerical simulations, and (III) space data analysis. Theoretical models are necessary to understand the basic ingredients of interesting phenomena. Though sometimes, the mathematical approach becomes either too difficult or requires too strong approximations to be carried on. The invaluable tool of numerical simulations pushed forward our understanding of plasma turbulence, as it is our only way to directly observe it. Simulations also allow preparing ad-hoc experiments to test analytical theories. Finally, observations – either Earth-based or in-situ – are the playground where analytical theories and numerical simulations face reality.

During my itinerary, I used all the methods above to approach different plasma turbulence problems at very small (kinetic) and very large (magnetohydrodynamics) scales. At kinetic scales, I investigated the problems of particle diffusion and acceleration. A novel theory that describes diffusion has been derived from the Nonlinear Guiding Center Theory and tested with self-consistent numerical simulations. The results obtained from simulations also allowed studying acceleration phenomena. Conducting a vast campaign of simulations with different techniques set the stage to understand how different algorithms and approximations can affect the physical results at these small scales.

At magnetohydrodynamics (MHD) scales, the focus was on equilibrium and transient coherent structures, which are persistent features in space plasmas. Using well-established theory for MHD equilibria and the detection of small-scale discontinuities, numerical algorithms were used to reveal the texture of the solar wind, finding precise patterns of such structures. Subsequently, a novel tech-

nique for the identification of more general equilibrium structures was developed and tested with numerical simulations and in-situ measurements, which led to a deeper understanding of the solar wind.

Last but not least, using this recently developed technique, large scales were coupled back to small scales, finding a close correlation between MHD equilibrium structures and energetic particles using in-situ measurements of the most recent space missions.

# Abstract

La turbolenza nei plasmi è un fenomeno estremamente diffuso che caratterizza l'intero universo. I complessi fenomemi relativi ai plasmi sono presenti a tutte le scale, dai buchi neri ai laboratori per la fusione. In questa tesi di dottorato saranno discussi diversi aspetti rilevanti per i plasmi astrofisici, la trattazione di annosi problemi sarà effettuata con la sinergia di diversi approcci. Si farà uso di (I) teoria del plasma, (II) simulazioni numeriche, e (III) analisi di dati spaziali. I modelli teorici sono necessari per comprendere gli ingredienti fondamentali dei fenomeni d'interesse, anche se alle volte la trattazione matematica può diventare troppo complessa o richiedere approssimazioni troppo stringenti per essere portata avanti. Le simulazioni numeriche diventano quindi uno strumento inestimabile per far avanzare la nostra conoscenza della turbolenza nei plasmi, poiché sono il nostro unico mezzo per averne una visualizzazione diretta. Le simulazioni permettono di preparare esperimenti ad hoc per testare le teorie matematiche. Infine, le osservazioni – sia da terra che in situ – diventano lo scenario in cui sia le teorie che le simulazioni si scontrano con la realtà

Nel mio percorso, ho utilizzato tutte le metodologie appena descritte per approcciarmi a diversi problemi della turbolenza nei plasmi, dalle scale molto piccole (cinetiche) a quelle molto grandi (magnetoidrodinamiche). Alle scale cinetiche, ho investigato i problemi della diffussione e dell'accelerazione delle particelle. A partire dalla Nonlinear Guiding Center Theory è stata derivata una nuova teoria per la descrizione della diffusione, che è stata successivamente testata con simulazioni numeriche autoconsistenti. I risultati ottenuti da queste simulazioni hanno anche permesso di investigare i fenomeni di accelerazione. Inoltre, aver condotto una vasta campagna di simulazioni con diversi algoritmi, ha permesso di capire come le diverse approssimazioni possono influire sui risulati fisici alle piccole scale.

Alle scale magnetoidrodinamiche (MHD), l'attenzione è stata focalizzata sulle strutture coerenti, di equilibrio e transienti, che sono ricorrenti nei plasmi spaziali.

Utilizzando teorie consolidate per gli equilibri MHD e per la localizzazione di discontinuità a piccola scala, si sono utilizzati algoritmi per rivelare la trama del vento solare che ha mostrato schemi ricorrenti di queste strutture. Successivamente, è stata sviluppata una nuova tecnica per l'identificazione di più generiche (meno specifiche) strutture di equilibrio. Questo algoritmo è stato testato con simulazioni numeriche e applicato a misure in situ, conducendo ad una comprensione più profonda della struttura del vento solare.

Infine, utilizzando questa nuova tecnica, siamo riusciti a congiungere il mondo delle grandi scale con quello delle piccole, trovando una forte correlazione tra le strutture di equilibrio MHD e le particelle energetiche utilizzando misure in situ delle più recenti missioni spaziali.

# Contents

# Introduction

One can consider plasma the vast majority of matter in our observable universe. Because of this, plasma states in nature are both very common but also very diverse. Among several examples, one can mention the solar wind (the continuous flow originating from the Sun), planetary magnetospheres, the interstellar medium, the matter around black holes and around galaxies. All these examples consist basically of charged particles (ionized gas) moving in turbulent electromagnetic fields. Because of this vast diversity, plasmas can be described at various levels of detail, from microscopic to gargantuan scales. The heliosphere, the cavity formed by the Sun in the surrounding interstellar medium, is filled by plasma embedded into a turbulent magnetic field originating from the Sun. Its rotating motion, together with fully developed turbulence, magnetic reconnection, and wave-like activity produce complex topological structures that propagate away, filling the solar wind (Jokipii, 1966; Jokipii & Parker, 1969; Velli et al., 1989; Poedts et al., 1997). The solar wind is extremely relevant for our understanding of the universe since it is our only reachable natural laboratory. The dynamical description of astrophysical plasmas is a very challenging problem that needs to be addressed via a comprehensive use of all the tools available to the scientific community: ground-based observations, in-situ spacecraft measurements, adequate theoretical models, and numerical simulations.

Spacecraft observations reveal the presence of multi-scale turbulence (Horbury et al., 2005; Alexandrova et al., 2008; Dudok de Wit et al., 2013; Matthaeus et al., 2015; Bruno, 2019), where kinetic physics is at work and the plasma is locally far from thermodynamic equilibrium (Marsch, 2006). This non-Maxwellian state of plasmas suggests that self-consistent, weakly-collisional models need to be adopted for more realistic description (Servidio et al., 2015; Schekochihin et al., 2016; Howes, 2017). Turbulence, diffusion and particle acceleration are ubiquitous both in astrophysical and laboratory plasmas. In astrophysics, understanding

particle diffusion is of fundamental importance in order to characterize the distribution of the charged gas in the universe and, more specifically, in the heliosphere. Analogously, it is important to understand the extreme acceleration and energization events, relevant for hazardous phenomena in the framework of space weather. In principle, it could be possible to predict the trajectory of a bunch of energetic particles originating from a localized source region, being it also an explosive event such as a solar flare or a coronal mass ejection, and how it propagates out through the heliosphere (Chhiber et al., 2021). These energetic particles could run over an astronaut, a Mars colonist, or a satellite, with severe consequences. Additionally, the distribution of heavy ions in the Earth's magnetosphere can have effects on climate changes (Luo et al., 2017). These nonlinear processes are equally important for laboratory devices since they might prevent maintaining particles strictly confined inside the machine. Understanding what affects particle turbulent diffusion might help solve the confinement problem - the last step to achieve controlled fusion on Earth. The acceleration and energization problems are also related to the unsolved problem of coronal heating, to the origin of cosmic rays and solar energetic particles (Velli et al., 2015).

At the same time, charged particle distribution is known to be affected by the presence of coherent structures (Dudok de Wit et al., 1995; J. A. Tessein et al., 2015, 2016). This is also true for the less magnetized and more energetic cosmic rays, of which a reduction is measured during strong solar activity (Usoskin et al., 2005). Because of the multi-scale nature of turbulence, such coherent structures are present at various scales, but they are also of different nature. Small-scale coherent structures can be identified with current sheets and magnetic discontinuities that can be readily detected with techniques such as the Partial Variance of Increments (PVI) (Greco et al., 2008). The interaction of particles with these structures can lead to local acceleration and runaway phenomena (Osman et al., 2010; Khabarova et al., 2015). On the other hand, large-scale coherent structures can act as "boundaries" that confine particles either inside or outside the structure itself (Kittinaradorn et al., 2009; Trenchi et al., 2013).

In this thesis work, we will present diverse analyses of plasma turbulence based on mathematical models, numerical simulations and in situ measurements. In particular, in Chap. 1 we will describe different algorithms for plasma turbulence simulations, and present the campaign of simulations we performed that has been used to derive the following results; in Chap. 2, particle diffusion and small-scale

acceleration phenomena will be tackled. We will describe several diffusion theories and present the derivation of a novel one that has been tested with the performed auto-consistent simulations. With the large number of simulations at our disposal, we will also investigate the effects of different numerical parameters on the description of micro-physics; in Chap. 3 we will describe the techniques used to identify coherent structures of turbulence. We will reconstruct the 2D topology of flux ropes and develop synergistic use of well-established techniques. We will also present a novel method for the detection of helical structures. Also, observational evidence of energetic particle modulation from flux ropes will be presented. Finally, in the Conclusions, there will be a review of the results achieved during this PhD work and future perspectives.

# Chapter 1

# Turbulence simulations of collisionless plasmas

We focus our attention on collisionless plasmas, which are plasmas in which Coulomb collisions between particles are so rare to be negligible. Because of the absence of collisions, the plasma is locally far from thermodynamic equilibrium (described by Maxwellian velocity distribution functions). This condition is extremely common in the universe, but it also makes the analytical description quite difficult. The solar wind is a very interesting medium since it offers the best (and unique) opportunity to collect information about collisionless plasma phenomena in a turbulent regime thanks to in-situ spacecraft. Indeed, the average mean free path for a charged particle in the heliosphere is of the order of an astronomical unit (Sun-Earth distance). On the other hand, studying plasma on Earth is a challenging issue since plasma devices (such as tokamaks and stellarators) have confinement problems due to the growth of nonlinear instabilities, which rapidly make the system unpredictable and uncontrollable.

Besides observations and analytical theories, one formidable tool used to describe turbulent plasmas are numerical simulations. Depending on the scales and phenomena that one wants to study, the equations to solve are different, and different can be the techniques to solve them. If the focus of the study are large-scale phenomena, one can rely on MHD equations. They provide a set of fluid equations which is not influenced by particle collective motion. Because particle motion is not taken into account, solving the MHD equations is less computationally expensive and systems as large as the whole heliosphere or as a supernova can be described (Odstrcil, 2003; Mignone et al., 2007; Pomoell, J. & Poedts, S., 2018).

Such MHD fields can also provide the starting point for test-particle simulations. In this approximation, the fields are not intended to be influenced by particle motion, hence it is possible to use the fields provided by an MHD simulation and solve the Lagrangian equation of motion for particles in these prescribed fields (Ambrosiano et al., 1988; Dmitruk et al., 2003; Dmitruk et al., 2004; Zhdankin et al., 2019).

Going to a finer level of description, we find particle-in-cell (PIC) codes that can be either hybrid or full (Markidis et al., 2010; Lapenta, 2012; Franci et al., 2018). Hybrid-particle-in-cell (hybrid-PIC or HPIC) codes are used when the scales of interest lie in between the MHD range and the sub-ion lengths. Indeed, with the hybrid approach ions and electrons are treated differently: the former are present as macro-particles (see below) whereas the latter are modeled as a massless fluid that neutralizes the plasma and provides an appropriate pressure term. This separation of scales retains ion kinetic effects at the price of neglecting those of the electrons, granting a reduced computational cost (Winske, 1985; Matthews, 1994). The Lagrangian equations of motions are not applied to "actual" particles, but rather to "slices" of the distribution function, the so-called macro-particles. The drawback is that a very large number of particles per cell is needed to collect a smooth distribution function at one spatial location. If both ions and electrons have to be described as Lagrangian macro-particles, the scheme to use is the full-PIC (FPIC). In this case, the separation of scales is retained between the species, though the actual mass ratio can rarely be used (e.g. Haynes et al. (2014)). The stratagem here is to give electrons a "fictitious" larger mass, thanks to which the separation of scales becomes less pronounced so that effects due to different species can be described. Though, one shall expect some impact on the physical results of the simulation. Several works (Melzani et al., 2014; Rowan et al., 2017; Verscharen et al., 2020) aim at understanding the effects of a nonrealistic ion-to-electron mass ratio in order to give some prescription on when it is possible to use this compromise depending on the physical quantities of interest.

The last, but not least, scheme generally used is the Vlasov-Maxwell (VM). This method solves the coupled Vlasov and Maxwell equations in hybrid or full approximation (Califano et al., 2006; Valentini et al., 2007, 2014; Servidio et al., 2015). In this case, since the Vlasov equation is solved, instead of the Lagrangian evolution of distribution function slices, the drawback of needing a lot of particles to avoid noise is no longer present. Instead, the problem now is to have enough

computational resources to advance the entire distribution function (which can weigh many terabytes) at each time step.

As it should be clear by now, each method has its own advantages and disadvantages, and the choice of which to use depends on the phenomena one wants to describe. In the following, we will describe more thoroughly the aforementioned numerical schemes and compare how the choice of different approaches can affect physical results.

## 1.1 The Hybrid-Vlasov model

The fundamental set of equations to describe the dynamics of ionized matter coupled with electromagnetic fields is given by the Vlasov-Maxwell system. The self-consistent equations read

$$\frac{\partial f_\alpha}{\partial t} + \boldsymbol{v}\cdot\boldsymbol{\nabla} f_\alpha + \frac{q_\alpha}{m_\alpha}\left(\boldsymbol{E} + \frac{1}{c}\,\boldsymbol{v}\times\boldsymbol{B}\right)\cdot\boldsymbol{\nabla}_{\boldsymbol{v}} f_\alpha = 0, \tag{1.1}$$

$$\boldsymbol{\nabla}\cdot\boldsymbol{E} = 4\pi\sum_\alpha q_\alpha \int f_\alpha(\boldsymbol{r},\boldsymbol{v},t)d\boldsymbol{v}, \tag{1.2}$$

$$\boldsymbol{\nabla}\cdot\boldsymbol{B} = 0, \tag{1.3}$$

$$\boldsymbol{\nabla}\times\boldsymbol{E} + \frac{1}{c}\frac{\partial \boldsymbol{B}}{\partial t} = \boldsymbol{0}, \tag{1.4}$$

$$\boldsymbol{\nabla}\times\boldsymbol{B} - \frac{1}{c}\frac{\partial \boldsymbol{E}}{\partial t} = \frac{4\pi}{c}\sum_\alpha q_\alpha \int \boldsymbol{v} f_\alpha d\boldsymbol{v}, \tag{1.5}$$

where $f_\alpha = f_\alpha(\boldsymbol{r},\boldsymbol{v},t)$ is the velocity distribution function of the $\alpha$-th specie, $q_\alpha$ and $m_\alpha$ its charge and its mass. Generally, $\alpha$ indicates ions ($i$) and electrons ($e$), $\boldsymbol{v}$ and $\boldsymbol{r}$ are the velocity and spatial coordinates respectively, $t$ is time, $c$ is the speed of light, $\boldsymbol{E}$ and $\boldsymbol{B}$ are the electric and magnetic fields.

As already stated, solving the Vlasov-Maxwell system, Eqs. 1.1–1.5, in an Eulerian frame is numerically expensive, even for just two species (electrons and ions). It is therefore convenient to define two different scales: the ion scale $d_i = c/\Omega_i$ and the electron scale $d_e = c/\Omega_e$, where $\Omega_i$ and $\Omega_e$ are ion and electron gyration frequencies respectively. The separation of scales given by $\Omega_e \gg \Omega_i$, is the basis of the hybrid approach.

We now reduce the Vlasov-Maxwell system of Eqs. 1.1–1.5 to the hybrid approximation with the condition of massless electrons. Assuming no displacement

current (i.e. $\partial \boldsymbol{E}/\partial t = 0$) and plasma quasi neutrality (i.e. $n_i \sim n_e \equiv n$), the Ampere's law Eq. 1.5 becomes

$$\boldsymbol{\nabla} \times \boldsymbol{B} = \frac{4\pi}{c}\boldsymbol{j} = \frac{4\pi}{c} ne(\boldsymbol{u}_i - \boldsymbol{u}_e), \tag{1.6}$$

where $n$ and $\boldsymbol{u}$ are the zeroth and the first velocity distribution function moments, defined as

$$n(\boldsymbol{x}, t) = \int f(\boldsymbol{x}, \boldsymbol{v}, t)\, d\boldsymbol{v}, \tag{1.7}$$

$$n\boldsymbol{u}_\alpha(\boldsymbol{x}, t) = \int \boldsymbol{v} f_\alpha(\boldsymbol{x}, \boldsymbol{v}, t)\, d\boldsymbol{v}, \tag{1.8}$$

with $\alpha =$ electrons or ions. The electron momentum equation is

$$\frac{\partial (n\boldsymbol{u}_e)}{\partial t} + \boldsymbol{\nabla} \cdot (n\boldsymbol{u}_e\boldsymbol{u}_e) = -\frac{1}{m_e}\boldsymbol{\nabla} P_e - \frac{ne}{m_e}\left(\boldsymbol{E} + \frac{\boldsymbol{u}_e \times \boldsymbol{B}}{c}\right) \tag{1.9}$$

where $P_e$ is the scalar electron pressure term. The first term of Eq. 1.9, using quasi neutrality assumption and Ampere's and Faraday's equations, can be written as:

$$\begin{aligned}
\frac{\partial}{\partial t}(n\boldsymbol{u}_e) &= \frac{\partial}{\partial t}\left(n\boldsymbol{u}_i - \frac{\boldsymbol{j}}{e}\right) = \\
&= \frac{\partial}{\partial t}\left(n\boldsymbol{u}_i\right) - \frac{1}{e}\frac{\partial}{\partial t}\left(\frac{c}{4\pi}\boldsymbol{\nabla} \times \boldsymbol{B}\right) = \\
&= \frac{\partial}{\partial t}\left(n\boldsymbol{u}_i\right) + \frac{c^2}{4\pi e}\boldsymbol{\nabla} \times (\boldsymbol{\nabla} \times \boldsymbol{E})
\end{aligned}$$

whereas its second term is

$$\begin{aligned}
\boldsymbol{\nabla} \cdot (n\boldsymbol{u}_e\boldsymbol{u}_e) &= \boldsymbol{\nabla} \cdot \left[n\left(\boldsymbol{u}_i - \frac{\boldsymbol{j}}{ne}\right)\left(\boldsymbol{u}_i - \frac{\boldsymbol{j}}{ne}\right)\right] = \\
&= \boldsymbol{\nabla} \cdot (n\boldsymbol{u}_i\boldsymbol{u}_i) - \frac{1}{e}\boldsymbol{\nabla} \cdot (\boldsymbol{u}_i\boldsymbol{j}) - \frac{1}{e}\boldsymbol{\nabla} \cdot (\boldsymbol{j}\boldsymbol{u}_i) + \boldsymbol{\nabla} \cdot \left(\frac{\boldsymbol{j}\boldsymbol{j}}{ne^2}\right).
\end{aligned}$$

Therefore, the equation of momentum for the electrons is:

$$\frac{\partial}{\partial t}\left(n\boldsymbol{u}_i\right)+\frac{c^2}{4\pi e}\boldsymbol{\nabla}\times\left(\boldsymbol{\nabla}\times\boldsymbol{E}\right)+\boldsymbol{\nabla}\cdot\left(n\boldsymbol{u}_i\boldsymbol{u}_i\right)-\frac{1}{e}\boldsymbol{\nabla}\cdot\left(\boldsymbol{u}_i\boldsymbol{j}\right)-\frac{1}{e}\boldsymbol{\nabla}\cdot\left(\boldsymbol{j}\boldsymbol{u}_i\right)+ \\ +\boldsymbol{\nabla}\cdot\left(\frac{\boldsymbol{j}\boldsymbol{j}}{ne^2}\right)=-\frac{1}{m_e}\boldsymbol{\nabla}P_e-\frac{ne}{m_e}\left(\boldsymbol{E}+\frac{\boldsymbol{u}_e\times\boldsymbol{B}}{c}\right). \tag{1.10}$$

Analogously, the ion momentum equation is

$$\frac{\partial(n\boldsymbol{u}_i)}{\partial t}+\boldsymbol{\nabla}\cdot\left(n\boldsymbol{u}_i\boldsymbol{u}_i\right)=-\frac{1}{m_i}\boldsymbol{\nabla}\cdot\boldsymbol{\Pi}+\frac{ne}{m_i}\left(\boldsymbol{E}+\frac{\boldsymbol{u}_i\times\boldsymbol{B}}{c}\right) \tag{1.11}$$

with $\boldsymbol{\Pi}=\int(\boldsymbol{v}-\boldsymbol{u}_i)(\boldsymbol{v}-\boldsymbol{u}_i)f_i(\boldsymbol{x},\boldsymbol{v},t)d\boldsymbol{v}$ being the ion pressure tensor defined as the second moment of the ion distribution function. By subtracting (1.11) from (1.10) we obtain an equation without time derivatives

$$\frac{c^2}{4\pi e}\boldsymbol{\nabla}\times\left(\boldsymbol{\nabla}\times\boldsymbol{E}\right)-\frac{1}{e}\boldsymbol{\nabla}\cdot\left(\boldsymbol{u}_i\boldsymbol{j}\right)-\frac{1}{e}\boldsymbol{\nabla}\cdot\left(\boldsymbol{j}\boldsymbol{u}_i\right)+\boldsymbol{\nabla}\cdot\left(\frac{\boldsymbol{j}\boldsymbol{j}}{ne^2}\right)= \\ =-\frac{1}{m_e}\boldsymbol{\nabla}P_e+\frac{1}{m_i}\boldsymbol{\nabla}\cdot\boldsymbol{\Pi}-\frac{ne}{m_e}\left(\boldsymbol{E}+\frac{\boldsymbol{u}_e\times\boldsymbol{B}}{c}\right)+\frac{ne}{m_i}\left(\boldsymbol{E}+\frac{\boldsymbol{u}_i\times\boldsymbol{B}}{c}\right) \tag{1.12}$$

and we can rewrite the terms

$$\begin{aligned}
&\frac{ne}{m_e}\left(\boldsymbol{E}+\frac{\boldsymbol{u}_e\times\boldsymbol{B}}{c}\right)+\frac{ne}{m_i}\left(\boldsymbol{E}+\frac{\boldsymbol{u}_i\times\boldsymbol{B}}{c}\right)= \\
&=-\mu ne\boldsymbol{E}-\frac{ne}{c}\left(\frac{\boldsymbol{u}_e}{m_e}+\frac{\boldsymbol{u}_i}{m_i}\right)\times\boldsymbol{B}= \\
&=-\mu ne\boldsymbol{E}-\frac{ne}{c}\left(\frac{\boldsymbol{u}_e}{m_e}+\frac{\boldsymbol{u}_i}{m_i}+\frac{\boldsymbol{u}_i}{m_e}-\frac{\boldsymbol{u}_i}{m_e}\right)\times\boldsymbol{B}= \\
&=-\mu ne\boldsymbol{E}-\frac{ne}{cm_e}\left(\boldsymbol{u}_e-\boldsymbol{u}_i\right)\times\boldsymbol{B}-\frac{ne}{c}\left(\frac{\boldsymbol{u}_i}{m_i}-\frac{\boldsymbol{u}_i}{m_e}\right)\times\boldsymbol{B}= \\
&=-\mu ne\boldsymbol{E}+\frac{1}{cm_e}\left(\boldsymbol{j}\times\boldsymbol{B}\right)-\frac{\mu ne}{c}\left(\boldsymbol{u}_i\times\boldsymbol{B}\right)
\end{aligned}$$

where $\mu=1/m_e+1/m_i$, and substituting them into (1.12) we obtain

$$\mu ne\boldsymbol{E}+\frac{c^2}{4\pi e}\boldsymbol{\nabla}\times\left(\boldsymbol{\nabla}\times\boldsymbol{E}\right)=\frac{1}{m_i}\boldsymbol{\nabla}\cdot\boldsymbol{\Pi}-\frac{1}{m_e}\boldsymbol{\nabla}P_e+ \\ +\frac{1}{cm_e}\left(\boldsymbol{j}\times\boldsymbol{B}\right)-\frac{\mu ne}{c}\left(\boldsymbol{u}_i\times\boldsymbol{B}\right)+\frac{1}{e}\boldsymbol{\nabla}\cdot\left(\boldsymbol{u}_i\boldsymbol{j}\right)-\frac{1}{e}\boldsymbol{\nabla}\cdot\left(\boldsymbol{j}\boldsymbol{u}_i\right)+\boldsymbol{\nabla}\cdot\left(\frac{\boldsymbol{j}\boldsymbol{j}}{ne^2}\right).$$

Finally, if we say $\mu \sim 1/m_e$ and use the quasi neutrality assumption, $\boldsymbol{\nabla} \times (\boldsymbol{\nabla} \times \boldsymbol{E}) \sim -\boldsymbol{\nabla}^2 \boldsymbol{E}$, we obtain the Ohm's law

$$\begin{aligned} \boldsymbol{E} - \frac{m_e c^2}{4\pi n e^2} \boldsymbol{\nabla}^2 \boldsymbol{E} = \frac{m_e}{n e m_i} \boldsymbol{\nabla} \cdot \boldsymbol{\Pi} - \frac{1}{ne} \boldsymbol{\nabla} P_e + \frac{1}{cne} (\boldsymbol{j} \times \boldsymbol{B}) - \frac{\boldsymbol{u}_i \times \boldsymbol{B}}{c} + \\ + \frac{m_e}{ne^2} \left[ ne \boldsymbol{\nabla} \cdot (\boldsymbol{u}_i \boldsymbol{j} + \boldsymbol{j} \boldsymbol{u}_i) - \boldsymbol{\nabla} \cdot (\boldsymbol{j} \boldsymbol{j}) \right]. \end{aligned} \tag{1.13}$$

Since we consider electrons as a massless fluid we can drop all terms depending on $m_e$, for $m_e \to 0$, obtaining the Ohm's law in Hall MHD (HMHD) approximation (Büchner et al., 2003; Birdsall & Langdon, 2004; Valentini et al., 2007)

$$\boldsymbol{E} = -\frac{\boldsymbol{u}_i \times \boldsymbol{B}}{c} + \frac{\boldsymbol{j} \times \boldsymbol{B}}{cne} - \frac{1}{ne} \boldsymbol{\nabla} P_e. \tag{1.14}$$

Neglecting the displacement current in Maxwell's equations means that the electric field does not depend explicitly on time. It is explicitly determined by the magnetic field $\boldsymbol{B}$, the electron pressure $P_e$, the numerical density $n$ and the ion bulk velocity $\boldsymbol{u}_i$ (Matthews, 1994).

For the electron pressure term, an appropriate equation of state (e.g. isothermal or adiabatic) can be used. Since the system is highly nonlinear, to prevent numerical errors, we introduce a resistive term $\eta \boldsymbol{j}$ in Ohm's law, with $\eta$ being the resistivity. So the corrected Ohm's law for the electric field becomes

$$\boldsymbol{E} = -\frac{\boldsymbol{u}_i \times \boldsymbol{B}}{c} + \frac{\boldsymbol{j} \times \boldsymbol{B}}{cne} - \frac{1}{ne} \boldsymbol{\nabla} P_e + \eta \boldsymbol{j}. \tag{1.15}$$

This resistive term $\eta \boldsymbol{j}$ is important since it models, somehow, the very small-scale dissipative terms. We can write now the hybrid Vlasov-Maxwell system that reads:

$$\frac{\partial f}{\partial t} + \boldsymbol{v} \cdot \boldsymbol{\nabla} f + \frac{e}{m} \left( \boldsymbol{E} + \frac{\boldsymbol{v}}{c} \times \boldsymbol{B} \right) \cdot \boldsymbol{\nabla}_{\boldsymbol{v}} f = 0, \tag{1.16}$$

$$\frac{\partial \boldsymbol{B}}{\partial t} = -c \boldsymbol{\nabla} \times \boldsymbol{E}, \tag{1.17}$$

$$\boldsymbol{E} = -\frac{\boldsymbol{u}_i \times \boldsymbol{B}}{c} + \frac{\boldsymbol{j} \times \boldsymbol{B}}{cne} - \frac{1}{ne} \boldsymbol{\nabla} P_e + \eta \boldsymbol{j}. \tag{1.18}$$

Finally, we can rescale the equations using the following plasma characteristic quantities:

$$
\begin{aligned}
&\boldsymbol{v} = \boldsymbol{v}' v_{_A}, \\
&\omega = \omega' \Omega_{c_i}, \\
&\boldsymbol{x} = \boldsymbol{x}' d_i = \boldsymbol{x}' c/\omega_{p_i} = \boldsymbol{x}' v_{_A}/\Omega_{c_i}, \\
&\boldsymbol{B} = \boldsymbol{B}' v_{_A} \sqrt{4\pi n m_i} = \boldsymbol{B}' m_i c \Omega_{c_i}/e, \\
&\boldsymbol{E} = \boldsymbol{E}' m_i v_{_A} \Omega_{c_i}/e, \\
&P_e = P_e' n m_i v_{_A}^2, \\
&\omega_{p_i}^2 = 4\pi n e^2/m_i,
\end{aligned}
$$

where $v_{_A} = B/\sqrt{4\pi n m_i}$ is the Alfvén velocity, $\Omega_{c_i}$ is the ion cyclotron frequency, $d_i$ is the ion skin depth, $\omega_{p_i}$ is the ion plasma frequency, $n$ is the ion numerical density and $m_i$ is the ion mass. The normalized system of equations, getting rid of primes for the new variables and of the $i$ subscript for ion quantities, finally reads

$$\frac{\partial f}{\partial t} + \boldsymbol{v} \cdot \boldsymbol{\nabla} f + (\boldsymbol{E} + \boldsymbol{v} \times \boldsymbol{B}) \cdot \boldsymbol{\nabla}_{\boldsymbol{v}} f = 0, \tag{1.19}$$

$$\frac{\partial \boldsymbol{B}}{\partial t} = -\boldsymbol{\nabla} \times \boldsymbol{E}, \tag{1.20}$$

$$\boldsymbol{E} = -(\boldsymbol{u} \times \boldsymbol{B}) + \frac{1}{n} \boldsymbol{j} \times \boldsymbol{B} - \frac{1}{n} \boldsymbol{\nabla} P_e + \eta \boldsymbol{j}. \tag{1.21}$$

As follows, we describe a numerical technique to solve Eqs. 1.19–1.21.

## 1.2 The PIC algorithm

Solving Eqs. 1.19–1.21 in an Eulerian fashion implies solving seven equations in a seven-dimensional space (3D in space, 3D in the velocity space, plus time evolution). This procedure, although pretty straightforward, is very expensive. The drawbacks of the Vlasov-Eulerian approach are the long execution times and the huge computational resources needed to store and advance the distribution function over the whole phase space (Valentini et al., 2007). Moreover, the algorithm does not provide information on particle trajectories, but only on the velocity distribution function $f(\boldsymbol{x}, \boldsymbol{v}, t)$. An alternative (and more practical) approach is given by the PIC method. In PIC algorithms, particles are free to move in the continuous

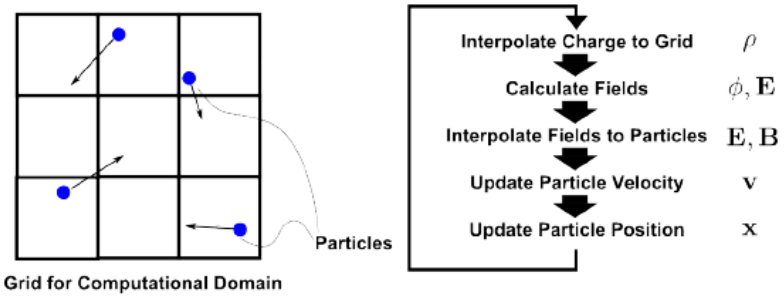


Figure 1.1: Schematic representation of the PIC method. (Left) Particles are free to move over the continuous computational domain, while fields and distribution function moments are defined only on grid points. The back reaction between field and particles is obtained by mutual interpolation (right). Adapted from Ebersohn et al. (2014).

phase space and their Lagrangian equations of motion are solved by interpolating the fields from grid points to particles positions (Winske, 1985). Conversely, the distribution function moments and the self-consistent fields are computed interpolating charge and current source terms on the defined grid points in the cycle depicted in Fig. 1.1.

In PIC codes, particles are actually macro-particles (Matthews, 1994), that represent fractions of $f(\boldsymbol{x}, \boldsymbol{v}, t)$. This is formally consistent with a picture where particles represent $\delta$-functions in the continuous phase-space, implying that they occupy a finite volume (Klimontovich, 1997). The utility of PIC algorithms is that each particle is followed individually through the Lagrangian approach solving its equations of motion. While in the Eulerian treatment one has few equations in a huge phase-space, in PIC codes one has few equations for a huge number of particles. A large number of macro-particles is required in order to have a statistically valuable description of the system. Moreover, the wider the distribution function, the more macro-particles are needed for a less noisy description. Contrary to test-particle algorithms, particles and fields are now nonlinearly coupled, interacting and exchanging information. The self-consistent approach is fundamental when treating transport problems in low-collisionality plasmas where the distribution function departs from the thermal Maxwellian (Servidio et al., 2016), as it happens in the solar wind (Marsch, 2006). When distribution functions are non-Maxwellian, they are prone to develop instabilities and the plasma generates waves, that may induce heating (Poedts & Goedbloed, 1997), to restore its thermal equilibrium.

Some of the physical systems we want to describe have a mean (guiding) magnetic field, such as coronal loops (Einaudi et al., 1996), the solar wind (Bieber et al., 1996) and also plasma fusion devices (Ongena et al., 2016). It is well-established that, when the plasma is sufficiently magnetized, fluctuations mainly lie in the plane perpendicular to the average field $\boldsymbol{B}_0$ and the variations along the mean field can be neglected (Shebalin et al., 1983; Matthaeus & Lamkin, 1986; Dmitruk et al., 2004; Servidio et al., 2015; Wan et al., 2016). This approximation is commonly referred to as 2.5D geometry, where fields have all three components, but depend only on the coordinates perpendicular to $\boldsymbol{B}_0$. This approximation allows neglecting $z$-variations, and simulate the time evolution of the quantities in 2D, sparing some computational time. In this geometry, the in-plane magnetic field is $\boldsymbol{B}_\perp = \nabla a_z \times \hat{\mathbf{z}}$, where $a_z$ is the magnetic potential and $\hat{z}$ is the out-of-plane unit vector. The current in the axial direction is $j_z = (\boldsymbol{\nabla} \times \boldsymbol{B}_\perp) \cdot \hat{z} = -\nabla^2 a_z$. In the following, we will describe the codes used to obtain the results presented in the next Chapters.

### 1.2.1 Hybrid-PIC simulations of turbulence

The equations that are directly solved for the HPIC simulations are:

$$\dot{\boldsymbol{x}} = \boldsymbol{v}, \tag{1.22}$$

$$\dot{\boldsymbol{v}} = \boldsymbol{E} + \boldsymbol{v} \times \boldsymbol{B}, \tag{1.23}$$

$$\frac{\partial \boldsymbol{B}}{\partial t} = -\boldsymbol{\nabla} \times \boldsymbol{E}, \tag{1.24}$$

$$\boldsymbol{E} = -\boldsymbol{u} \times \boldsymbol{B} + \frac{1}{n}\boldsymbol{j} \times \boldsymbol{B} - \frac{1}{n}\boldsymbol{\nabla} P_e + \eta \boldsymbol{j}. \tag{1.25}$$

These are formally equivalent to the Vlasov-Maxwell system in Eqs. 1.19–1.21. In the above equations, $\boldsymbol{x}$ is the particle position, $\boldsymbol{v}$ the velocity, $\boldsymbol{E}$ is the electric field, $\boldsymbol{B}$ is the magnetic field, $n = \int f d\boldsymbol{v}$ is the ion number density, $\boldsymbol{u} = (1/n) \int \boldsymbol{v}\ f d\boldsymbol{v}$ is the proton bulk velocity, and $\boldsymbol{j} = \boldsymbol{\nabla} \times \boldsymbol{B}$ is the current density. In the above definitions $f(\boldsymbol{x}, \boldsymbol{v}, t)$ is the velocity distribution function of the ions.

The adiabatic electron pressure term is $P_e = \beta n^\gamma$ with $\gamma = 5/3$, and $\eta = 0.006$ is the resistivity that introduces a small scale dissipation for numerical stability. The choice of a particular equation of state (in this case adiabatic), is not always

| ID | $N_x \times N_y$ | ppc | $\beta$ |
|---|---|---|---|
| H1 | $512 \times 512$ | 1500 | 0.1 |
| H2 | $512 \times 512$ | 1500 | 0.5 |
| H3 | $512 \times 512$ | 1500 | 5 |

Table 1.1: Parameters of the HPIC simulations. The first column is the label identifying the simulation, $N_x$ and $N_y$ are the number of cells in the $x$ and $y$ directions respectively, ppc is the number of particles per cell, and in the last column we report the plasma $\beta$.

completely justified when simulations of the complex, collisionless, multi-species solar wind are carried out. However, to be able to describe the puzzling problem of plasma turbulence, one has to assume some simplifications (Parashar et al., 2014). Despite this assumption, the above model represents a step further in plasma description with respect to classical MHD treatment. The main unjustified assumptions remain (I) the use of resistivity (for purely numerical reasons) and (II) the choice of the electron equation of state. Regarding the assumption (I), we verified that the resistive term acts only at very small, grid-size scales. Regarding the (II), it will be fully overcome with the use of the full-PIC model, as described in the next Section.

The electric field is given by the generalized Ohm's law. Distances are normalized to the ion skin depth $d_i = c/\omega_{p_i}$, where $c$ is the speed of light and $\omega_{p_i}$ is the ion plasma frequency. The time is normalized to $\Omega_{ci}^{-1}$, that is the ion cyclotron frequency. Finally, velocities are normalized to the Alfvén speed $v_{_A} = c\Omega_{ci}/\omega_{p_i}$. We performed three hybrid-PIC simulations in 2.5D approximation, varying the ion plasma $\beta$, defined as the ratio between thermal and magnetic pressure, namely $\beta = P_{cin}/P_B = 2v_{th}^2/v_A^2$, with $v_{th}$ and $v_A$ being the initial thermal and the Alfvén speeds (related to the mean field $B_0$), respectively. The plasma $\beta$ is equal for ions and electrons. We performed three runs with $\beta = 5$, 0.5, and 0.1, to cover a wide range of relevant environments. These values are such that high $\beta$ is typical of plasmas found in the Earth's magnetosheath; the value of $\beta = 0.5$ is close to the typical solar wind conditions, whereas the lowest $\beta$ is appropriate for solar corona and laboratory devices. The details are summarized in Table 1.1.

The three simulations have the same initial conditions: uniform density and a Maxwellian distribution of particles velocities with uniform temperature. We impose random fluctuations with a power law spectrum for both the magnetic field and the ion bulk velocity field. The Eqs. 1.22–1.25 are solved on a square grid of

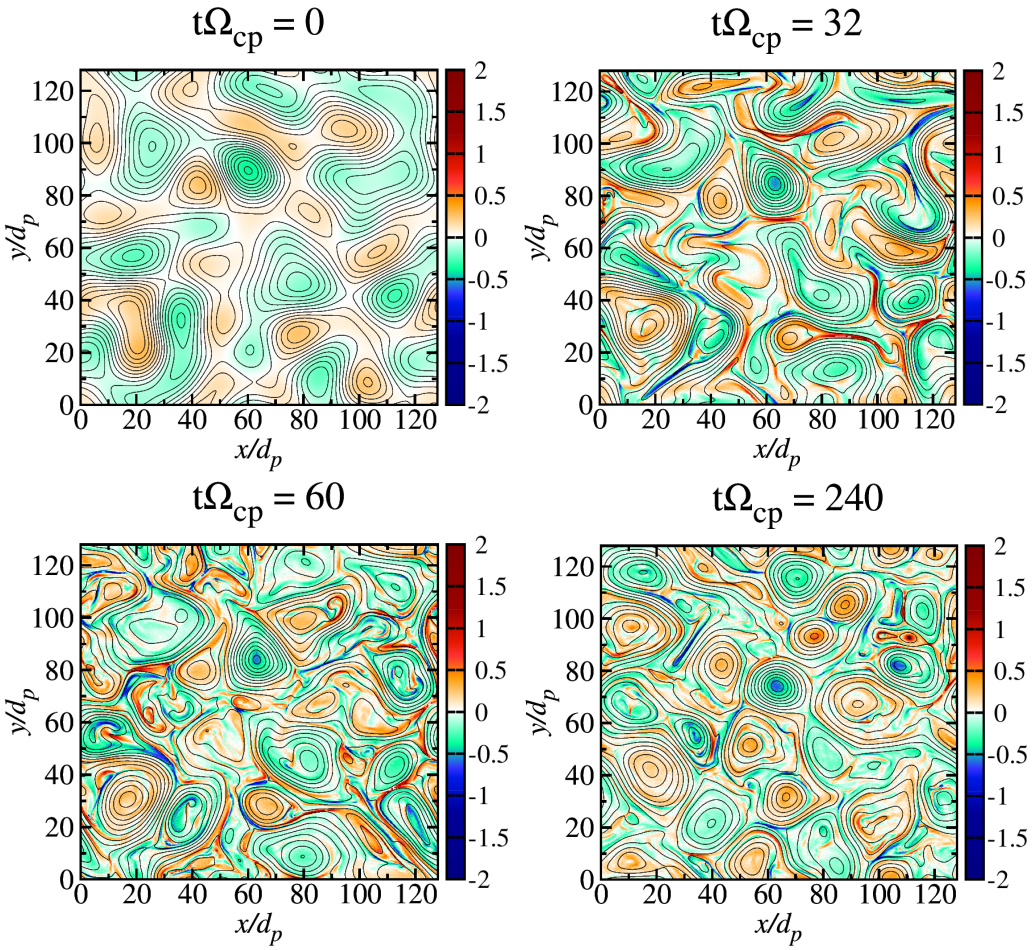


Figure 1.2: Current density $j_z$ (color shading) together with vector potential $a_z$ (contour lines), at different times of the turbulent evolution. (Top left) The initial state is composed of large structures and tenuous axial current. As turbulence develops in time, coherent structures such as small vortices and intense current sheets appear. The most intense current sheets are located in between reconnecting magnetic islands.

size $L = 2\pi \times 20 d_i$ discretized with $512^2$ points, and periodic boundary conditions (in the following, the subscripts $i$ and $p$ will be used interchangeably as protons are the only present species of ions). The initial state consists of a 2D spectrum of fluctuations, perpendicular to the main field $B_0$ (the latter chosen along $z$). The fluctuations' amplitude is $\delta b/B_0 \sim 0.3$. To dampen the statistical noise of the PIC method, we use 1500 particles per cell (about $4 \times 10^8$ total particles). This set of simulations is also described in Servidio et al. (2016); Pecora et al. (2018); Pecora, Pucci, et al. (2019).

To ensure statistical invariance of the following analyses, they were performed

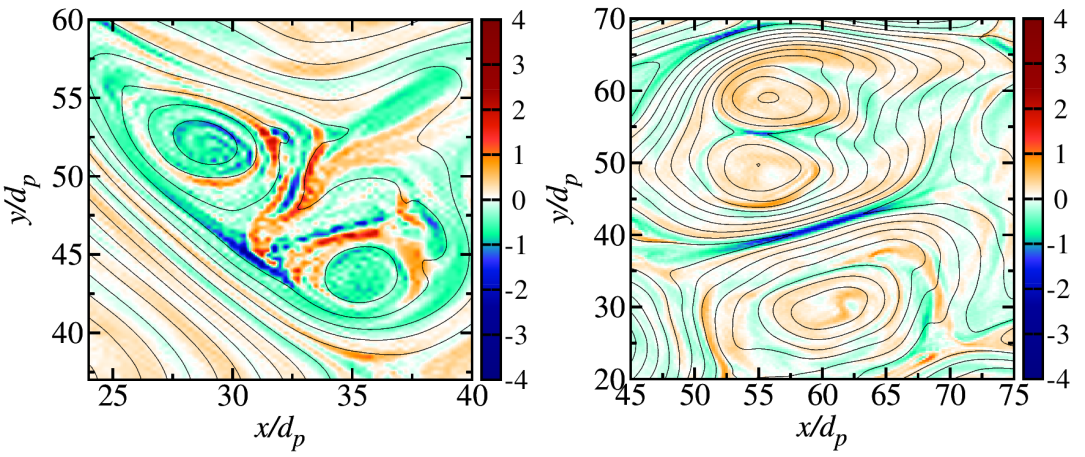


Figure 1.3: Zooms into small-scale structures of Fig. 1.2. In between magnetic islands it is possible to observe intense current sheets, whose typical dimension is on the order of the ion skin depth.

in steady state turbulence. To achieve this state, we borrow ideas from hydrodynamics (S. Chen et al., 1993), and let the system initially evolve unperturbed. Then, we introduce a forcing at the peak of nonlinearity (roughly the peak of $\langle j_z^2 \rangle$). The forcing consists of "freezing" the amplitude of the large-scale modes of the in-plane magnetic field, with $1 \leq m \leq 4$, leaving the phases unchanged. This corresponds to a large-scale input of energy as described in Servidio et al. (2016). The evolution of the simulation is shown in Fig. 1.2, where the color shading indicates the out-of-plane current density $j_z$ and contour lines represent the magnetic potential $a_z$. The initial state is formed by a few big and tenuous vortices starting to interact. After a few times (the peak of nonlinearity is reached at $t\Omega_{cp} \sim 25$), large eddies start to interact and fragment into smaller ones also creating localized strong gradients (Matthaeus & Montgomery, 1980; Servidio et al., 2015). The global appearance of the system remains unchanged, in a statistical sense, after the peak of nonlinearity has been reached. These regions of small, intense current sheets, appear in between interacting magnetic islands (flux tubes in 3D). They are possibly associated with magnetic reconnection that is a fundamental process for which the magnetic field changes topology. This process leads to the conversion of magnetic energy into particle kinetic energy (Parker, 1957; Drake et al., 2006; Ono et al., 1996; Hayashi & Sato, 1978; Yoo et al., 2013), as will be investigated in the following Chapter. Figure 1.3 shows a blow-up over these small intense structures developing in the simulations.

The approach to statistical invariance of turbulence can also be observed with

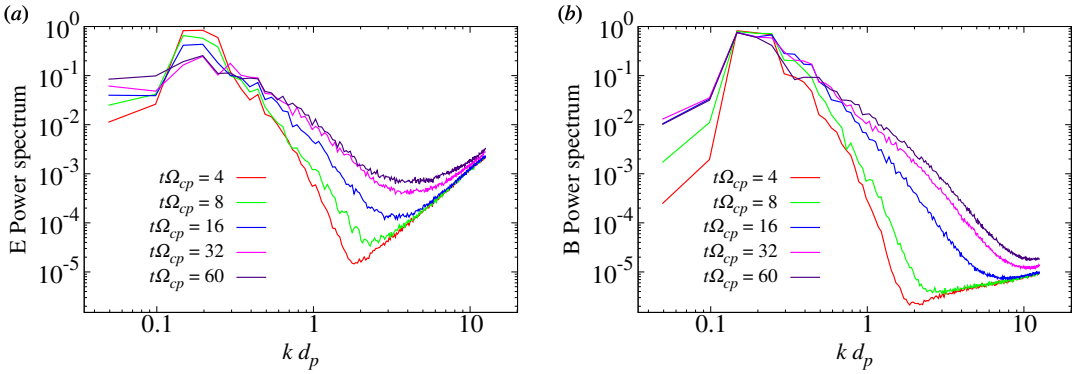


Figure 1.4: Power spectra of (a) electric and (b) magnetic fields as a function of the wavenumber (normalized with the proton skin depth $d_p$), at different times for HPIC simulations. While turbulence develops, energy is transferred from the large to the small scales.

the Fourier spectra, as a function of the wavenumber $|\boldsymbol{k}|$, of both the electric and magnetic fields. The power spectra for the trace of the correlation tensor, $|\tilde{\boldsymbol{B}}(\boldsymbol{k},t)|^2$, where $\tilde{\boldsymbol{B}}(\boldsymbol{k},t)$ are the respective Fourier coefficients, are reported in Fig. 1.4. These spectra exhibit the classical scenario of MHD turbulence, in which energy flows from large to small scales as Fig. 1.2 shows in configuration space. This cascade of energy occurs over the so-called inertial range, where the energy spectrum scales as $k^{-5/3}$ (Bruno & Carbone, 2016). Figure 1.4 shows how turbulence develops transferring energy from low to high $k$'s. For these HPIC simulations, the state of fully developed turbulence is achieved after $\sim 50\Omega_{cp}^{-1}$. After this time, the spectra are almost stationary. It is important to note that, as observed in the solar wind (Bale et al., 2005), the power in the electric fields is higher, at $k$'s that correspond to characteristic ion lengths. This is in agreement with previous studies and simulations of plasma turbulence (Howes et al., 2008; Matthaeus et al., 2008; Schekochihin et al., 2009; TenBarge et al., 2013; Franci et al., 2015).

### 1.2.2 Full-PIC simulations of turbulence

We will also use full kinetic simulations that were performed with an implicit PIC algorithm implemented in a 3D parallel code, called iPIC3D (Markidis et al., 2010; Lapenta, 2012). The governing equations, in code units, are:

$$\frac{\partial f_s}{\partial t} + \boldsymbol{v} \cdot \frac{\partial f_s}{\partial \boldsymbol{x}} + \frac{q_s}{m_s} (\boldsymbol{E} + \boldsymbol{v} \times \boldsymbol{B}) \cdot \frac{\partial f_s}{\partial \boldsymbol{v}} = 0,$$

$$\boldsymbol{\nabla}^2 \boldsymbol{E} - \frac{\partial^2 \boldsymbol{E}}{\partial t^2} = 4\pi \frac{\partial \boldsymbol{j}}{\partial t} + 4\pi \boldsymbol{\nabla} \rho,$$

$$\frac{\partial \boldsymbol{B}}{\partial t} = -\boldsymbol{\nabla} \times \boldsymbol{E}.$$

In this case, lengths are normalized to $d_i$, times to $d_i/c$, and velocities to $c$, that is set to 1 in code units. The mass ratio used is $m_i/m_e = 25$, and $v_A/c = B_0 = 10^{-2}$. $(q_s/m_s)$ is the charge-to-mass ratio of the species $s$, normalized to the physical ion charge-to-mass ratio. $\rho = \sum_s q_s \int f_s d\boldsymbol{v}$ and $\boldsymbol{j} = q_s \int \boldsymbol{v} f_s d\boldsymbol{v}$ are the charge density and the current density computed over the two species $s$. The electric and magnetic fields are given by the Maxwell equations whose solution is computed implicitly, meaning that, with respect to a time step $n$, the charge density $\rho$ is evaluated at time $n+1$ and the current density $\boldsymbol{j}$ at an intermediate step $n + 1/2$ (Markidis et al., 2010). The time step is $\Delta t = (1/8\pi)\, \tau_{ge}$, with $\tau_{ge} = 2\pi/\Omega_{ce}$ being the electron cyclotron frequency. The implicit scheme allows using a larger time-step (not restricted to follow a stability condition imposed by the smallest scales) so it is possible to follow the simulation for longer times, at the price of more computational resources needed to invert the matrix for variables computed at intermediate steps.

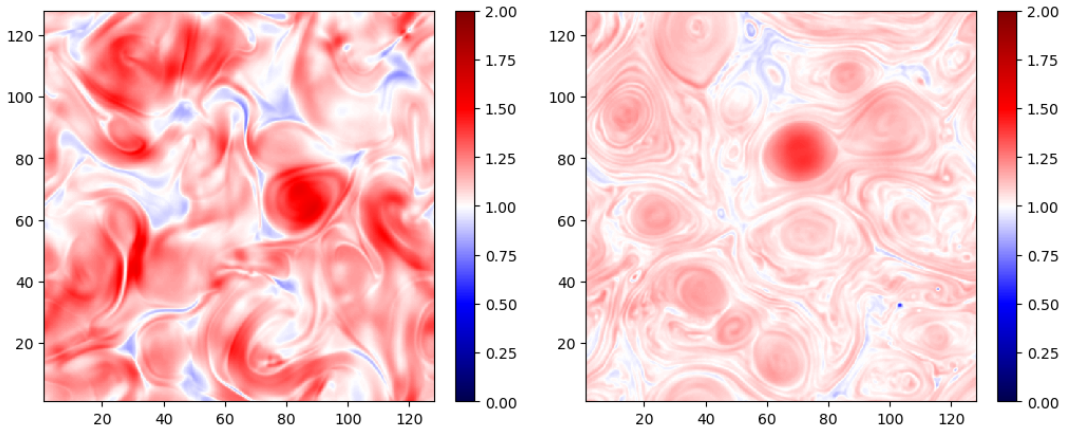


Figure 1.5: Magnetic field magnitude at (left) initial and (right) final times of K1 simulation. Refer to Table 1.2 for K1 details.

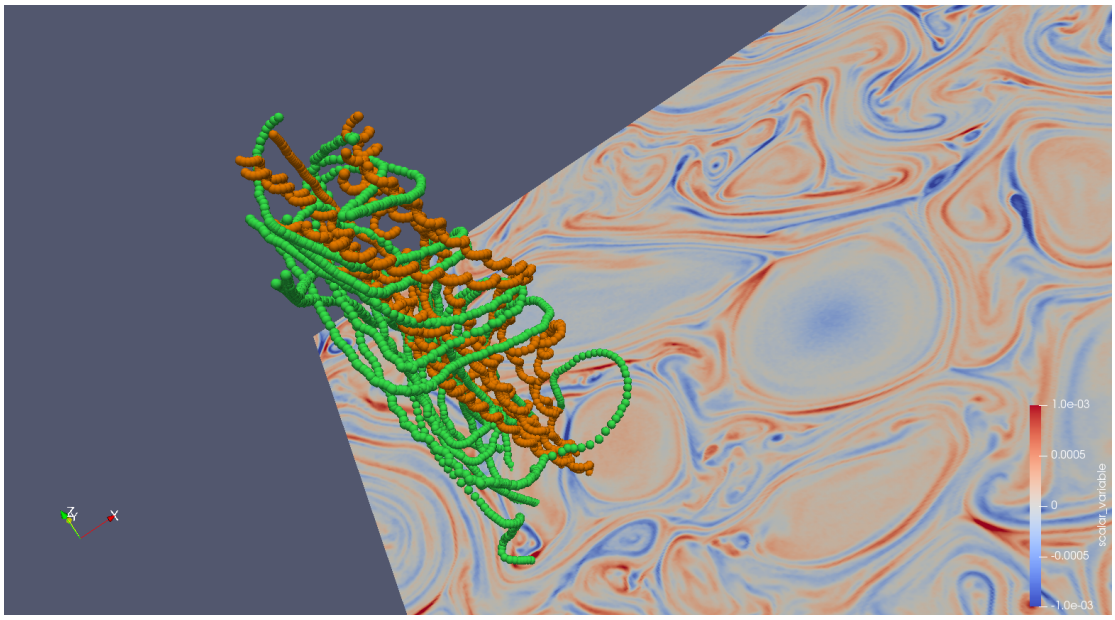


Figure 1.6: Trajectories of some ions (orange) and electrons (green) in an FPIC simulation. In the $x-y$ plane a color map of $j_z$ is reported. The $z$ direction represents the time axis and the direction of the mean magnetic field.

This new campaign of simulations has been conducted with the same values of plasma $\beta$ and box size as those of the HPIC simulations presented in the previous Section. Some variations on the number of cells (and hence on resolution) and the number of particles per cell have been included to study the convergence. The full list of simulations and parameter details is reported in Table 1.2. Turbulence evolution for one of the simulations is shown in Fig. 1.5. In Fig. 1.6, we show the trajectories of some ions and electrons, as FPIC simulations allow to describe both species from a kinetic point of view, over a map of the current density $j_z$.

### Energy conservation

One of the major issues that arises when dealing with simulations is the conservation of total energy. We define a measure of the conservation of the energy, as

$$\Psi(t) = \frac{\mathcal{E}(t) - \mathcal{E}(0)}{\mathcal{E}(0)}, \tag{1.26}$$

where $\mathcal{E}$ is the total plasma energy. The energy is given by magnetic $\mathcal{E}_B = \int d\boldsymbol{r} B^2/8\pi$ and electric $\mathcal{E}_E = \int d\boldsymbol{r} E^2/8\pi$ contributions, and the particles total

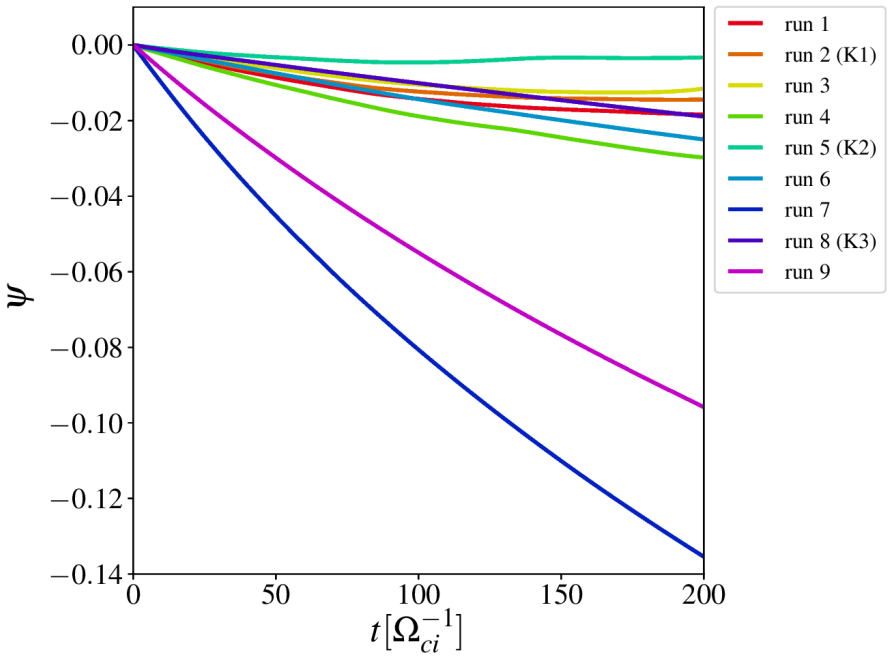


Figure 1.7: Total energy conservation for the FPIC simulations. All of them conserve energy within 3% of the initial value. Only run 7 and run 9 go down to $\sim 14\%$ and $\sim 10\%$, respectively. From (Pecora, Pucci, et al., 2019).

kinetic energy $\mathcal{E}_K = 1/2 \sum_\alpha \sum_p m_\alpha v_{\alpha,p}^2$, where the index $p$ runs over all the particles and $\alpha$ over the two species (ions and electrons).

Figure 1.7 shows the energy conservation parameter $\Psi$, for all the FPIC simulations. The general behavior is very good since eight runs out of ten do conserve energy within $\sim 3\%$ of the initial value. All the losses are due to the semi-implicit method (Lapenta & Markidis, 2011; Lapenta, 2017). Only two runs go down to $\sim 10\%$ and $\sim 14\%$. In these latter two cases, $\beta_{tot} = 10$, suggesting that less magnetized plasmas need to be treated more carefully. In fact, higher $\beta$ means larger excursions in the velocity subspace, and therefore the number of particles should increase to correctly reconstruct the VDF. This means that the wider the distribution (the less magnetized the plasma), the more particles are needed to sample the distribution accurately. As it can be seen from Fig. 1.7, run 7 is the worst simulation regarding energy conservation, and doubling both the resolution and the number of particles does not imply a noticeable improvement (run 9). Instead, a huge improvement in energy conservation is achieved when the number of particles per cell is increased by one order of magnitude, even with lower resolution (run 8). When the plasma $\beta$ is average or low, the energy conservation is

| ID | $N_x \times N_y$ | ppc | $\beta_e = \beta_i$ | $\beta_{tot}$ | $\Psi_{max}$ |
|---|---|---|---|---|---|
| run1 | $512 \times 512$ | 400 | 0.1 | 0.2 | -1.8% |
| run2 (K1) | $512 \times 512$ | 4000 | 0.1 | 0.2 | -1.4% |
| run3 | $1024 \times 1024$ | 1000 | 0.1 | 0.2 | -1.2% |
| run4 | $512 \times 512$ | 400 | 0.5 | 1 | -3.0% |
| run5 (K2) | $512 \times 512$ | 4000 | 0.5 | 1 | -0.3% |
| run6 | $1024 \times 1024$ | 1000 | 0.5 | 1 | -2.5% |
| run7 | $512 \times 512$ | 400 | 5 | 10 | -13.5% |
| run8 (K3) | $512 \times 512$ | 4000 | 5 | 10 | -1.9% |
| run9 | $1024 \times 1024$ | 1000 | 5 | 10 | -9.6% |

Table 1.2: Parameters used for the FPIC simulations. ID is the label identifying the simulation, $N_x$ and $N_y$ are the number of cells in the $x$ and $y$ directions respectively, ppc is the number of particles per cell, $\beta_e$ and $\beta_i$ are the plasma $\beta$ for electrons and ions respectively and $\beta_{tot}$ is the total plasma $\beta = \beta_i + \beta_e$. $\Psi_{max}$ is the maximum energy variation of the run as defined in Eq. 1.26 and reported in Fig. 1.7.

excellent and quite similar among all the runs.

The best energy conservation is achieved in run 5 - large number of ppc and low $\beta$. This leads us straightforwardly to the choice of run 5 and run 8 as the best candidates to look at the physical effects, along with run 2. In the next Chapter, the FPIC runs K1 ($\beta = 0.1$), K2 ($\beta = 0.5$), and K3 ($\beta = 5$), are going to be compared with the HPIC runs H1 ($\beta = 0.1$), H2 ($\beta = 0.5$) and H3 ($\beta = 5$).

# Chapter 2

# Particle diffusion and acceleration in plasma turbulence

The description of the motion of charged particles in astrophysics dates back to the approaches of Bohm (1949); Longmire and Rosenbluth (1956); Morrison (1956); Meyer et al. (1956); Parker (1965); Taylor and McNamara (1971). Steps forward have been made since then, new theories have been developed, numerical simulations have evolved far beyond early imaginations, modern spacecraft have unprecedented resolutions, but the problem of charged particles diffusing in a turbulent magnetic field is still waiting to achieve closure. Longmire and Rosenbluth (1956) started solving the problem with smooth magnetic field lines, so the guiding center of the motion remains fixed on the same field line. Collisions have then been introduced, as scattering centers, to allow random diffusion across the magnetic field. Later on, the discussion moved to non-collisional plasmas with the description of cosmic-ray penetration in the heliosphere. In this case, the scattering centers are magnetic field irregularities that cause particles to deviate from their free streaming along field lines (Morrison, 1956; Meyer et al., 1956; Parker, 1965; Jokipii & Parker, 1969). The close correlation between particle diffusion and magnetic field irregularities sets the stage for other fundamental phenomena happening in plasma turbulence: particle acceleration and energization. Several mechanisms are involved in this process, ranging from interaction with large-scale magnetic structures (Fermi, 1949, 1954) to smaller-scale events such as magnetic reconnection (Ambrosiano et al., 1988; Drake et al., 2009, 2010; Blasi, 2013; Guo et al., 2015). In this Chapter, some of the most recent and valuable theories will be described, along with developments and results obtained during the PhD.

## 2.1 Ideal single-particle motion

The motion of plasma's charged particles is, in principle, difficult to describe mathematically in a self-consistent way because particles and fields influence each other. A simple description of the trajectory of a charged particle moving through electric and magnetic fields can be obtained by neglecting its feedback on the external fields. To have a basic picture of particle motion, we make one more approximation, imposing that the external electric and magnetic fields are static and spatially uniform. The equation of motion is given by the Lorenz force

$$m\ddot{\boldsymbol{r}} = q(\boldsymbol{E} + \dot{\boldsymbol{r}} \times \boldsymbol{B}), \tag{2.1}$$

where $\boldsymbol{r} = (x, y, z)$ is the particle position vector, $\boldsymbol{E}$ and $\boldsymbol{B}$ the electric and magnetic fields. Without loss of generality, we can impose the magnetic field along $z$, namely $\boldsymbol{B} = (0, 0, B)$, and the electric field is in the $xz$ plane, $\boldsymbol{E} = (E_\perp, 0, E_\parallel)$. The equation of motion can be decomposed in the three directions as

$$\begin{aligned} m\ddot{x} &= q(E_\perp + \dot{y}B), & (2.2)\\ m\ddot{y} &= -q\dot{x}B, & (2.3)\\ m\ddot{z} &= qE_\parallel. & (2.4) \end{aligned}$$

Equation 2.4 can be readily solved since it is decoupled from the others. It proves that particles accelerate along the magnetic field, given that there is a parallel component of the electric field. This point will be recalled in future Sections. The equations for the in-plane components can be solved using the Landau variable $w = \dot{x} + i\dot{y}$. Combining Eqs. 2.2–2.3, one gets

$$\dot{w} + i\Omega w = \frac{q}{m} E_\perp, \tag{2.5}$$

where $\Omega = qB/m$. To solve this inhomogeneous differential equation, we have to look for the solution of the related homogeneous equation and the particular integral. The related homogeneous equation is $\dot{w} = -i\Omega w$ and its solution is

$$w(t) = w_0 e^{-i\Omega t}, \tag{2.6}$$

where $w(t = 0) = w_0$ and $w_0 = \dot{x}_0 + i\dot{y}_0 \equiv v_\perp e^{-i\phi}$, $v_\perp = \sqrt{\dot{x}_0^2 + \dot{y}_0^2}$ and

$\phi = \text{atan}(\dot{x}_0/\dot{y}_0)$ is the phase. Finally, substituting back the position of the Landau variable in Eq. 2.6, one gets

$$v_x(t) = v_\perp \cos(\Omega t + \phi), \tag{2.7}$$
$$v_y(t) = -v_\perp \sin(\Omega t + \phi), \tag{2.8}$$

i.e. in the absence of an electric field, the particle moves in a circular motion in the $xy$ plane, as it is well known. To find the particular integral we notice that the inhomogeneous term is a constant, so we can say the particular solution is a constant too, say $w_p = A$, and by substituting this solution in Eq. 2.5, one obtains $w_p = -iE_\perp/B$. The complete solution is then

$$w = v_\perp e^{-i(\Omega t+\phi)} - i\frac{E}{B},$$

and, the velocity components are $v_x(t) = v_\perp \cos(\Omega t+\phi)$, and $v_y(t) = -v_\perp \sin(\Omega t+\phi) - \frac{E_\perp}{B}$. The electric field perpendicular to the magnetic field causes a drift motion in the direction perpendicular to both the fields, independent of the nature of the particle. By integration, the particle orbit in 2D is given by

$$x(t) = \frac{v_\perp}{\Omega} \sin(\Omega t + \phi), \tag{2.9}$$
$$y(t) = \frac{v_\perp}{\Omega} \cos(\Omega t + \phi) - \frac{E_\perp}{B} t. \tag{2.10}$$

These are the equations describing a trochoid – a more general form of the cycloid – that is shown in Fig. 2.1 (Kivelson & Russell, 1995). The ratio

$$\frac{v_\perp}{\Omega} \equiv R_{_L} \tag{2.11}$$

is the radius of the particle's orbit, commonly known as the Larmor radius.

In the following Sections, we will study and describe the motion of charged particles in the self-consistent, time-dependent, non-uniform, simulations of plasma turbulence we have described in the previous Chapter.

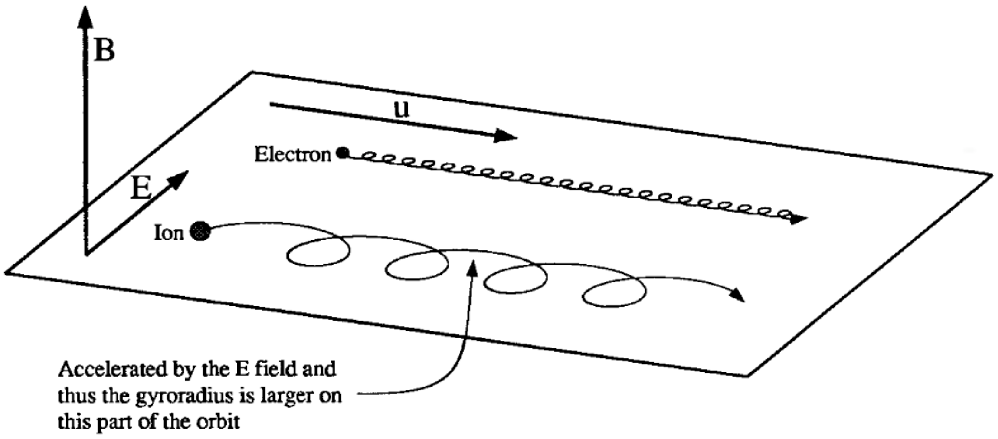


Figure 2.1: Schematic picture of the trajectories of charged particles in a uniform magnetic field $\boldsymbol{B}$, when a perpendicular electric field $\boldsymbol{E}$ is present. The motion along the magnetic field is not represented as it would have only the effect of bending the trajectories along $\boldsymbol{B}$ for the ions, and along $-\boldsymbol{B}$ for the electrons. The geometric shape of the motion is a trochoid (a generalization of the cycloid). Adapted from (Kivelson & Russell, 1995).

## 2.2 Single-particle motion

The analytical solution for charged particle trajectories in electromagnetic fields is usually limited to the case above and a few other particular examples. The reason becomes evident when looking at the trajectories of charged particles in simulations of plasma turbulence. Figure 2.2 shows the motion of some particles in the HPIC simulation described in Sec. 1.2.1. As the reader can notice, trajectories are pretty far from the idealized case described before. The perpendicular diffusion envisioned by early approaches becomes evident, with magnetic field irregularities and discontinuities taking the place of particle-particle collisions as scattering points. This evidence arises from the presence of "break-points" along the trajectories – sudden and unpredictable changes in their direction when encountering such irregularities. On the other hand, trapping phenomena also occur. Sometimes, the gyrating motion is confined within large magnetic structures and is not heavily disturbed by magnetic irregularities or discontinuities. This behavior is found both in small- and large-$\beta$ simulations (between which the average Larmor radius size changes as Fig. 2.2 shows, and as will be discussed in the following). The overall motion seems to be almost random: particles scatter and diffuse as they move, while also having the chance to be trapped for a certain amount of time.

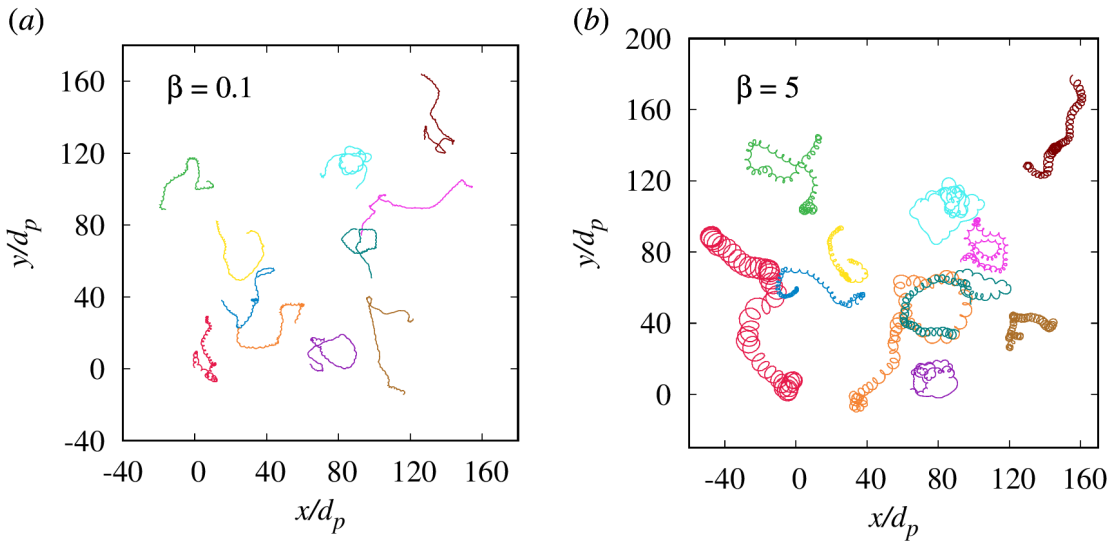


Figure 2.2: Particle trajectories in (a) low- and (b) high-$\beta$ plasmas. The difference in gyration radii size is due to high-$\beta$ particles having higher energies (recall that $\beta = 2v_{th}^2/v_A^2$). Also, the unpredictability of the motion is evident. Particles trapped in magnetic islands show closed orbits, while those that encounter magnetic irregularities display sharp turns of their trajectories. From Pecora et al. (2018).

Depending on the time-scale of interest, particle-to-turbulence scales ratio (see below), and different geometries, one can focus on different diffusive regimes, which are "anomalous" in the sense that they deviate from normal diffusion (Verkhoglyadova & Le Roux, 2005; Zimbardo et al., 2006). Generally, these regimes are of transient nature and some features may be recognized in the following analyses when looking at trapping (subdiffusion) and initial transients of the diffusion coefficient (ballistic). Also in 3D geometries (of which the 2.5D can be considered as a limit case), when the simulation is axisymmetric and anisotropic, the normal diffusive behavior is recovered for asymptotic times (Pommois et al., 2007). In the next Sections, we will focus on the normal diffusive motion, quantifying diffusion, and deriving analytical forms for the diffusion coefficient.

### 2.2.1 The Brownian diffusive motion

From the pictures of trajectories in Fig. 2.2, we have seen that particles do not follow an ideal trochoid, rather their motion seems quite stochastic (though correlated to magnetic field properties in some way that will be clarified in the following Sections). Because of the complexity and unpredictability of each singular trajec-

tory, it is important to provide a global, statistical description of the phenomenon; this implies large ensemble-averages, over particles, volume, and time. The turbulent, stochastic nature of fluctuations acting on plasma particles suggests that their motion can be described within the class of Brownian diffusion phenomena.

We start from the equation of diffusion and find its solution, following Einstein's approach (Einstein, 1905; Chandrasekhar, 1943; Abe & Thurner, 2005). Consider a group of particles whose motion is independent of one another. Let $\phi(\Delta)$ be the probability for a particle to move from its position $x$ to $x + \Delta$ in a single time step $\tau$, then $\phi(\Delta)$ satisfies

$$\int_{-\infty}^{+\infty} \phi(\Delta) d\Delta = 1, \tag{2.12}$$

$$\phi(\Delta) = \phi(-\Delta). \tag{2.13}$$

Let $P(x,t)$ be the probability of finding a particle at the position $x$, at the time $t$; one can write

$$P(x, t+\tau) = \int_{-\infty}^{+\infty} P(x+\Delta, t)\phi(\Delta) d\Delta. \tag{2.14}$$

For small $\tau$ and $\Delta$, one can expand in Taylor series

$$P(x, t+\tau) = P(x,t) + \frac{\partial P(x,t)}{\partial t}\tau, \tag{2.15}$$

$$P(x+\Delta, t) = P(x,t) + \frac{\partial P(x,t)}{\partial x}\Delta + \frac{1}{2}\frac{\partial^2 P(x,t)}{\partial x^2}\Delta^2, \tag{2.16}$$

and, recalling the properties in Eqs. 2.12–2.13 of $\phi(\Delta)$, one obtains

$$\frac{\partial P}{\partial t}\tau = \frac{1}{2}\frac{\partial^2 P}{\partial x^2}\int_{-\infty}^{+\infty} \Delta^2 \phi(\Delta) d\Delta. \tag{2.17}$$

The above equation is a diffusion equation with the diffusion coefficient $D$ defined as

$$D = \frac{1}{2\tau}\int_{-\infty}^{+\infty} \Delta^2 \phi(\Delta) d\Delta. \tag{2.18}$$

Equation 2.17 can be finally written in the more usual form:

$$\frac{\partial P}{\partial t} = D\frac{\partial^2 P}{\partial x^2}. \tag{2.19}$$

A solution of Eq. 2.19 is

$$P(x,t) = \frac{N}{\sqrt{4\pi Dt}}\, e^{-x^2/4Dt}, \tag{2.20}$$

with $N$ normalization constant that can be determined by imposing that $\int P(x,t)dx = 1$. In this case $N = 1$. Since the solution is the normal distribution, as expected since we are treating random displacements, one can evaluate the mean squared displacement by translating the solution, so that $x$ becomes the displacement $\Delta x$ rather than the absolute position, and $t$ becomes the time interval $\tau$. The width of the normal distribution defined in Eq. 2.20 is

$$2\sigma^2 = 4D\tau, \tag{2.21}$$

which is equivalent to

$$\langle(\Delta x)^2\rangle = 2D\tau. \tag{2.22}$$

Equation 2.22 is the well-known equation that describes the mean motion of elements moving in stochastic fields (Chandrasekhar, 1943; Batchelor, 1976; Wang et al., 2012). $\Delta x$ is the element's displacement with respect to the initial position $x_0 = x(t_0)$, $\langle \dots \rangle$ is an appropriate ensemble average, $\tau$ is the time interval for which $\Delta x = x(t_0 + \tau) - x(t_0)$ and $D$ is the diffusion coefficient. This equation is of primary importance in describing mixing in a wide variety of natural phenomena. The physical quantities that influence the random motion are gathered (and hidden) into the diffusion coefficient. The diffusion theories that will be presented look for an explicit form of $D$.

### 2.2.2 The diffusive behavior in plasma simulations

In this Section, we build some statistics based on the description given above, using HPIC simulation results, to quantify plasma charged particle diffusion. To verify the diffusive limit, a probability function $P(\Delta x, \tau)$ was built for particles having displacement $\Delta x$ in a time interval $\tau$. We can focus on displacements along one direction, say $x$, for the isotropy of the plane perpendicular to the mean field. These distributions show Gaussian cores with small tails (almost completely absent in the low-$\beta$ plasma), as can be seen in Fig. 2.3. It is evident that the

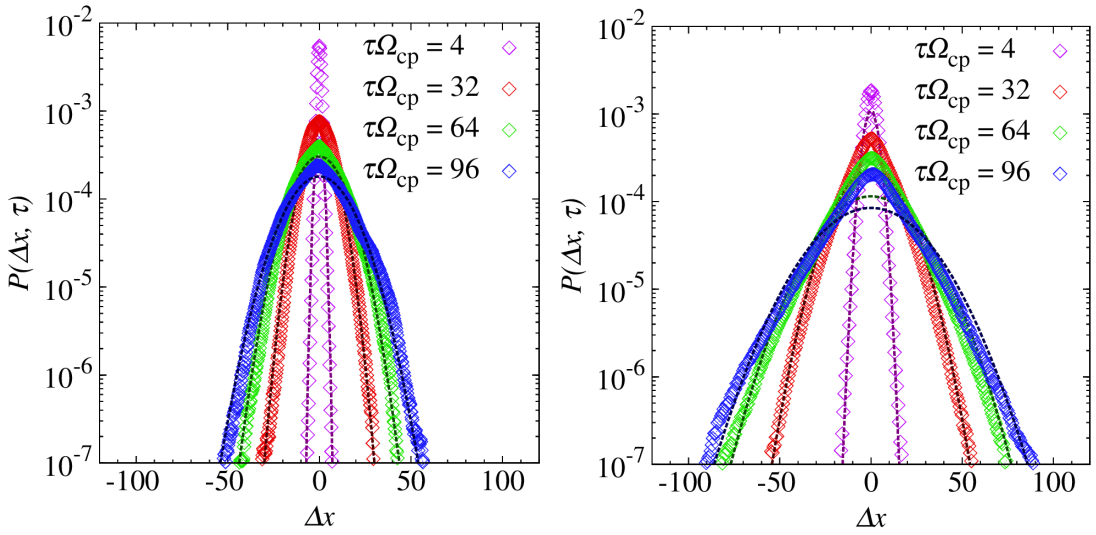


Figure 2.3: Measured probability for a particle having displacement $\Delta x$ in a time interval $\tau$, for different values of $\tau$, for (left) $\beta = 0.1$ and (right) $\beta = 5$. As expected from the Brownian diffusion theory, this probability has a Gaussian shape (dashed lines are Gaussian fits for the experimental data of the same color).

behavior depends on $\beta$. This dependence can be explained by saying that high-$\beta$ particles can have bigger displacement because they have higher energies, and they are weakly magnetized (they are less affected by the presence of magnetic field patterns). Low-$\beta$ particles, instead, have lower energies their wandering is more limited. In any case, the common feature is that the longer the time interval $\tau$, the farther particles spread.

We can measure the diffusive coefficient $D$, at different times, evaluating the width of the Gaussian functions that fit the accumulated probability functions, as shown in Fig. 2.3. The numerical values of the diffusion coefficients have been evaluated using Eq. 2.21 and are listed in Table 2.1. As we have already noticed by the shapes of the distribution functions, the diffusion coefficient is larger for high-$\beta$ particles and smaller for low-$\beta$ particles. Moreover, regardless of $\beta$, the diffusion coefficient grows in time until an asymptotic value is reached after $\sim 50 - 60$ cyclotron times.

Another measure for the diffusion coefficient can be obtained averaging the displacement over all particles and using Eq. 2.22 to fit the mean squared displacement shown in Fig. 2.4. The experimental diffusion coefficient values we obtain are $D(\beta = 0.1) = 1.10$ and $D(\beta = 5) = 1.45$. The linear fits have been performed after sufficiently long time intervals ($\tau \gtrsim 80\Omega_{cp}^{-1}$), when particles un-

| | $\tau\Omega_{cp}$ | $\sigma^2$ | $D$ |
|---|---|---|---|
| $\beta = 0.1$ | 4 | 2.51 | 0.31 |
| | 32 | 47.34 | 0.74 |
| | 64 | 112.14 | 0.88 |
| | 96 | 195.85 | 1.02 |

| | $\tau\Omega_{cp}$ | $\sigma^2$ | $D$ |
|---|---|---|---|
| $\beta = 5$ | 4 | 12.88 | 1.61 |
| | 32 | 182.22 | 2.85 |
| | 64 | 456.31 | 3.57 |
| | 96 | 621.53 | 3.24 |

Table 2.1: Diffusion coefficient $D$ calculated for different times, and for different $\beta$'s applying Eq. 2.21 to the Gaussian fits of Fig. 2.3.

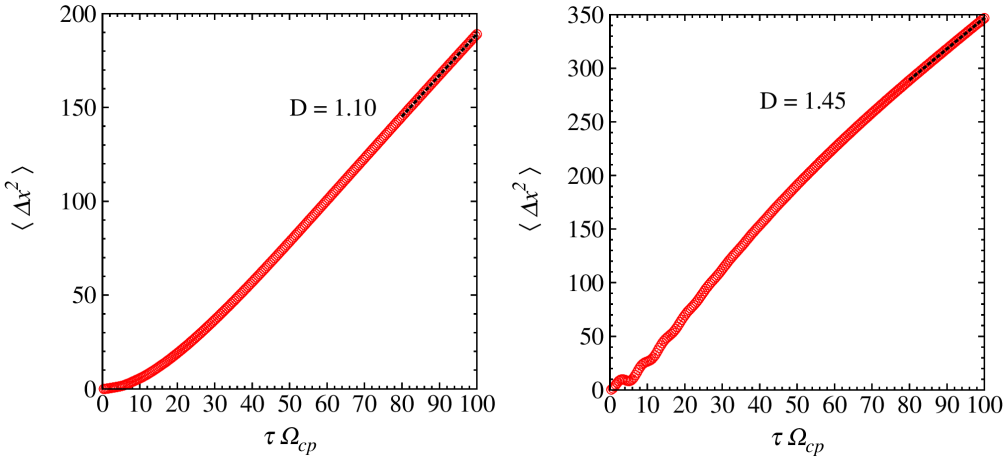


Figure 2.4: Mean squared displacement in the $x$ direction, averaged over all particles in (left) $\beta = 0.1$ and (right) $\beta = 5$ plasmas, as a function of the time interval $\tau$ (cyclotron units). For short time intervals the motion is ballistic ($\propto \tau^2$). For asymptotic times, the Brownian diffusion is attained ($\propto \tau$).

dergo Brownian diffusion. For short time intervals, particle motion cannot be stochastic for there exists a field correlation time during which particles sample a correlated field. This correlation time can be thought of as the time a particle needs to experience uncorrelated vortices. Only after this correlation time has elapsed the motion can become stochastic. There is a good agreement between the diffusion coefficients estimated using the probability function and the mean squared displacement at low and $\beta$ while there is some discrepancy at large $\beta$.

So far, we have performed averages over all the particles. This means also averaging over all the energies and found that the diffusion coefficient reaches an asymptotic value after a certain transient, and depends on the plasma $\beta$ – i.e. on particles' energy. To begin understanding more in detail the dependence of the diffusion coefficient on particles' energy, we divide particles into energy ranges and evaluate the running diffusion coefficient for every range using the time derivative

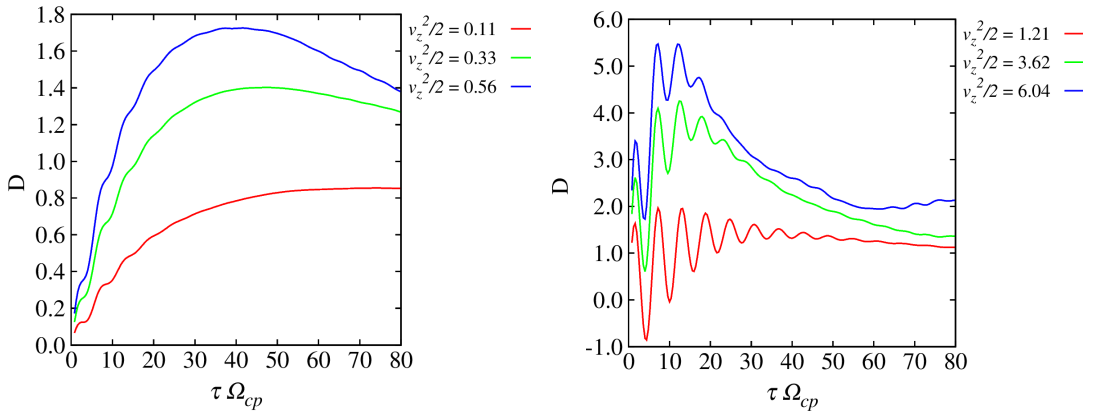


Figure 2.5: Running diffusion coefficient, computed via Eq. 2.23, for three different energy ranges for (left) low- and (right) high-$\beta$ simulations. For a given $\beta$, the diffusion coefficient $D$ explicitly depends on the parallel energy.

| | $v_z^2/2$ | $D$ | | $v_z^2/2$ | $D$ |
|---|---|---|---|---|---|
| | 0.11 | 0.83 | | 1.21 | 0.97 |
| $\beta = 0.1$ | 0.33 | 1.12 | $\beta = 5.0$ | 3.62 | 1.5 |
| | 1.56 | 1.10 | | 6.04 | 2.2 |

Table 2.2: Diffusion coefficients evaluated as the asymptotic values of Fig. 2.5 when particles achieve stochastic diffusion. Particles have been divided into different energy ranges ($v_z^2/2$ is the kinetic energy in the $z$ direction).

of Eq. 2.22,

$$D = \frac{1}{2}\frac{\partial\langle(\Delta x)^2\rangle}{\partial t}. \tag{2.23}$$

The above is known as the "running" diffusion coefficient. Figure 2.5 shows this diffusion coefficient as a function of the time interval, for different energy ranges, for the low- and high-$\beta$ plasmas. Energy ranges are based on the parallel kinetic energy (namely $v_z^2/2$). The choice of using this quantity rather than the total kinetic energy will be explained in Sec. 2.6. The asymptotic values are the Brownian diffusion coefficients, reported in Table 2.2. From Fig. 2.5 we can see, again, the same behavior suggested by previous analyses: the diffusion coefficient is proportional to $\beta$. More interestingly, for a given $\beta$, one can notice that the diffusion coefficient depends explicitly on energy (Ruffolo et al., 2012).

In the following Sections, we will describe some of the most common diffusion theories that look for an explicit form of the diffusion coefficient in different approximations, as well as deriving a new analytical form for the diffusion coefficient that depends on plasma properties.

## 2.3 The field line random walk theory

One of the first diffusion theories developed for plasmas is the field line random walk theory (FLRW), owed to Jokipii and Parker (1969). This theory is valid for high-energy particles, moving in a turbulent magnetic field with a mean component. The focus on high-energy particles maintains the approach to a relatively easy mathematical level. Indeed, trajectories of high-energy particles are less affected by magnetic discontinuities and can be strictly related to the motion of magnetic field lines themselves. Figure 2.6 (Jokipii & Parker, 1969) is a schematic representation of the process of magnetic field lines being mixed by the random horizontal (parallel to Sun's surface) velocity field that produces this random walk.

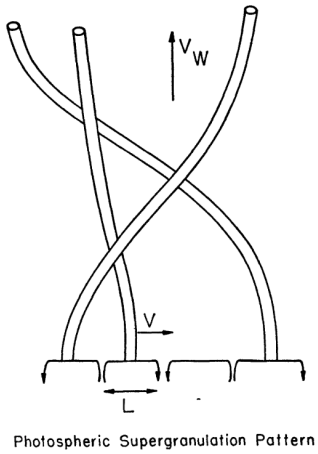


FIG. 4.—Schematic illustration of the field-line random walk generated by the turbulent motions in the photosphere. A typical element of fluid moves a distance $L$ at velocity $V$, and a cell lasts a time $\tau = L/V$. The field lines are convected out by the solar wind at velocity $V_w$, which is several times the Alfvén velocity.

Figure 2.6: Adapted from Jokipii and Parker (1969).

This correlation between the velocity and large-scale magnetic field can be directly seen from Faraday's law

$$\frac{\partial \boldsymbol{B}}{\partial t} = -\boldsymbol{\nabla} \times \boldsymbol{E}$$

with the large-scale electric field $\boldsymbol{E}$ given by the MHD term $\boldsymbol{E} = -\boldsymbol{u} \times \boldsymbol{B}$, so that

$$\frac{\partial \boldsymbol{B}}{\partial t} = \boldsymbol{\nabla} \times (\boldsymbol{u} \times \boldsymbol{B}).$$

This means that magnetic field lines displacement is as stochastic as that of the velocity field. This transfer of stochastic properties – from the velocity field

to the magnetic field – results in the perpendicular (with respect to the mean magnetic field) diffusion of energetic particles. The explicit form of the perpendicular diffusion coefficient is now obtained following the classical derivation, with the approximations stated above. The magnetic field can be written as composed by a mean component $B_0\hat{e}_z$, and a fluctuating part $\delta\boldsymbol{B}(\boldsymbol{r})$ with zero average, and amplitude $\delta B \ll B_0$,

$$\boldsymbol{B}(\boldsymbol{r}) = \delta\boldsymbol{B}(\boldsymbol{r}) + B_0\hat{e}_z.$$

Magnetic field lines are defined by the equations

$$\frac{dx}{B_x} = \frac{dy}{B_y} = \frac{dz}{B_z}, \tag{2.24}$$

and we focus on solving

$$\frac{dx}{B_x} = \frac{dz}{B_z},$$

which means

$$dx = \delta B_x \frac{dz}{B_0},$$

and integrating both sides we have

$$\Delta x = \frac{1}{B_0}\int_0^{\Delta z} dz\, \delta B_x.$$

It is interesting to notice that, since $\langle B_x\rangle = \langle B_y\rangle = 0$ (as they are zero-average fluctuations by definition) it is also $\langle \Delta x\rangle = \langle \Delta y\rangle = 0$. What is different from zero is the mean squared displacement $\langle \Delta x^2\rangle$, that is

$$\langle \Delta x^2\rangle = \frac{1}{B_0^2}\int_0^{\Delta z} dz' \int_0^{\Delta z} dz'' \langle \delta B_x(x_0, y_0, z')\delta B_x(x_0, y_0, z'')\rangle. \tag{2.25}$$

Defining the two-point correlation tensor

$$C_{ij}(\eta, \psi, \zeta) = \langle B_i(x, y, z)B_j(x + \eta, y + \psi, z + \zeta)\rangle,$$

and making the position $z'' = z' + \Delta z$, Eq. 2.25 becomes

$$\langle \Delta x^2 \rangle = \frac{1}{B_0^2} \int_0^{\Delta z} dz' \int_{-z'}^{\Delta z - z'} d\zeta \; C_{xx}(0,0,\zeta).$$

Since the diffusive behavior is achieved for large scales, the two-point correlation tensor can be safely integrated from $-\infty$ to $+\infty$ giving the expression

$$\langle \Delta x^2 \rangle = \frac{1}{B_0^2} \Delta z \int_{-\infty}^{+\infty} d\zeta \; C_{xx}(0,0,\zeta). \tag{2.26}$$

In the original work, the authors were interested in time variations while particles move in a 3D space, as in the case of solar wind expansion. Equation 2.26 can depend explicitly on time since $\Delta z = v_z \Delta t$, where $v_z$ is the particle velocity along the $z$ direction. The FLRW diffusion coefficient can be expressed as

$$D_{FLRW} = \frac{\langle \Delta x^2 \rangle}{\Delta t} = \frac{v_z}{B_0^2} \int_{-\infty}^{+\infty} d\zeta \; C_{xx}(0,0,\zeta) \simeq \frac{v_z \lambda_{_C}}{B_0^2} \delta B_x^2, \tag{2.27}$$

where $\lambda_{_C}$ is the correlation length along the $z$ direction. The above expression has been successfully used in the past decades to describe the diffusion of magnetic field lines in the solar wind. Unfortunately, this expression of the diffusion coefficient is of little to no use for our purposes since the HPIC simulations have been performed in a 2.5D geometry and it is not possible to evaluate a correlation length in the parallel direction. In fact, the correlation length is defined as the length $\boldsymbol{\ell}$ at which the correlation function $C(\boldsymbol{\ell})$ drops at $1/e$, with

$$C(\boldsymbol{\ell}) = \frac{1}{\langle |B(\boldsymbol{r})|^2 \rangle} \int \boldsymbol{B}(\boldsymbol{r} + \boldsymbol{\ell}) \cdot \boldsymbol{B}(\boldsymbol{r}) \; d\boldsymbol{r}, \tag{2.28}$$

and in the 2.5D case, the increment $\boldsymbol{\ell}$ cannot have a $z$ component. In the following, we will present a theory that uses Lagrangian properties to determine the diffusion coefficient.

## 2.4 The Bieber and Matthaeus theory

The next theory we want to describe has been proposed by Bieber and Matthaeus (1997) and is commonly referred to as the BAM theory. A new sight on the perpendicular scattering theory is needed, as the FLRW is valid only for very high-energy particles restricted to turbulent systems with fluctuation amplitudes small compared to mean values. Like several diffusion theories, BAM derives the

perpendicular diffusion coefficient using the Taylor-Green-Kubo (TGK) formulation that is based on the velocity autocorrelation function (G. I. Taylor, 1922; Green, 1951; Kubo, 1957). The diffusion coefficient defined with TGK is

$$D_{ij} = \int_0^\infty \langle v_i(t_0) \cdot v_j(t_0 + \tau) \rangle d\tau \equiv \int_0^\infty C_{v_{ij}}(\tau) d\tau. \tag{2.29}$$

This deceptively simple starting point involves explicitly particles velocity, that can be related to other fields (as it can be seen from Eqs. 1.22–1.25). The hard problem is to figure out the right expression for the velocity correlation function $C_{v_{ij}}$.

Note that particle transverse velocities are gyro-periodic if particles would move in a fluctuation-free field, but fluctuations make the two-time correlation function no longer perfectly recurrent. The simplest modeling of this phenomenon is the following approximation (say in the $x$ direction)

$$C_{v_{xx}}(\tau) \propto \cos(\Omega\tau) e^{-\tau/\tau_c}, \tag{2.30}$$

where the proportionality constant is $v^2/3$, with $v$ being the particle (perpendicular thermal) velocity, $\Omega$ is the gyration frequency and $\tau_c$ is the correlation (or Lagrangian) time. As we have seen in previous Sections, this particular time is important since it separates two different kinds of motion. The transient motion, for times shorter than the correlation time, is the so-called "ballistic" regime during which particles spread quickly ($\langle \Delta x^2 \rangle \propto t^2$). The stationary regime of Brownian diffusion, at which each particle experience an uncorrelated field, is achieved for intervals longer than $\tau_c$. This time can be estimated by means of the auto-correlation function (Servidio et al., 2016). The Lagrangian time is

$$\tau_c = \frac{1}{\langle v_x(t_0)^2 \rangle} \int_0^\infty \langle v_x(t_0) v_x(t_0 + \tau) \rangle d\tau. \tag{2.31}$$

In the above definition, the operation $\langle \dots \rangle$ is the average over all particles. Evaluating this time lag in HPIC simulations suggest that particles with higher energies reach the diffusive behavior sooner than their less energetic counterpart that, instead, experience longer trapping times

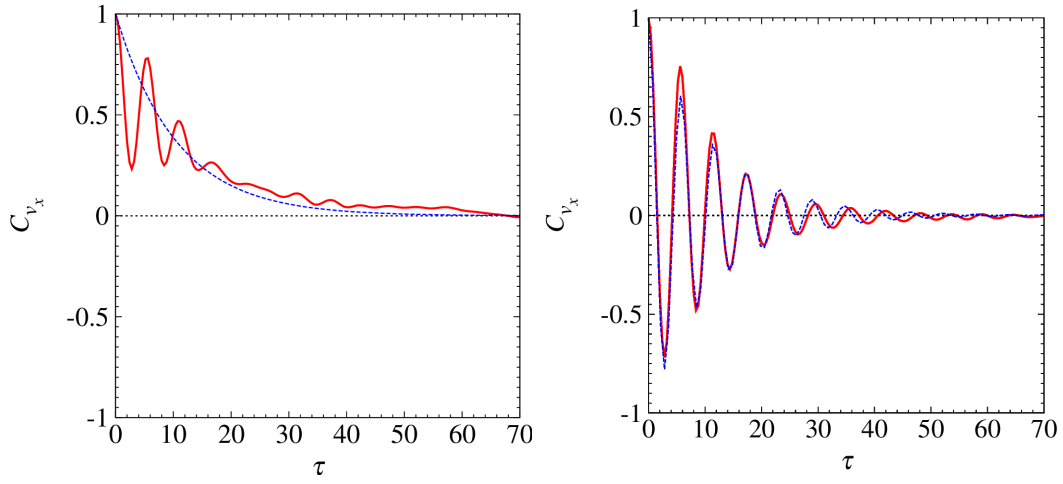


Figure 2.7: Two-time velocity correlation function for (left) $\beta = 0.1$ and (right) $\beta = 5$ in the HPIC simulations. Dashed lines are the best fits with the approximate form of Eq. 2.30.

$$\tau_c(\beta = 5.0) = 0.95\Omega_{cp}^{-1},$$
$$\tau_c(\beta = 0.5) = 4.13\Omega_{cp}^{-1},$$
$$\tau_c(\beta = 0.1) = 9.64\Omega_{cp}^{-1}.$$

We find the form in Eq. 2.30 to describe quite well the correlation function for high $\beta$'s, reasonably well for intermediate $\beta$, while, for our simulations, fails at low $\beta$, as can be seen in Fig. 2.7.

By integrating Eq. 2.30, using the TGK formulation, one obtains the perpendicular diffusion coefficient as

$$D_{xx} = \frac{v^2}{3}\int_0^\infty d\tau\ \cos(\Omega\tau)e^{-\tau/\tau_c} = \frac{v^2}{3}\frac{\tau_c}{1+\Omega^2\tau_c^2},$$

that can be made dependent on the Larmor radius $R_{_L} = v/\Omega$ as

$$D_{xx} = \frac{vR_{_L}}{3}\frac{\Omega\tau_c}{1+\Omega^2\tau_c^2}. \tag{2.32}$$

This prediction has been evaluated by calculating the average thermal perpendicular velocity, the average Larmor, and the correlation time using Eq. 2.31. The results are reported in Table 2.3. The comparison of the numerical values of the diffusion coefficient obtained with the BAM theory with the experimental values obtained before (Table 2.2) shows that this theory underestimates the diffusion coefficient, as already found in literature (Matthaeus et al., 2003). This

| $\beta$ | $D_{xx}$ |
|---|---|
| 0.1 | 0.005 |
| 0.5 | 0.043 |
| 5 | 0.790 |

Table 2.3: Perpendicular diffusion coefficients for the HPIC simulations evaluated using the BAM theory at different $\beta$'s. Recall that, from HPIC simulation analysis reported in Table 2.2, $D_{xx}(\beta = 0.1) \sim 0.8$–$1.1$ and $D_{xx}(\beta = 5) \sim 1.0$–$2.2$.

can be due to the modeling used for the correlation function in Eq. 2.30. The description is that of orbits that become non-perfectly recurrent because of any non-energy-changing random fluctuations, no properties of the system are explicitly present. As will be shown below, when considering actual fluctuations of a turbulent magnetic field, the description of the diffusion coefficient becomes more accurate; especially when considering low-$\beta$ plasmas in which particles have lower energies and are more affected by turbulent fluctuations.

In the following Section, we will obtain an analytical form of the diffusion coefficient using a more refined theory.

## 2.5 The nonlinear guiding center theory

The last theory we are going to explore is the nonlinear guiding center (NLGC) theory (Matthaeus et al., 2003). This theory solves the main problems of the two previous approaches: it can treat particles in a wide range of energies, and it also takes into account the spectral distribution of the magnetic field. This is a 3D theory in which the transverse turbulent structures decorrelate particle trajectories after parallel scattering. The starting point of the theory is again the TGK formulation, with a new model for the two-time velocity correlation function. The idea is to focus on particles' gyrocenters as they are scattered while following magnetic field lines (Shalchi & Dosch, 2008; Shalchi, 2015). Assuming that particles' gyrocenters follow magnetic field lines, their velocity can be estimated using Eqs. 2.24. The velocity of the gyrocenters, e.g. in the $x$ direction, is given by

$$v_{g_x} = a v_z \frac{B_x}{B_0}, \tag{2.33}$$

where $a$ is a proportionality constant and $v_z$ is the particle velocity in the $z$ direction. The form of the velocity in Eq. 2.33 transforms the two-time correla-

tion function into a fourth-order correlator, and the diffusion coefficient in the $x$ direction is

$$D_{xx} = \frac{a^2}{B_0^2}\int_0^\infty d\tau \langle v_z(0) B_x(\boldsymbol{x}(0),0) v_z(\tau) B_x(\boldsymbol{x}(\tau),\tau)\rangle,$$

where $B_x(\boldsymbol{x}(\tau),\tau)$ is the Lagrangian magnetic field, i.e. the magnetic field measured at particle position $\boldsymbol{x}(\tau)$. Assuming that velocity and magnetic field fluctuations are uncorrelated, the fourth-order correlation function can be split in the product of two second-order correlation functions

$$D_{xx} = \frac{a^2}{B_0^2}\int_0^\infty d\tau \langle v_z(0) v_z(\tau)\rangle \langle B_x(\boldsymbol{x}(0),0) B_x(\boldsymbol{x}(\tau),\tau)\rangle. \tag{2.34}$$

The two-time velocity correlation function can be modeled by the isotropic assumption

$$\langle v_z(0) v_z(\tau)\rangle = \frac{v^2}{3} e^{-v\tau/\lambda_\parallel},$$

where $v$ is the particle speed and $\lambda_\parallel$ is the mean free path in the $z$ direction. The Lagrangian magnetic autocorrelation tensor can be rewritten using Corrsin's independence hypothesis that is very common in astrophysical studies. It can be used when long time intervals or, equivalently, when distances larger than a correlation length are considered. With this approximation, it is possible to separate the statistics of the magnetic field from that of particles. This means that it is possible to write the Lagrangian correlation function as the Eulerian one using the displacement probability density as a weight (Corrsin, 1959; Salu & Montgomery, 1977; McComb, 1990; Ruffolo et al., 2004; Tautz & Shalchi, 2010), obtaining

$$\langle B_x(\boldsymbol{x}(0),0) B_x(\boldsymbol{x}(\tau),\tau)\rangle = \int d\boldsymbol{r}\; R_{xx}(\boldsymbol{r},\tau) P(\boldsymbol{r},\tau),$$

where $R_{xx}(\boldsymbol{r},\tau)$ is the Eulerian two-point two-time magnetic field correlation tensor, and $P(\boldsymbol{r},\tau)$ is the probability function of the particle having displacement $\boldsymbol{r}$ after a time interval $\tau$ (same as in the previous Sections, except here we used $\boldsymbol{r}$ instead of $\Delta x$). The Eulerian two-point two-time magnetic field correlation can be written in terms of its Fourier transform $R_{xx}(\boldsymbol{r},\tau) = \int d\boldsymbol{k} S_{xx}(\boldsymbol{k},\tau) e^{i\boldsymbol{k}\cdot\boldsymbol{r}}$ and, for convenience, the dependencies of the spectral amplitude can be separated as $S_{xx}(\boldsymbol{k},\tau) = S_{xx}(\boldsymbol{k})\Gamma(\boldsymbol{k},\tau)$. The term $\Gamma(\boldsymbol{k},\tau)$ represents the time-propagator of the spectrum. Usually, this functional form is described via the so-called sweeping

decorrelation mechanism, namely $\Gamma(\boldsymbol{k},\tau) \sim e^{-\tau/\tau_c(\boldsymbol{k})}$, where $\tau_c(\boldsymbol{k})$ is a characteristic decorrelation time. The latter is usually thought to be the the "sweeping decorrelation time" (Chen & Kraichnan, 1989; Nelkin & Tabor, 1990), in analogy with fluid turbulence. With these positions, the integral in Eq. 2.34 can be rewritten as

$$D_{xx} = \frac{a^2}{B_0^2}\int_0^\infty d\tau\ \frac{v^2}{3}e^{-\upsilon\tau/\lambda_\parallel}\int d\boldsymbol{r}\ P(\boldsymbol{r},\tau)\int d\boldsymbol{k}\ S_{xx}(\boldsymbol{k})e^{-\tau/\tau_c(\boldsymbol{k})}e^{i\boldsymbol{k}\cdot\boldsymbol{r}}. \tag{2.35}$$

Knowing that the probability function $P(\boldsymbol{r},\tau)$ is normal, and taking into account the isotropy of the perpendicular plane, it can be written as $P(\boldsymbol{r},\tau) = e^{-r_\perp^2/D_{xx}\tau}e^{-z^2/D_\parallel\tau}$, with $r_\perp^2 = x^2+y^2$, and the $\boldsymbol{r}$ integration can be readily solved, giving

$$D_{xx} = \frac{a^2v^2}{3B_0^2}\int d\boldsymbol{k}\ \frac{S_{xx}(\boldsymbol{k})}{\frac{v}{\lambda_\parallel} + (k_x^2+k_y^2)D_{xx} + k_z^2D_\parallel + \frac{1}{\tau_c(\boldsymbol{k})}}. \tag{2.36}$$

A comparison of the diffusion coefficient evaluated with these three theories, as a function of the energy, has been made in previous test-particles works. Adapted from Matthaeus et al. (2003), we report here this result in Fig. 2.8.

The NLGC approach is able to describe test-particle simulations with remarkable precision. The FLRW is an upper limit since it describes high-energy particles via the magnetic field random motion. The BAM underestimates the diffusion coefficient, especially at low energies as also found with HPIC simulation in the previous Sec. 2.4. In the next Section, we will develop a 2D version of the NLGC theory to describe diffusion in 2.5D simulations of plasma turbulence.

## 2.6 2D nonlinear guiding center theory

All the theories described in previous Sections were developed for 3D systems and have been validated via test-particle simulations, and observations (Bieber et al., 2004; Shalchi et al., 2004). Among them, NLGC provides an accurate prediction of the diffusion coefficient as Fig. 2.8 shows. In the current Section, the analytical derivation of a 2D version of NLGC is presented. The necessity of this complementary version arises because 3D simulations are quite expensive, and not always indispensable since solar wind turbulence can be very often described with 2D approximation (Dasso et al., 2005; Oughton et al., 2015; Servidio et al.,

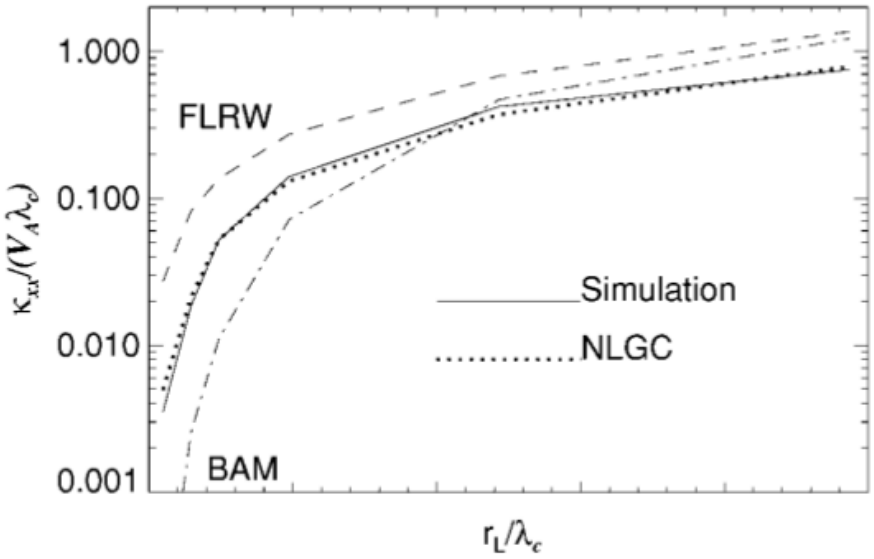


Figure 2.8: Comparison of the diffusion coefficient $\kappa_{xx}$ ($D_{xx}$ in our notation) normalized to the Alfvén speed $V_A$ and the correlation length $\lambda_c$ in the $z$ direction as a function of the Larmor radius $r_L$ i.e. as a function of the particle magnetization. The NLGC approach is the one that fits better the numerical data obtained in 3D simulations with test particles. Adapted from Matthaeus et al. (2003)

2015). In this Section, it will also be presented the validation with the HPIC self-consistent plasma turbulence simulations described in Sec. 1.2.1. The comparison with FPIC simulations described in Sec. 1.2.2 will be presented in Sec. 2.8.

The starting point is, as for the 3D version, the TGK formulation of the diffusion coefficient when particle gyromotion is considered. With the hypothesis of homogeneous turbulence, one can write the diffusion coefficient along one direction without loss of generality. For instance, along the $x$ direction, the diffusion coefficient $D_{xx}$, can be expressed as

$$D_{xx} = \frac{1}{B_0^2}\int_0^\infty d\tau \langle v_z(0)B_x(\boldsymbol{x}(0),0)v_z(\tau)B_x(\boldsymbol{x}(\tau),\tau)\rangle,$$

We assume that the magnetic field fluctuations in the perpendicular plane are totally uncorrelated with the velocity in the $z$ direction, and this allows the separation of the terms in the averaging operation as

$$D_{xx} = \frac{1}{B_0^2}\int_0^\infty d\tau \langle v_z(0)v_z(\tau)\rangle\langle B_x(\boldsymbol{x}(0),0)B_x(\boldsymbol{x}(\tau),\tau)\rangle.$$

Here the derivation separates from that of the 3D case. We assume that the

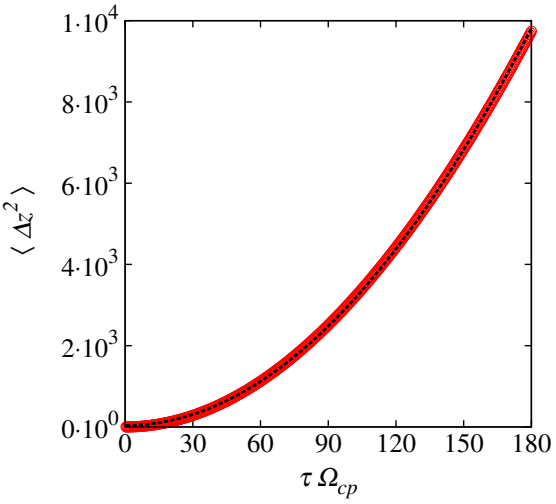


Figure 2.9: Mean squared displacement in the $z$ direction averaged over all particles as a function of $\tau$. The dashed line is the parabolic fit ($\propto \tau^2$). This same behavior is recovered for all simulations at different $\beta$'s (only one case shown here), confirming the assumption of particles free-streaming along the mean magnetic field to be solid.

velocity correlation function in the $z$ direction can be modeled as

$$\langle v_z(0)v_z(\tau)\rangle \sim v_z^2. \tag{2.37}$$

This assumption has been directly proved valid by measuring the quantity $\langle v_z(0)v_z(\tau)\rangle$ in our simulations. Figure 2.9 shows that particles are essentially free-streaming in the $z$ direction, hence $\langle \Delta z^2\rangle \propto t^2$, and therefore the velocity $v_z$ is, on average, constant.

Using this approximation, we can estimate the diffusion coefficient, neglecting the parallel scattering, as

$$D_{xx} = \frac{v_z^2}{B_0^2}\int_0^\infty d\tau\ \langle B_x(\boldsymbol{x}(0),0)B_x(\boldsymbol{x}(\tau),\tau)\rangle.$$

Again, we use Corrsin's independence hypothesis to transform the integrand function as

$$\langle B_x(\boldsymbol{x}(0),0)B_x(\boldsymbol{x}(\tau),\tau)\rangle = \int d\boldsymbol{r}\ R_{xx}(\boldsymbol{r},\tau)P(\boldsymbol{r},\tau).$$

The diffusion coefficient is then

$$D_{xx} = \frac{v_z^2}{B_0^2}\int_0^\infty d\tau \int d\boldsymbol{r}\; R_{xx}(\boldsymbol{r},\tau)P(\boldsymbol{r},\tau),$$

where $R_{xx}(\boldsymbol{r},\tau)$ is the Eulerian two-point two-time correlation tensor and $P(\boldsymbol{r},\tau)$ is the probability function of the particle having spatial displacement $\boldsymbol{r}$ after a time interval $\tau$. Now, we make use of the same transformations used in the previous Section to express $R_{xx}(\boldsymbol{r},\tau)$ using its Fourier transform

$$R_{xx}(\boldsymbol{r},\tau) = \int d\boldsymbol{k}\; S_{xx}(\boldsymbol{k},\tau)e^{i\boldsymbol{k}\cdot\boldsymbol{r}}.$$

We model $S_{xx}(\boldsymbol{k},\tau) = S_{xx}(\boldsymbol{k})\Gamma(\boldsymbol{k},\tau)$, and $\Gamma(\boldsymbol{k},\tau) \sim e^{-\tau/\tau_c(\boldsymbol{k})}$, where $\tau_c(\boldsymbol{k})$ is the characteristic sweeping decorrelation time (see below). At this point, we can proceed with the derivation of the diffusion coefficient, given by

$$D_{xx} = \frac{v_z^2}{B_0^2}\int_0^\infty d\tau \int d\boldsymbol{k}\; S_{xx}(\boldsymbol{k})\Gamma(\boldsymbol{k},\tau)\int d\boldsymbol{r}\; P(\boldsymbol{r},\tau)e^{i\boldsymbol{k}\cdot\boldsymbol{r}}. \tag{2.38}$$

Since $P$ is Gaussian, then

$$\int d\boldsymbol{r}\; P(\boldsymbol{r},\tau)e^{i\boldsymbol{k}\cdot\boldsymbol{r}} = e^{-(k_x^2 D_{xx}+k_y^2 D_{yy})\tau}.$$

In axisymmetric turbulence $D_{xx} = D_{yy} \equiv D$, $S_{xx} = S_{yy} \equiv S$, since we have only in-plane structures (i.e. $k_z = 0$) $k_x^2 + k_y^2 \equiv k^2$, and the diffusion coefficient is

$$D = \frac{v_z^2}{B_0^2}\int d\boldsymbol{k}\; S(\boldsymbol{k})\int_0^\infty d\tau\; e^{-k^2 D\tau}e^{-\tau/\tau_c(\boldsymbol{k})}.$$

Finally, integrating over $\tau$, one gets

$$D = \frac{v_z^2}{B_0^2}\int d\boldsymbol{k}\; \frac{S(\boldsymbol{k})}{[\tau_c(\boldsymbol{k})]^{-1} + k^2 D}. \tag{2.39}$$

Note that this prediction is only a small modification to the original NLGC theory, having suppressed the $z$-dependence by using the free streaming behavior of particles along $z$ (Eq. 2.37).

It is possible to obtain a first estimate of the diffusion coefficient assuming that the sweeping decorrelation time is long (as in the case of large scale slow driving, for example), therefore the term $\tau_c(k)^{-1}$ in Eq. 2.39 can be neglected to obtain the approximate form

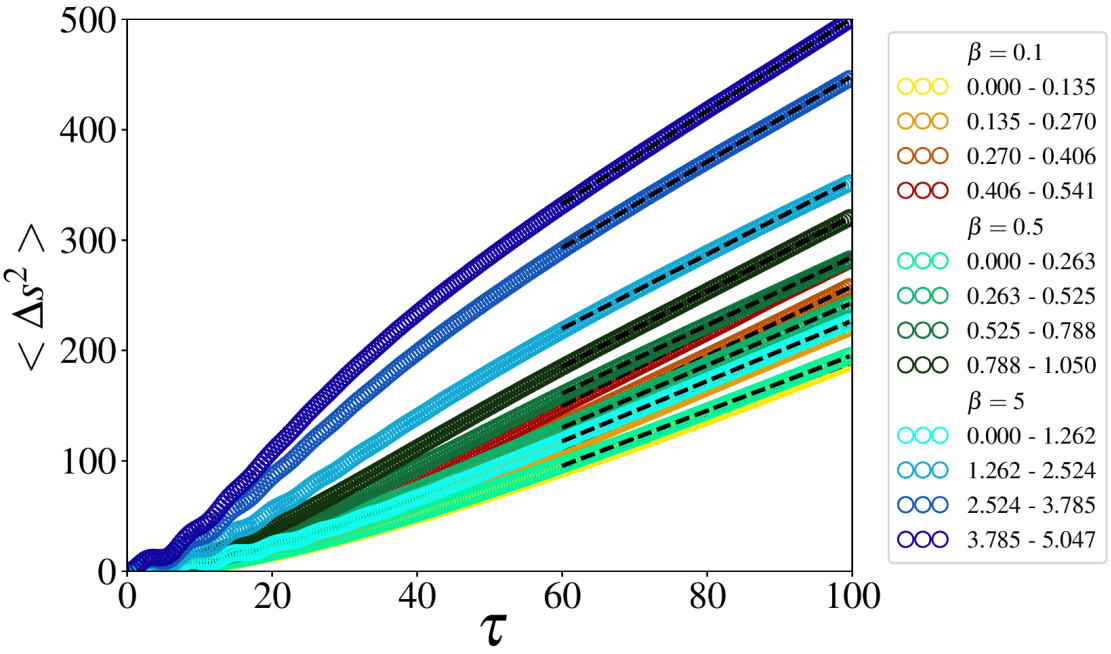


Figure 2.10: Mean squared displacement in the perpendicular plane as a function of the time interval $\tau$ (cyclotron units), for several ranges of particles' energy (normalized to the square of Alfvén velocity $v_A^2$), indicated in the label, for the three different $\beta$ values. Normal diffusion is achieved for $\tau \gtrsim 60\Omega_{ci}^{-1}$, where we extrapolate the values of the perpendicular diffusion coefficient via linear fits (dashed lines). From Pecora et al. (2018).

$$D^* = \sqrt{\frac{v_z^2}{B_0^2} \int d\boldsymbol{k} \frac{S(\boldsymbol{k})}{k^2}}. \tag{2.40}$$

To estimate the theoretical values of the diffusion coefficient via Eqs. 2.39–2.40, we computed the average power spectrum $S(\boldsymbol{k})$, of magnetic fluctuations. The experimental values of the diffusion coefficient have been obtained in a similar fashion to Fig. 2.4. Because of the isotropy of the perpendicular plane already invoked before, now instead of measuring $\Delta x^2$ we measure $\Delta s^2 = \Delta x^2 + \Delta y^2$. Moreover, particles have been divided into energy bins and a few of them (for clarity's sake) are shown in Fig. 2.10.

Figure 2.11 shows the experimental values of $D$ obtained by fitting particles mean squared displacements in Fig. 2.10 with Eq. 2.22 ($\langle \Delta s^2 \rangle = 2D\tau$) . The theoretical values of the 2D-NLGC, evaluated via both the exact (Eq. 2.39) and the approximated (Eq. 2.40) formulas, are reported as a function of the particles' energies. The simulations results follow very well the theoretical prediction at low

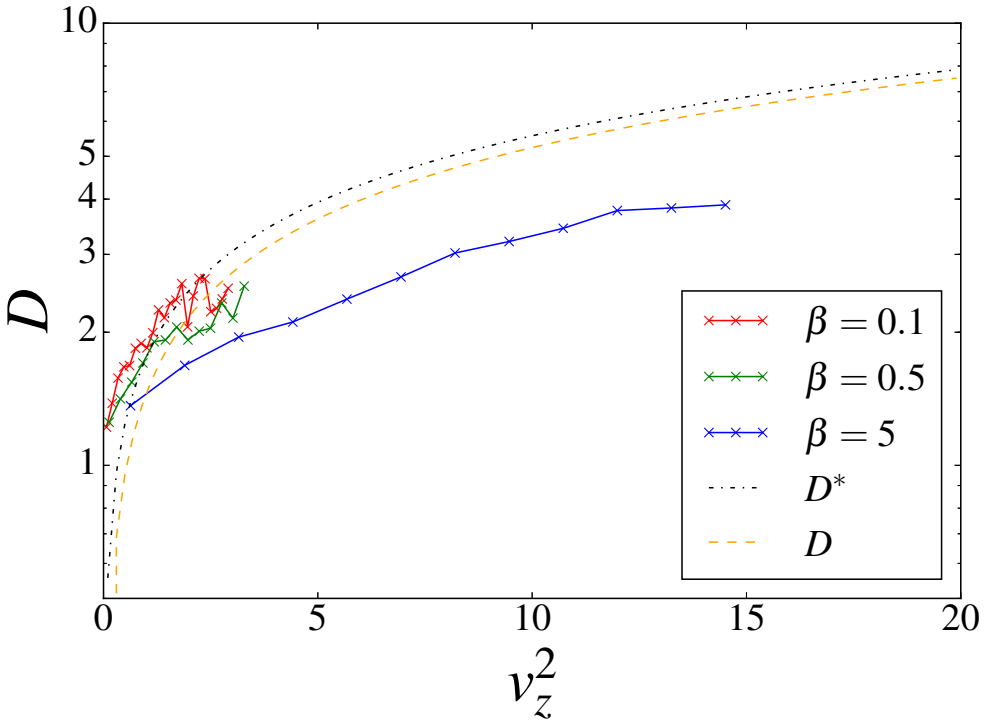


Figure 2.11: The 2D-NLGC diffusion coefficient as a function of the parallel energy $v_z^2$. The theoretical exact (orange dashed from Eq. 2.39) and approximated (black dotted from Eq. 2.40) display a monotonic behavior. Experimental measures follow the predictions very well for low- and mid-$\beta$ plasmas. The large $\beta$ shows systematic underestimation, though retaining the same monotonic increase. From Pecora et al. (2018).

$\beta$. The theory slightly deviates at large $\beta$, although the functional monotonic behavior is very similar. Departures of experimental data from the theoretical expectations can be expected when considering technical issues on the classification of particles. As will be shown in the following, lower-energy particles are those which are more prone to gain energy (changing their velocity modulus), thus generating some ambiguity when energy binning is performed. Also, higher-energy classes (especially for low-$\beta$ plasmas) are less populated and become less statistically relevant.

Lastly, we briefly investigate the decorrelation mechanism in self-consistent plasma turbulence. We performed a Fourier transform in time of magnetic fluctuations, computing the propagator $\Gamma(k, \tau)$, as described in Servidio, Carbone, et al. (2011); Perri et al. (2017). As in fluid, MHD, and Hall MHD models of turbulence, this time-dependent correlation of turbulence strongly depends on the amplitude

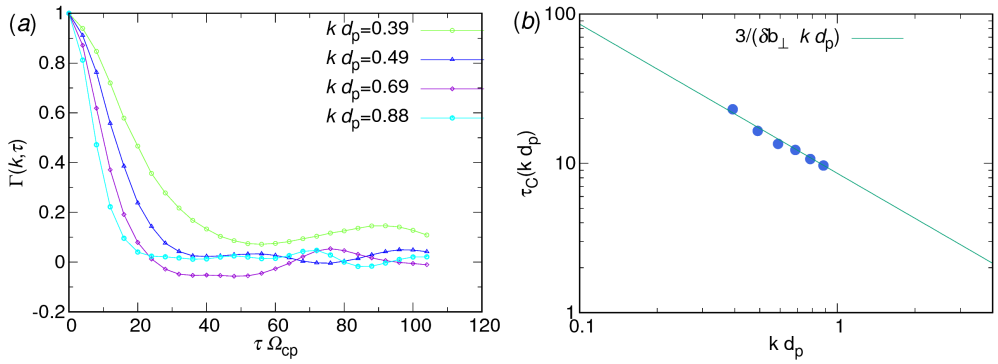


Figure 2.12: (a) Propagator of the magnetic field spectrum, computed for several (perpendicular) $k$ modes in the inertial range of plasma turbulence. (b) Decorrelation time as a function of $k$ (blue bullets), computed as the $e$-folding time of the functional form in (a). The sweeping prediction is reported with the solid teal line.

of $k$, as reported in Fig. 2.12. The decorrelation mechanism depends on $k$ and drops quickly in time (only a few inertial range modes are reported). From this functional form, we computed the decorrelation time $\tau_c(k)$, represented in panel (b) of the same figure. The decorrelation time scales as $\sim 1/k$, indicating a clear dominance of the sweeping effect (Servidio, Carbone, et al., 2011). To be more quantitative in computing the diffusion coefficient for our experiment, we found that $\tau_c(k) \sim 3/(\delta b_\perp k d_p)$, where $\delta b_\perp$ is the root-mean-square (rms) of the in-plane magnetic fluctuations.

The effect of large eddies is to randomly sweep the inertial range fluctuations through the Eulerian probe, resulting in a local Taylor (frozen in) effect. Together with the Alfvén propagation effect, these are the main causes of time-decorrelation.

This conclusion is complementary to earlier observations and computations in hydrodynamics (Orszag & Patterson, 1972; Sanada & Shanmugasundaram, 1992; Zhou et al., 1993). The shape of large eddies is not expected to be strongly influenced by sweeping motion or straining at inertial-range scales. Indeed, as Fig. 2.12 shows, smaller $k$'s have longer correlation times. In the diffusion (large-scale) regime, this is consistent with the fact that the term $1/\tau_c$, appearing at the denominator of the diffusion coefficient expression in Eq. 2.39, can be neglected. The sweeping therefore becomes a correction, producing very small differences, as shown by the two theoretical curves in Fig. 2.11 and confirming that diffusion is effectively modulated by large-scale structures.

## 2.7 Particle Acceleration

In the previous Sections, in agreement with existing literature (Jokipii & Parker, 1969; Matthaeus et al., 2003), we have shown that diffusivity depends on particles' energy, and can be well described by the 2D-NLGC theory. In this Section, we investigate the possible mechanisms responsible for the acceleration and energization of charged particles in plasma turbulence.

Again, we start from a statistical description of our ensemble of $10^5$ particles. We computed the distribution of the Lagrangian acceleration, $\boldsymbol{a} = \partial \boldsymbol{v}/\partial t$ (evaluated using a $6^{th}$ order finite difference centered method), of all particles at different times for all HPIC simulations. The initial condition for Lagrangian quantities is to be normally distributed. Therefore, we can take advantage of the $\chi^2$ distribution that is defined as

$$PDF(\chi^2_k) = \frac{1}{2^k \Gamma(k/2)} x^{k/2-1} e^{-x/2}$$

where $\Gamma(x)$ is the gamma function, and $k$, commonly referred to as "degrees of freedom", represents the number of elements of a set of independent normally distributed variables $\{x_1, x_2, \ldots, x_k\}$ . The sum of the squares of these $k$ variables distributes according to the $\chi^2_k$ PDF. In our case, the three independent variables are the acceleration components $\{a_x, a_y, a_z\}$, and the square modulus of the acceleration $|a|^2 = a_x^2 + a_y^2 + a_z^2$ distributes according to $PDF(\chi^2_3)$ with 3 degrees of freedom. The distributions of $|a|^2$ perfectly overlap with PDF($\chi^2_3$) at initial times, as reported in Fig. 2.13, confirming that acceleration is a normally distributed variable. The time evolution for low- and high-$\beta$ plasmas is different. The latter shows no appreciable sign of time evolution during the simulation; the initial and final distributions are indistinguishable. The former, instead, develops a well-noticeable tail that grows in time, separating from the initial distribution. This means that the number of particles experiencing "anomalous" acceleration is larger for the low-$\beta$ plasma, suggesting that a physical process that depends on plasma conditions is at work (Chandran & Maron, 2004).

A straightforward acceleration mechanism can be due to an electric field parallel to the local magnetic field, namely $E_\parallel = \frac{\mathbf{E}\cdot\mathbf{B}}{|\mathbf{B}|}$ (as we have also seen in the simple model of Sec. 2.1). We define "anomalous" particles as those with acceleration values exceeding the variance of their distribution (see below). Such particles are correlated with $E_\parallel$ and magnetic structures as Fig. 2.14 shows. Anomalous

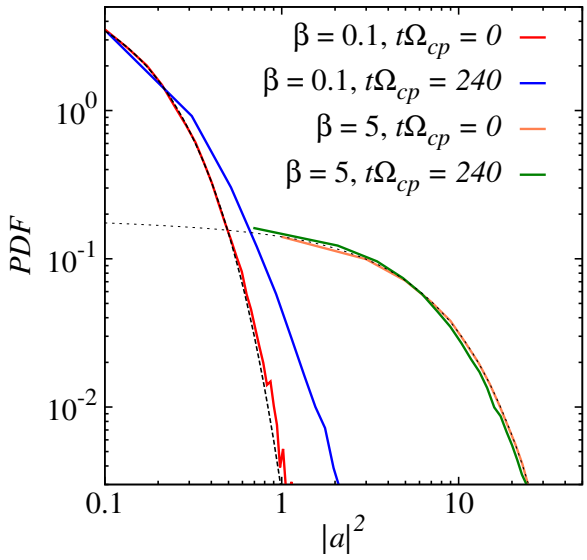


Figure 2.13: PDFs of the acceleration, for $\beta = 0.1$ and $\beta = 5$. Both initial and final times of the simulations are reported, together with the corresponding probability distributions (dashed black lines). In the low$\beta$ plasma, "anomalous" acceleration processes are observed.

particles are, indeed, non-uniformly distributed on the color map of $E_{\parallel}$. They tend to cluster within magnetic islands, evidenced by the contour plot of the magnetic potential $a_z$, at whose boundaries it is known that reconnection electric field is large and strong magnetic discontinuities are present (Ambrosiano et al., 1988; J. Tessein et al., 2013).

To establish a more quantitative link between the electric field and possible local acceleration effects, we compared the PDFs of separate contributions to the electric field (see Eq. 1.21). We focus on those terms that can be parallel to the local magnetic field ($\nabla P_e$ and $\eta \boldsymbol{j}$), on the total parallel electric field itself ($E_{\parallel}$), and the total inductive electric field ($E_{ind} = |\boldsymbol{u} \times \boldsymbol{B}|$). To make an association with particles' acceleration, we divide them into low- and high-acceleration populations. The two populations were distinguished by thresholds with respect to the global acceleration distribution: the high-acceleration population is defined by acceleration values larger than three standard deviations of the global distribution ("anomalous"), the other population has acceleration values lower than one standard deviation ("normal"). We build up the distributions of the above-mentioned fields at particles position indicating with superscript "$^{\uparrow}$" those measured at the positions of "anomalous" ions, whereas the fields with superscript "$^{\downarrow}$" are related to "normal" particles. Note that the above conditioned statistics would give the

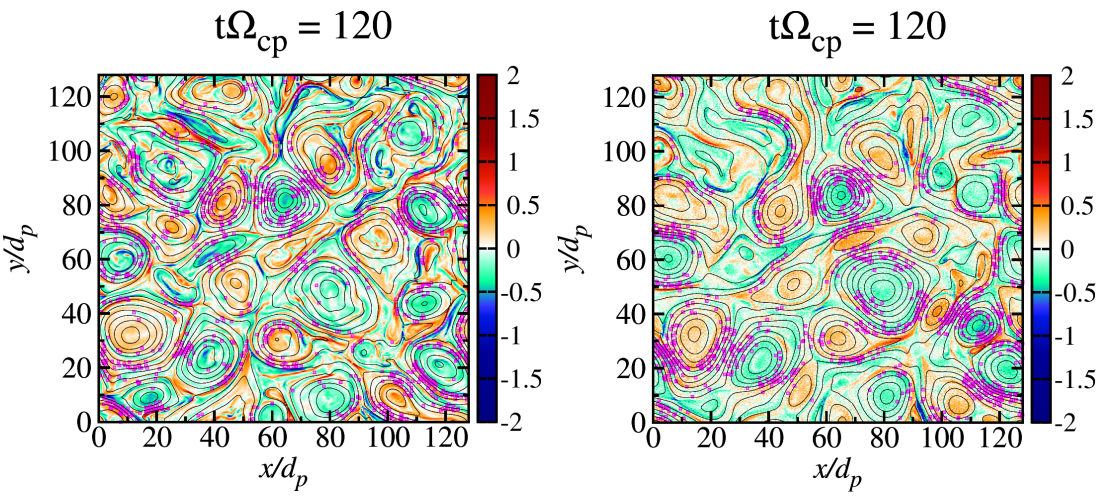


Figure 2.14: Particles with very high acceleration (magenta squares), superimposed on the shaded contour of the parallel electric field in (left) low- and (right) high-$\beta$ plasmas. These particles are localized at the boundaries of magnetic structures (evidenced by the contour plot of magnetic potential $a_z$) where $E_{\parallel}$ is large.

same distribution only if acceleration and fields are uncorrelated.

The localization of anomalous particles on the flanks of magnetic islands suggests that, along with the parallel electric field, magnetic field discontinuities can also play a role in the acceleration process. To reveal the presence of small-scale gradients of the magnetic fields, we use the PVI technique (Greco et al., 2008; Greco, Matthaeus, Servidio, Chuychai, & Dmitruk, 2009; Greco et al., 2018).

Generally, the detection of discontinuities can be achieved via several methodologies such as those based on wavelets (Farge, 1992; Farge & Schneider, 2015) as the local intermittency measure (LIM) (Bruno et al., 2001), or distinct techniques such as the phase coherence index (Hada et al., 2003), and multifractal analysis (Sorriso-Valvo et al., 2017). Among these, we chose the PVI (that is a particular case of wavelet transform) for its utility, ease of implementation, and good time localization despite the scarce scale localization. This technique has few-to-no assumptions on the discontinuity type it can detect, and has been extensively tested in simulations (Greco et al., 2018), and has been demonstrated to give similar results as LIM analysis (Greco & Perri, 2014).

These regions of discontinuities are indeed usually found at the boundaries of magnetic islands where, possibly, reconnection, heating, and particle acceleration are taking place (J. Tessein et al., 2013; Osman et al., 2014; Khabarova et al., 2016; Pecora et al., 2018). The PVI is defined as

$$\mathrm{PVI}(s,\ell) = \frac{|\Delta \boldsymbol{B}(s,\ell)|}{\sqrt{\langle |\Delta \boldsymbol{B}(s,\ell)|^2 \rangle}}, \tag{2.41}$$

where $\Delta \boldsymbol{B}(s,\ell) = \boldsymbol{B}(s+\ell) - \boldsymbol{B}(s)$ are the increments evaluated at scale $\ell$ and the averaging operation $\langle \dots \rangle$ is performed over a suitable interval (Servidio, Greco, et al., 2011). The function can be computed spatially in simulations or in magnetic field time series by assuming the Taylor hypothesis. The structures identified by large PVI values contribute to non-Gaussian statistics and therefore to intermittency (Matthaeus et al., 2015; Bruno, 2019). Applying the PVI technique, we found that the regions of larger $E_{||}$ occur in correspondence of magnetic discontinuities and not in smooth regions, as the PDF of $E_{||}$ conditioned on PVI values clearly evidences in the inset of panel (a) of Fig. 2.15 (Greco, Matthaeus, Servidio, & Dmitruk, 2009). In the Figure, we see that the distribution of each electric field contribution is enhanced at the positions of highly accelerated particles, indicating that anomalous particles are more likely to be associated with larger electric field values. This supports the idea that accelerating particles cluster close to regions where dynamical activity is occurring, notably along boundaries of interacting flux tubes, and near the associated current sheets, suggesting involvement of magnetic reconnection. In general, the conditioned PDFs of Fig. 2.15 further confirm the relation between the parallel electric field and the stochastic acceleration mechanisms in 2.5D turbulence.

This acceleration in the out-of-plane direction has a global effect of elongating the ion velocity distribution function (VDF) in this same direction. To see if this typical alignment effect is present in our numerical experiments, we computed the PDFs of the angles that particles' velocity forms with both the local and mean magnetic fields (along $z$) as:

$$\cos(\theta) = \frac{\boldsymbol{v}\cdot\boldsymbol{B}}{|\boldsymbol{v}||\boldsymbol{B}|}, \qquad \cos(\psi) = \frac{v_z}{|\mathbf{v}|} \tag{2.42}$$

In Fig. 2.16 we report the distributions of the cosine of both these angles, at the initial and final times of the simulation, for different values of $\beta$. At the initial time, when turbulence has not developed yet, the distributions are quite flat, as evidence of the initially isotropic particle distribution. As turbulence develops, particles tend to align with the mean magnetic field in the $z$ direction. This effect is much more evident for the low-$\beta$ plasma, the more magnetized one. Another feature one can notice in the low-$\beta$ plasma is that particles orient themselves more

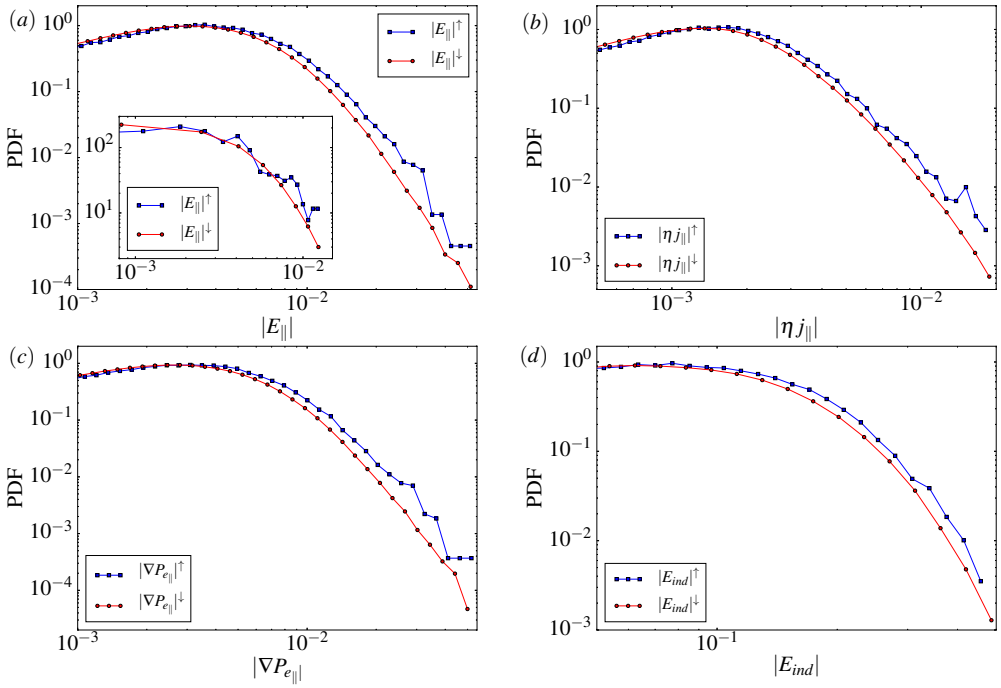


Figure 2.15: PDFs of electric field terms (see Eq. 1.21) conditioned to particles' acceleration. PDFs designated by $^\uparrow$ (blue squares) are the PDFs collected at positions of anomalous particles, defined as particle with acceleration value exceeding three standard deviations of the total acceleration distribution. Likewise, PDFs for normal particles, indicated by $^\downarrow$, (red circles) are collected at the positions of particles with acceleration below one standard deviation. The cases shown are (a) total parallel electric field $|E_\parallel|$; (b) parallel resistive electric field $|\eta j_\parallel|$; (c) parallel electron pressure $|\nabla P_{e\parallel}|$; and (d) total inductive electric field $E_{ind} = |\boldsymbol{u} \times \boldsymbol{B}|$. The parallel components are defined relative to the local magnetic field vector. The inset of panel (a) shows the total parallel electric field component conditioned over PVI values. Red circles are the parallel electric field values computed along the whole PVI path, whereas blue squares are the parallel electric field values computed in the regions where the PVI exceeds a threshold value. From Pecora et al. (2018).

on the local magnetic field rather than its $z$ component ($\cos(\theta)$ distribution has slightly larger values than that of $\cos(\psi)$), although the $z$ component is its main one and the difference is not statistically relevant.

It is crucial to see now whether this acceleration mechanism, locally related to intense parallel electric fields, can actually increase particles' energy. This correspondence is not trivial since particles with anomalous acceleration are only a small fraction of the plasma. The distribution of energy in time, shown in Fig. 2.17, exhibits a different behavior at different $\beta$'s. In low-$\beta$ plasma, the

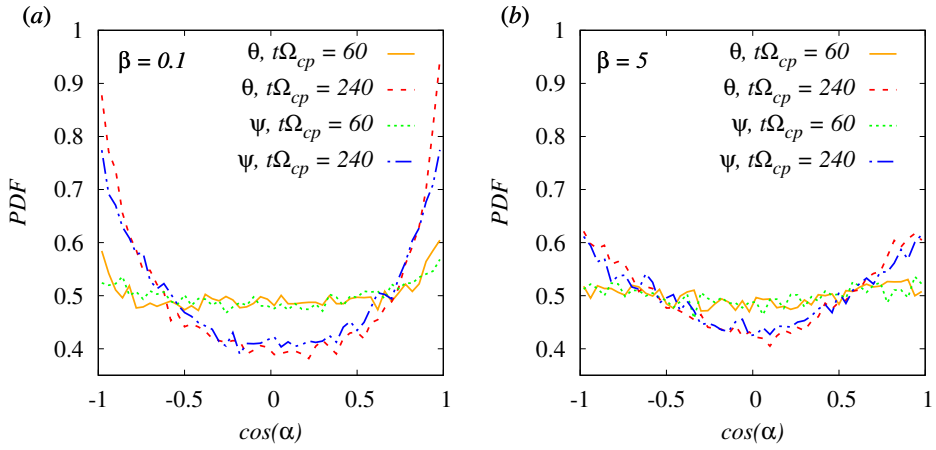


Figure 2.16: PDFs of the cosine of the angle between particles' velocity and the magnetic field for (a) low- and (b) high-$\beta$ plasmas, before maximum turbulence activity and at the end of the simulation. Both plasma $\beta$'s start with an isotropic distribution of the velocities (orange and green lines). At the end of the simulations, particles align to the magnetic field (red and blue lines). The effect is more evident for more magnetized particles (low-$\beta$), and less pronounced for less magnetized particles (high $\beta$).

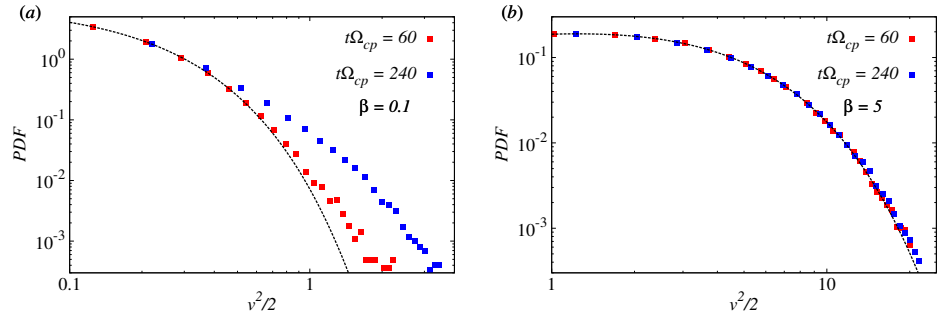


Figure 2.17: PDF of particles energy, for the (left) low- and (right) high-$\beta$ simulations, at different times of the simulation. Particles in low-$\beta$ plasma have a substantial energy gain because of resonance with turbulence small-scale structures. The distribution of particles in high-$\beta$ plasma does not experience any significant evolution.

PDF develops a power-law tail, consistent with previous findings in literature (Guo et al., 2016). On the other hand, high-$\beta$ plasma is less prone to developing high-energy tails, and the distribution at later times is rather indistinguishable from that of the initial, Maxwellian equilibrium condition. This suggests that the acceleration mechanisms can energize particles and that the process depends on the plasma $\beta$.

### 2.7.1 Magnetic trapping

We have seen that the acceleration mechanism involves the parallel electric field. However, there must be something else that makes this field preferably energize particles in low- rather than in high-$\beta$ plasmas. In Fig. 2.14 it is shown that anomalous particles lie within magnetic islands, in agreement with previous discussions. The acceleration mechanism possibly occurs in association with magnetic reconnection. Particles temporarily trapped inside small flux tubes or in the dynamically active region of larger flux tubes experience coherent acceleration processes. In the region near current sheets, particles can experience almost continuous energization (Ambrosiano et al., 1988; Hoshino et al., 2001; Drake et al., 2010; Haynes et al., 2014). Moving from a statistical description to single-case observation, we followed the trajectory of one of the most energetic particles and monitored its energy, acceleration, and the parallel current density it experiences along its journey (the parallel pressure term is not shown because it is too noisy for non-statistical treatment). This particle and the above-mentioned quantities are shown in Fig. 2.18. The trajectory is plotted over the color map of $E_{\parallel}$ with contour plot of the magnetic potential. Fields evolution is slower than particle motion so that large-scale structures can be considered quasi-stationary during this time interval. This individual trajectory confirms the discussion carried on in previous Sections: particles can be confined within magnetic islands and be effectively energized interacting with a coherent electric field, as the color code of the trajectory – indicating the energy of the particle – suggests. Eventually, the energy grows up to a value that allows the particle to escape the magnetic confinement.

Analogously to Fig. 2.18, Fig. 2.19 shows a proton, in FPIC simulations, interacting with a strong current sheet. The particle gets energized passing through this intermittent structure, as the increase of its orbit radius suggests.

To estimate global escaping times we calculated the Lagrangian auto-correlation time using Eq. 2.31 (reported here for convenience),

$$T_{esc} = \frac{1}{\langle v_x(t_0)^2 \rangle} \int_0^\infty \langle v_x(t_0) v_x(t_0 + \tau) \rangle d\tau.$$

This quantity roughly represents the time interval up to which a particle experiences a correlated field. In the above definition, the averaging operation $\langle \dots \rangle$ is performed over a suitable ensemble of particles. We first averaged over all particles

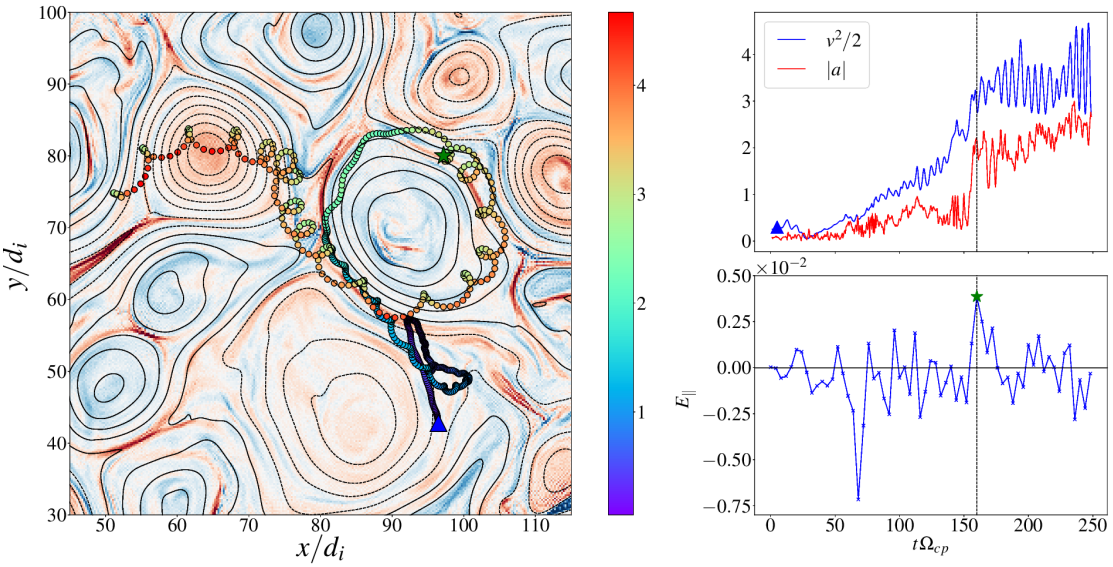


Figure 2.18: One of the most energetic particles, in HPIC simulations, followed along its path. (Left) Particle trajectory, starting at the blue triangle, superimposed on the map of $E_\parallel$ (color shading), and magnetic potential $a_z$ (contour lines) that evidences magnetic structures. The map of $E_\parallel$ is a snapshot at $t\Omega_{ci} = 160$, when the particle encounters the peak of $E_\parallel$ (indicated with the green star). The color code of the trajectory measures the kinetic energy that grows while the particle is trapped in a magnetic island. (Top right) Particle energy (blue line), and acceleration (red line). (Bottom right) Lagrangian $E_\parallel$ – measured along the particle's trajectory. Both the energy and the acceleration show an increase in correspondence to a peak in the parallel current density. After the boost in acceleration and energy, these quantities, although oscillating, remain almost constant.

| $\beta$ | $T_{esc}^{all}(\Omega_{ci}^{-1})$ | $T_{esc}^{anom}(\Omega_{ci}^{-1})$ |
|---|---|---|
| 0.1 | 9.6 | 5.7 |
| 0.5 | 4.1 | 3.0 |
| 5 | 0.9 | 0.8 |

Table 2.4: Correlation times of all particles ($T_{esc}^{all}$) and of anomalous particles ($T_{esc}^{anom}$) for the three $\beta$ values of HPIC simulations.

and then compared the values with the average performed only over anomalous particles. Numerical values are reported in Table 2.4.

For the isotropy of the perpendicular plane, we computed the escaping times also using $v_y$ correlation function obtaining similar results. The determined escaping times are consistent with the fact that particles in low-$\beta$ plasmas develop high energy tails since they are confined within magnetic islands for longer periods, experiencing a coherent acceleration from the parallel electric field. On the

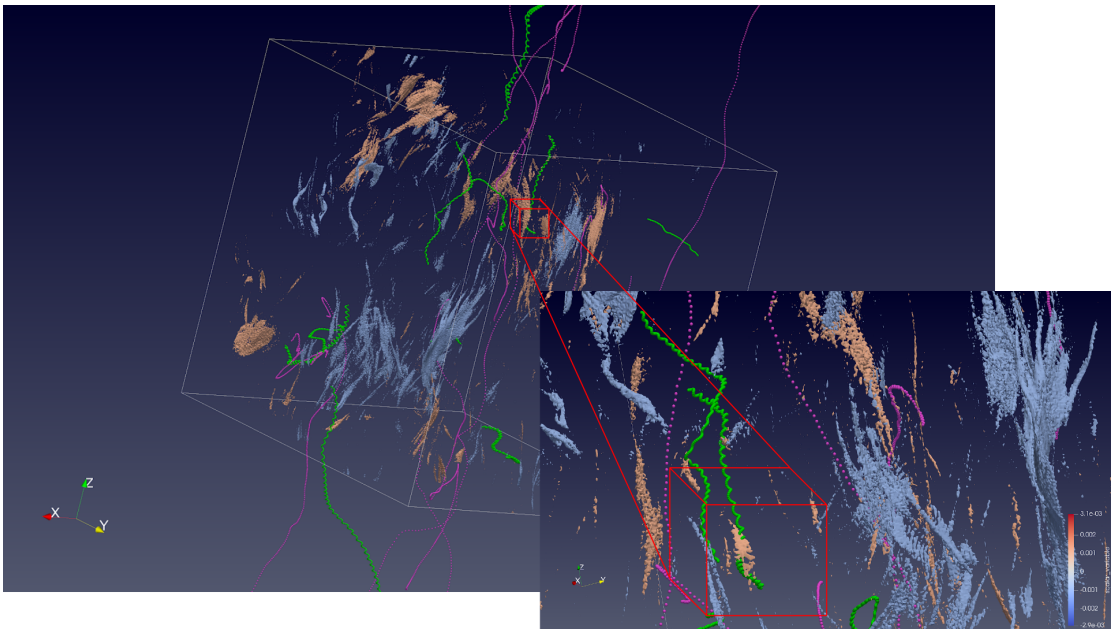

Figure 2.19: Interaction of a proton with a current sheet in FPIC simulations. The $x-y$ plane is the simulation domain, the $z$ axis represents the time. Strong current sheets are indicated with iso-surfaces (red for positive, and blue for negative $j_z$). Trajectories of some ions (green) and electrons (magenta) are shown. In particular, the blow-up shows a proton passing through an intense current sheets and becomes energized (notice the increase in the orbit radius and in the velocity component parallel to the mean magnetic field in the $z$ direction).

other hand, particles in high-$\beta$ plasmas easily escape from magnetic islands and are not efficiently energized since they are subject to stochastic values of $E_{\parallel}$ which are less prone to provide coherent acceleration. The comparison of trapping times values at the same $\beta$ for the different populations supports this view. Indeed, the escaping times calculated over all the particles are longer than those of the anomalous particles suggesting that more energetic particles are more likely to escape from magnetic islands while lower-energy particles remain trapped for longer periods and experience coherent energization. This coherent acceleration process due to stochastic reconnection electric field, invoked in small scale reconnection (Ambrosiano et al., 1988), is now quantitatively observed in large scale plasma turbulence. It is interesting now to further characterize the energization process by looking at the characteristic parameters of these anomalous particles.

### 2.7.2 Magnetic moment (non) conservation

We now further inspect the acceleration process by looking at the magnetic moment $\mu$, defined as

$$\mu = \frac{mv_\perp^2}{2B}, \tag{2.43}$$

where $m$ is the particle mass and $v_\perp$ its velocity (perpendicular to the magnetic field $\boldsymbol{B}$ measured at the particle's position). If $\boldsymbol{B}$ is slowly varying, particles' orbits are like closed circles and the flux of magnetic field passing through them is almost constant, namely:

$$\Phi_B = \Sigma B = \pi R_L^2 B = \pi \left(\frac{mv_\perp}{qB}\right)^2 B = \frac{\pi m^2}{q^2}\frac{v_\perp^2}{B} \doteq \frac{2\pi m}{q^2}\mu,$$

where $\Sigma$ is the surface enclosed within the circular orbit and $R_L$ is the radius of the orbit. This flux is constant if the ratio $v_\perp^2/B = 2\mu$ is constant. This suggests that the magnetic moment might not be a constant of the motion in a turbulent system where magnetic field changes are not negligible nor adiabatic (Dalena et al., 2012). This phenomenon however depends on the characteristic scales, as we will see in a little. A first visual inspection of magnetic moment variations can be obtained evaluating a normalized version for each particle $p$:

$$\tilde{\mu}_p = \frac{\mu_p(t) - \mu_p(0)}{\mu_p(0)}. \tag{2.44}$$

This measure gives information about the variation of the particle magnetic moment with respect to its initial value. Figure. 2.20 shows $\tilde{\mu}_p$ as a function of time, for some randomly selected particles, for two values of plasma $\beta$. Particles that move in the low-$\beta$ plasma have the highest magnetic moment excursions; in the high-$\beta$ plasma, where particles are not so energized in time, the magnetic moment is much more conserved.

To see whether the magnetic moment is a constant of the motion in a more quantitative way, we calculated the standard deviation $\sigma_\mu(p)$. This can be interpreted as the dispersion of the magnetic moment, for each particle, and is defined as

$$\sigma_\mu(p) = \sqrt{\frac{1}{T}\int_{t_0}^{t_0+T} \left(\mu_p(t') - \langle\mu_p\rangle_T\right)^2 dt'}, \tag{2.45}$$

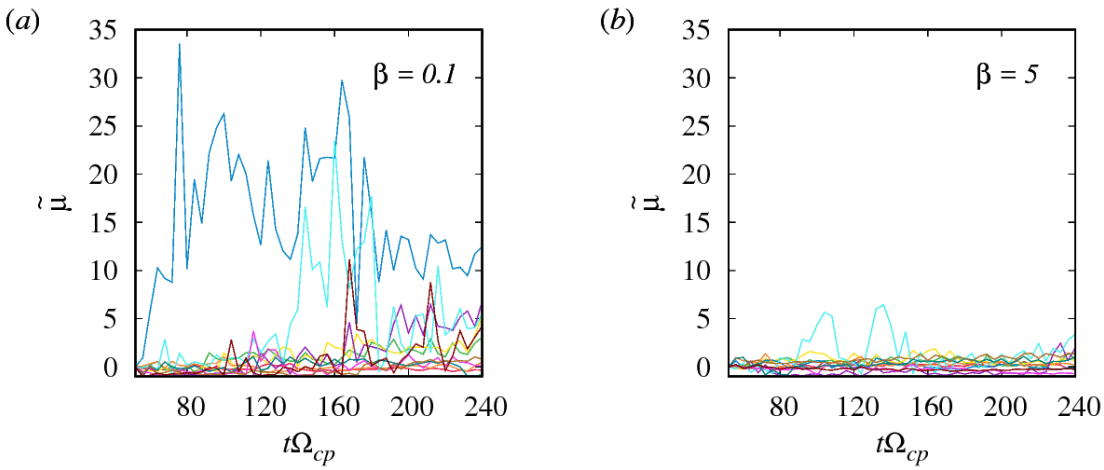


Figure 2.20: Normalized magnetic moment as a function of time, for a group of 11 randomly selected particles, for (a) $\beta = 0.1$, and (b) $\beta = 5$. The violation of magnetic moment conservation is much more pronounced in the case of $\beta = 0.1$. In the low-$\beta$ plasma, particles have smaller gyro-radii and they can interact with local strong inhomogeneities. On the other hand, in the high-$\beta$ plasma particles keep their magnetic moment better conserved as small-scale local sharp variations are averaged out over large orbits.

where $\mu_p(t)$ is the magnetic moment of the $p$-th particle at the time $t$, and the average in the integral is calculated over an appropriately long time interval $T$. In the case of perfectly conserved magnetic moment, this quantity is null. To better visualize the dispersion of the magnetic moment, we built the PDF of the quantity

$$\varepsilon = \frac{\sigma_\mu(p)}{\langle \mu_p \rangle_T}, \tag{2.46}$$

that indicates how much the magnetic moment deviates from its mean value – how much the magnetic moment is "broken". The PDF($\varepsilon$) is shown in panel (a) of Fig. 2.21, for the whole ensemble of $10^5$ particles. The violation of the magnetic moment is much more pronounced in the case of $\beta = 0.1$, for which the distribution is broader. Low-$\beta$ particles have small gyro-radii and they can actively interact with local sharp inhomogeneities, while high-$\beta$ particles keep their magnetic moment better conserved as they average out small-scale intermittent events.

For a direct comparison of magnetic moment violation with small-scale structures, we inspect both Lagrangian and Eulerian quantities. About the former, the

typical size is that of the Larmor radius, whose distribution is shown in panel (b) of Fig. 2.21, and reveals what is expected: low-$\beta$ particles have a narrow distribution about small values; large-$\beta$ particles, instead, have a broader distribution centered about larger values. In the same panel, we also report the Taylor length defined as $\lambda_T = \sqrt{\frac{\delta b_\perp^2}{\langle j_z^2 \rangle}}$, and the average current sheets' width $\delta_c$. The former is the scale at which the resistive term is no longer negligible, and it is about the size of the largest current sheet in the simulation; the latter is the average thickness of current sheets cores – where the current density is more intense. In our simulations. $\lambda_T \sim 1.7 d_i$ and $\delta_c \sim 0.3 d_i$. The positioning of these two important scales supports the description of the dynamics given before. The emerging picture is that of a scale resonance between particles and turbulence. When the orbit is much larger than the average current sheets' size $\delta_c$, and of the order of the dissipative scale $\lambda_T$, particles cannot resonate with and gain energy from turbulence small-scale structures. On the other hand, particles with orbits of the order of $\delta_c$ "feel" the presence of sharp discontinuities and experience magnetic moment non-conservation and coherent energization.

The obvious limits in drawing these conclusions are the physical size and the spatial resolution of the simulation domain. The $\beta$-dependence of magnetic moment conservation may not be so distinct in domains where coherent structures (e.g. current sheets) can develop on a wider range of scale and provide coherent interaction with particles of lower and higher energies. A saturation of such interaction, possibly due to approaching the dissipative scale or reaching energies high enough to include energy losses caused by radiative processes, is out of the scope of the present description.

### 2.7.3 Approaching velocity space diffusion

In Sec. 2.2, we investigated spatial diffusion. Then, we concentrated on the possibility of particles to modify their velocity (to accelerate). Acceleration can be interpreted as "motion" in velocity space, i.e. $v$-diffusion (Subedi et al., 2017). In this last Section, we will briefly mention this aspect. As for spatial diffusion, it is instructive to observe particles trajectories in the velocity space. In particular, we represent these trajectories in a 2D space whose coordinates are $v_z$ (parallel to the global magnetic field) and the in-plane velocity $(v_x^2 + v_y^2)^{1/2}$. The trajectories in this subset of the velocity space are shown in Fig. 2.22.

Velocity space trajectories show, from another point of view, the same behavior

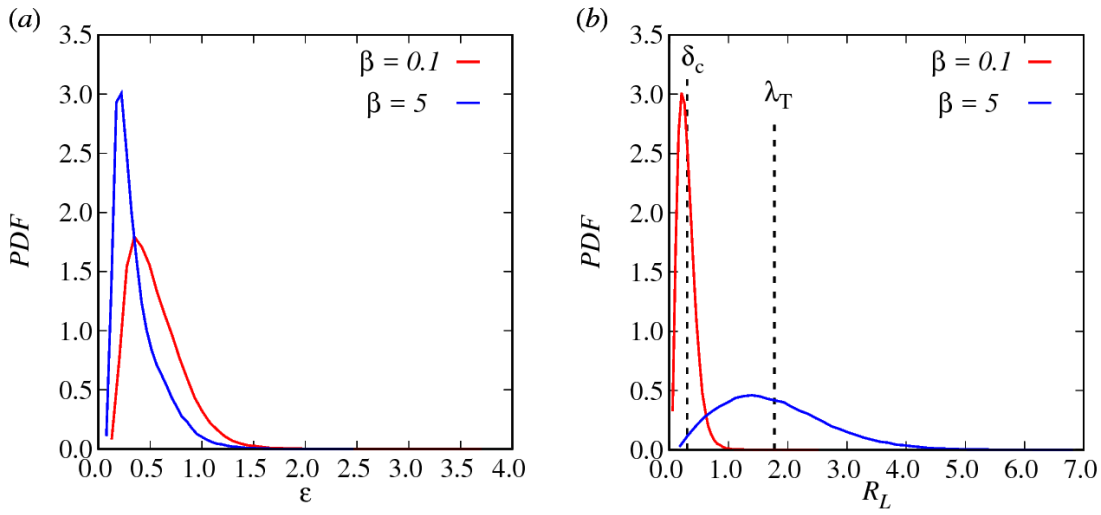


Figure 2.21: (a) PDF of the dispersion of the magnetic moment defined in Eq. 2.46. These PDFs show that particles are more likely to "break" their magnetic moment in the low-$\beta$ case. (b) PDF of the Larmor radius for different $\beta$'s. High-$\beta$ particles have a wide distribution, reaching values up to one order of magnitude larger than in the low-$\beta$ case. The Taylor length $\lambda_T$ and the average current sheets width $\delta_c$ are also indicated.

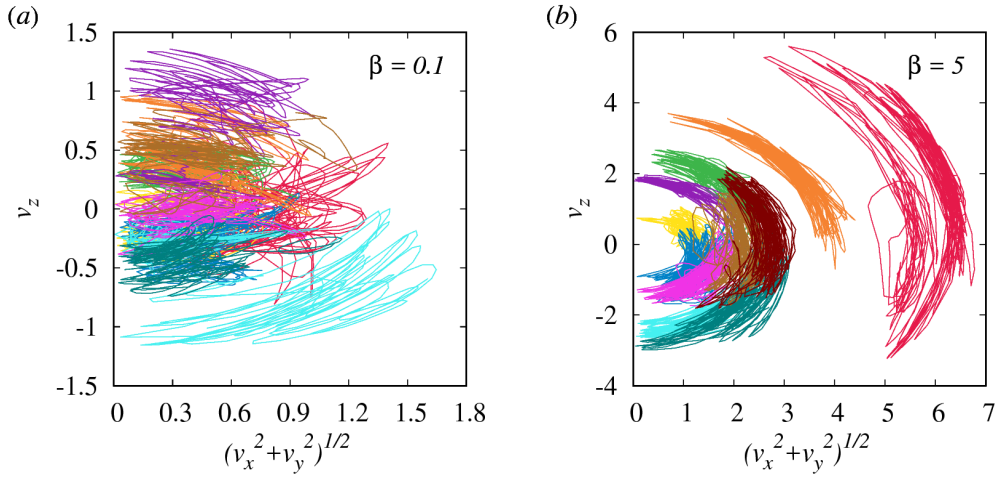


Figure 2.22: Velocity space trajectories for the same particles of Fig. 2.20, at (a) low, and (b) high $\beta$'s. Particles moving in the high-$\beta$ plasma are more energetic and do not undergo energization processes. They diffuse in pitch angle and move on quasi-isoenergetic shells. Differently, in the low-$\beta$ plasma, particles manifest more complex (almost ergodic) trajectories: they are not locked on isoenergetic shells since they can effectively gain/lose energy throughout their turbulent journey.

we have seen in the previous Sections. In the high-$\beta$ plasma, particles can be slightly accelerated but not effectively energized. Indeed, they diffuse only in pitch-angle and gyrophase moving on isoenergetic shells varying only the angle the velocity forms with the magnetic field. In the low-$\beta$ plasma, particles are coherently accelerated and decelerated by current sheets and magnetic structures (recall, however, that the percentage of high-energy particles is very low). The combined acceleration, deceleration, and energization phenomena make particles trajectories in the velocity space more complex, almost ergodic, since particles can diffuse both in pitch-angle and momentum-amplitude. The ergodicity domain is bounded by the upper limit of energy a particle can gain before escaping a vortex and run into a decelerating (de-energizing) electric field. This interesting aspect of velocity diffusion will be further inspected in future works.

## 2.8 HPIC & FPIC: similarities and differences

In this Section, we present a comparison between Hybrid- (Sec. 1.2.1) and Full-PIC (Sec. 1.2.2) simulations. We recall that the former (HPIC) can describe the kinetics only of the heavy species (protons) which is treated as Lagrangian particles while the electrons are described as a massless fluid. The latter (FPIC) solves Lagrangian equations for both the species composing the plasma. Small-scale phenomena, such as diffusion and acceleration, can be affected by the approximations that are used. In the following, we will highlight similarities and differences between the two approaches, conducting analyses similar to those of the previous Sections. It is important to recall that also inaccuracies may influence the results. For instance, an inadequate spatial resolution might affect energization phenomena as well as the diffusion of particles (Lapenta & Markidis, 2011).

### 2.8.1 Power spectra

Both the HPIC and FPIC simulations show important features in the power spectra of magnetic and electric fields, as shown in Fig. 2.23. The magnetic field spectrum manifests, for scales larger than the ion skin depth, an inertial range consistent with Kolmogorov's prediction of fluid-like turbulence, for which the power spectrum scales as $k^{-5/3}$ (where $k$ is the wavenumber). At smaller scales, the spectral slope is steeper, consistent with the index $-8/3$, typical manifestation

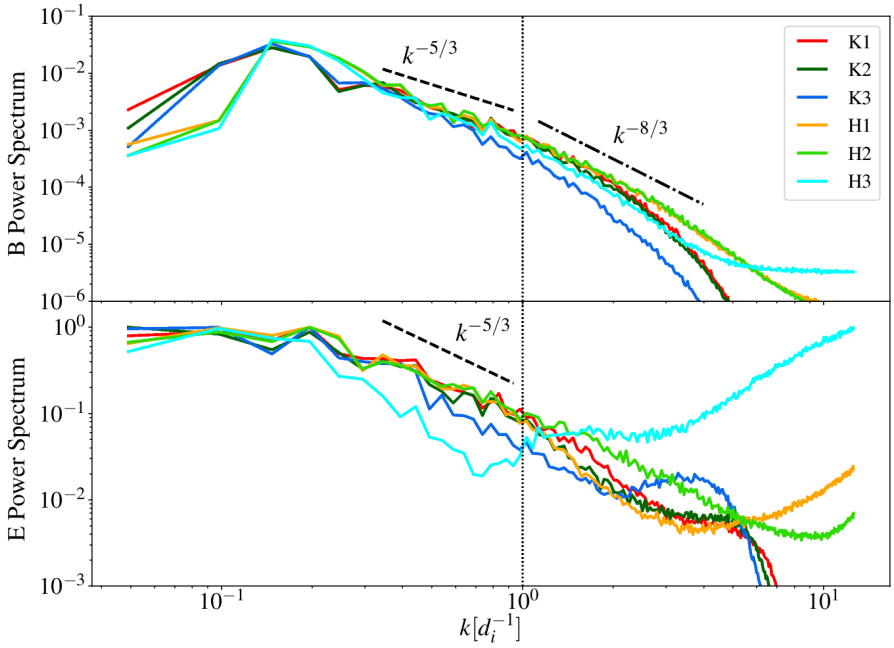


Figure 2.23: Comparison of the (top) magnetic and (bottom) electric field power spectra for the hybrid- (H1, H2, H3) and the full-PIC (K1, K2, K3) simulations. In both cases, the spectra present a range that follows Kolmogorov's prediction $k^{-5/3}$ (the so-called inertial range for $k$'s smaller than the ion skin depth) and the magnetic field spectrum approaches a $k^{-8/3}$ power law at smaller scales. The dashed and dot-dashed lines serve the purpose of guiding the eye. From Pecora, Pucci, et al. (2019).

of dispersive-kinetic physics (Alexandrova et al., 2009; Franci et al., 2015). Magnetic field spectra obtained from the two numerical experiments compare quite well in the inertial range, but there are some small differences at sub-ion scales. In particular, in the high-$\beta$ plasma, the magnetic field is steeper for the FPIC simulation. This may be due to electron physics, where electron resonances and damping might interact with small-scale magnetic fluctuations. Note also that for the hybrid case, at very small scales (almost the grid size), there is a flattening of the spectrum, due to particle noise which has not been treated with numerical filters (see below). This is indeed more evident for the high-$\beta$ simulation H3, at $kd_i \gtrsim 3$. The different behavior between the two codes at the very small scales is therefore due to the different ways of handling the noise. In the hybrid simulations, there is no artificial small-scale filter. In the FPIC algorithm, a local smoothing technique, described in previous literature (Olshevsky et al., 2018), has been introduced.

| run7 | | run8 (K3) | | run9 | |
|---|---|---|---|---|---|
| $v_z^2$ | $D$ | $v_z^2$ | $D$ | $v_z^2$ | $D$ |
| 0.6 | 2.0 | 0.7 | 2.1 | 0.6 | 2.1 |
| 1.9 | 4.0 | 2.0 | 4.3 | 1.8 | 4.0 |
| 3.1 | 5.4 | 3.3 | 6.0 | 3.1 | 5.3 |
| 4.3 | 6.3 | 4.6 | 7.1 | 4.3 | 6.5 |
| 5.6 | 7.1 | 5.9 | 7.7 | 5.5 | 7.3 |

Table 2.5: Particle energy values and the corresponding diffusion coefficient. The energy values do not change by increasing the number of particles from 400 to 4000 meaning that particles are accelerated and energized in the same way. Moreover, the diffusion coefficients are comparable among the runs suggesting that also spatial diffusion is not affected by an increase in the number of particles.

To better highlight small-scale differences between the hybrid and the full PIC approaches, we also computed the power spectrum of the electric field, also shown in Fig. 2.23. Qualitatively, these spectra are all in agreement with spacecraft observations (Bale et al., 2005), for which the slopes of the two fields are similar in the inertial range, whereas at sub-ion scales the electric field spectrum is higher than that of the magnetic field. There are some small differences between the two numerical methods, which are due to both physical and numerical reasons. Regarding the numerical reason, the noise has a role, in the hybrid case, at $kd_i \gtrsim 3$, as discussed before. The electric field is more sensitive to small-scale fluctuations and more directly to the noise of particles' momentum, since $\boldsymbol{E} \sim \boldsymbol{u} \times \boldsymbol{B}$. Therefore, the noise induced by low ppc is more evident in its spectrum. Regarding the physical reasons, at scales close to (and smaller than) the ion skin depth, it is interesting to notice that, for low $\beta$, there is more electric power in the FPIC case. This is very likely due to the fact that, generalizing Ohm's law, many contributions are missing in the hybrid approximation (such as the divergence of the whole electron pressure tensor contribution and other smaller electron inertial terms).

For the hybrid runs, Servidio et al. (2016) previously verified statistical convergence by varying the number of particles per cell. For the FPIC case, we did a convergence study for the high-$\beta$ case (that is the most sensitive to noise) in which we found that: (I) the power spectrum of the magnetic field is consistent going from 400 ppc to 4000 ppc (Fig. 2.24), and (II) the diffusion coefficient is consistent between these cases with different models and resolutions (Table. 2.5). The latter is not surprising, since the diffusion coefficient depends mostly on energy-containing and inertial scales of the magnetic spectrum ($kd_i \ll 1$)

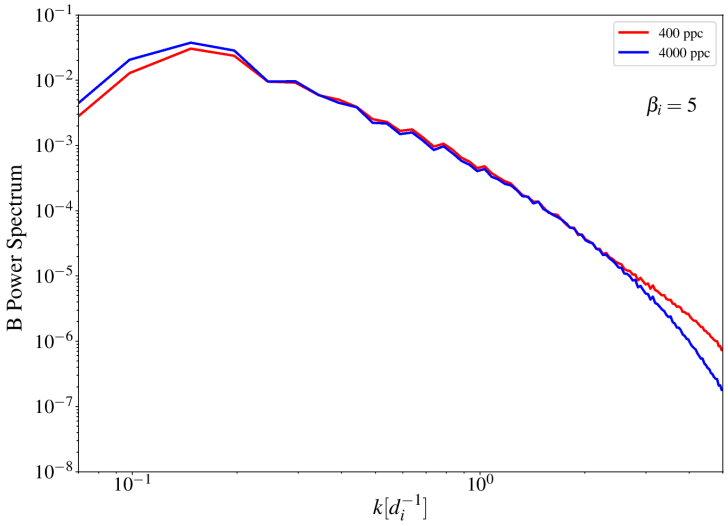


Figure 2.24: Magnetic field power spectra for FPIC run7 and run8 (K3) with 400 and 4000 particles per cell respectively. The spectra show the statistical converged achieved already at 400 ppc since the large scales are quite similar and the inertial ranges have the same slopes.

### 2.8.2 Ion diffusion

This Section is focused on the motion of the macro-particles. Again, to have a look at the collective general motion of the ions, we computed the mean squared displacement in the $xy$ plane, namely $\Delta s^2 = \Delta x^2 + \Delta y^2$, with $\Delta x$ and $\Delta y$ the displacements calculated after a time interval $\tau$ in the $x$ and $y$ directions respectively, defined as $\Delta x = x(t_0 + \tau) - x(t_0)$ and $\Delta y = y(t_0 + \tau) - y(t_0)$. For convenience, we recall Eq. 2.22 that links the mean squared displacement with the diffusion coefficient as

$$\langle \Delta s^2 \rangle = 2D\tau,$$

As reported in the previous Section, we divide particles in energy ranges and their mean squared displacements are shown in Fig. 2.25 for the two algorithms at different $\beta$'s (only a few energy classes are plotted for a matter of clarity).

In all cases, the linear trend expected for normal diffusion is achieved after long time intervals. The partitioning of particles in parallel energy ($v_z^2/2$) bins has been performed to control whether it influences perpendicular diffusion as predicted by the 2D-NLGC derived in Sec. 2.6. As expected from the theory, the diffusion coefficient is proportional to the energy of the particles in the parallel direction and to the presence of magnetic turbulence. We also computed the

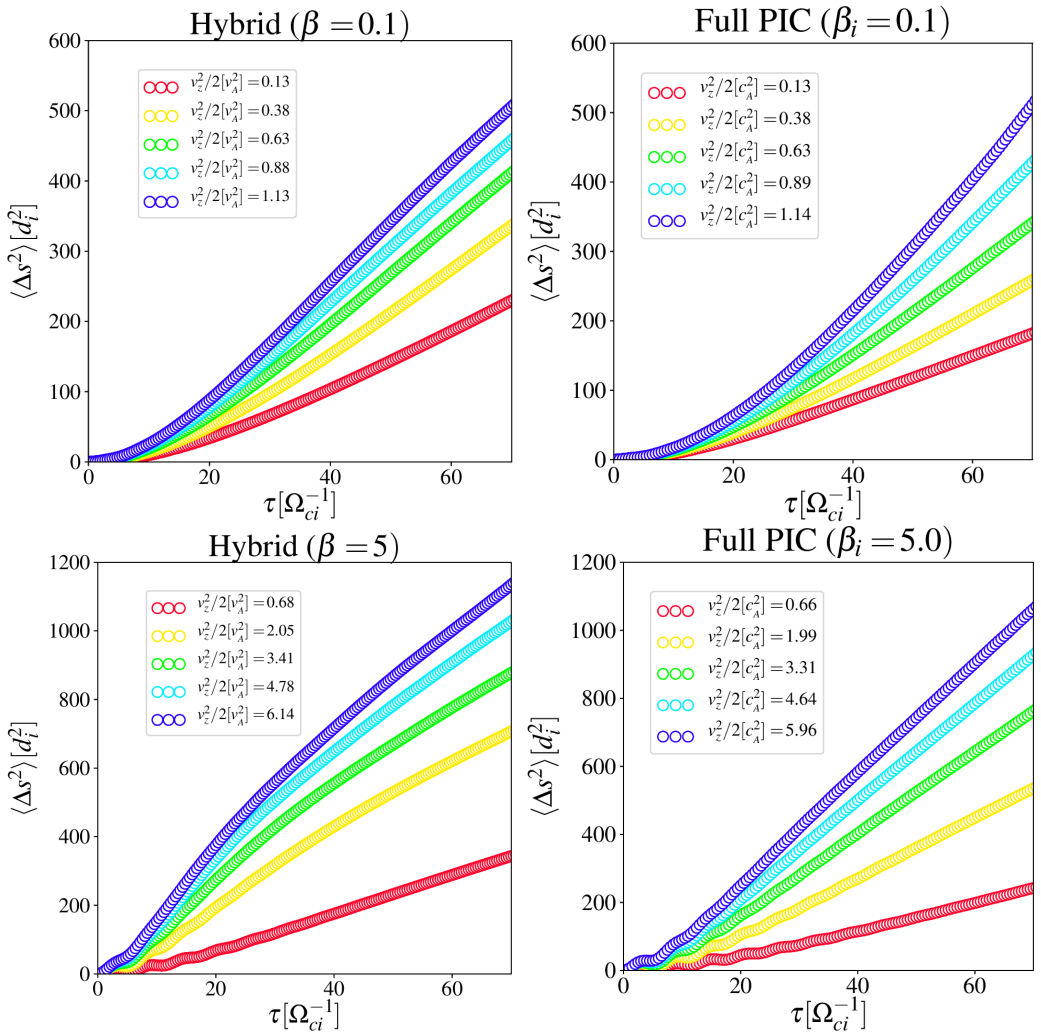


Figure 2.25: Ion mean squared displacement for the HPIC and FPIC simulations for the low- and high-$\beta$ plasmas. For each $\beta$, the particles class energy is reported in the label. From Pecora, Pucci, et al. (2019).

running diffusion coefficient for each energy class, for all simulations

$$D = \frac{1}{2}\frac{\partial \langle \Delta s^2 \rangle}{\partial \tau}. \tag{2.47}$$

The above quantity, computed over the appropriate ensembles of particles, achieves a plateau after the diffusive limit is reached. This classical procedure gives a measure of the diffusion coefficients for each class of parallel energy. The measured values are reported in Fig. 2.26, for $\beta = 0.1$ and 5, for both types of numerical experiments. A quite good agreement between both numerical approaches and the 2D-NLGC theory is found.

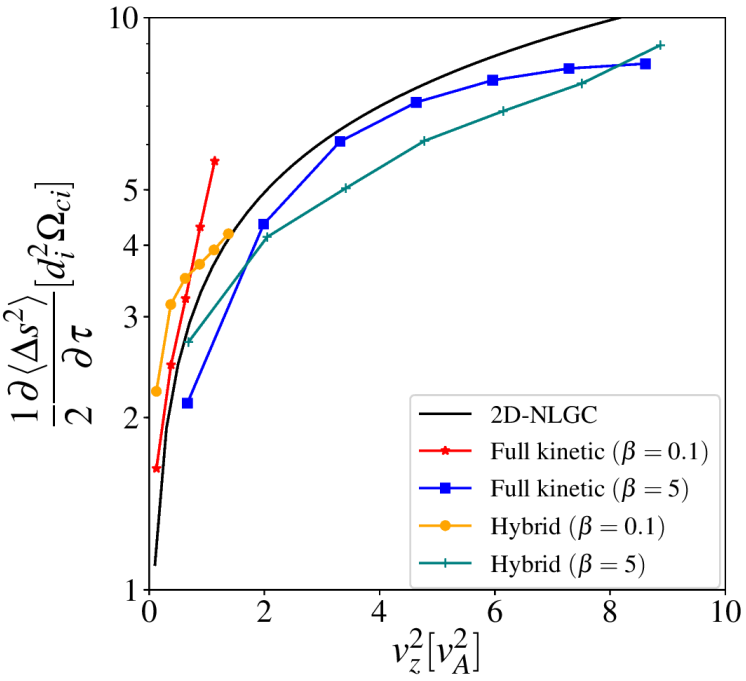


Figure 2.26: Perpendicular diffusion coefficient measured for the low- and high-$\beta$ plasma, for both HPIC and FPIC runs. The solid black line represents the theoretical prediction of 2D-NLGC. From (Pecora, Pucci, et al., 2019).

Though a slightly better agreement is evident in the case of FPIC simulations, the overall behavior is similar, suggesting that smaller-scale resolution is a higher-order correction for the problem of particle diffusion (as also evidenced by the convergence study).

### 2.8.3 Particle energization

The last process to compare is that of particle energization. It is important to establish whether there are substantial differences for particle energization mechanisms, comparing the HPIC and FPIC approaches. Figure 2.27 shows the distribution of the kinetic energy of particles $E_{kin} = (v_x^2 + v_y^2 + v_z^2)/2$ at the beginning of the turbulence steady state ($t\Omega_{ci} = 50$) and at the final time of the simulations ($t\Omega_{ci} = 200$).

PDF comparison suggests, as evidenced in the previous Section, that in the hybrid case, at high $\beta$, there is a very small deviation between the two times, indicating a lack of energization. This is because particles, in the case of large $\beta$ (and large Larmor radius), do not effectively gain energy by interacting with the

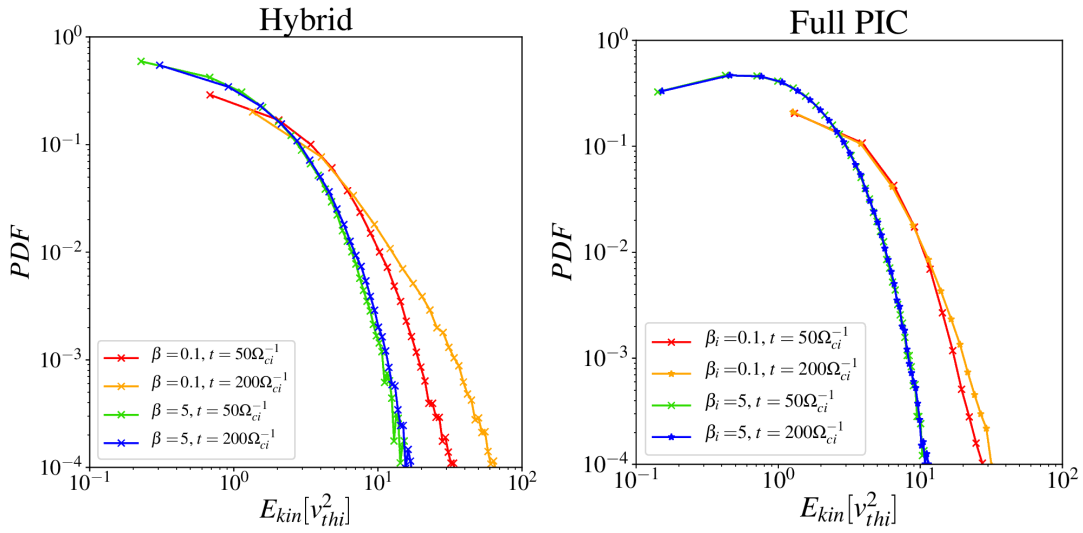


Figure 2.27: Particles kinetic energy evolution. The distributions of the energy (normalized to the ion thermal velocity $v_{thi}$) are shown for (left) HPIC and (right) FPIC simulation at two different times. In both cases, the energy in high-$\beta$ plasmas (green and) does not grow in time; for the low $\beta$ (red and orange), instead, HPIC ions gain much more energy with respect to those in FPIC simulations. From Pecora, Pucci, et al. (2019).

turbulence structures such as current sheets. This scenario changes when one looks at the low-$\beta$ case, where an extended tail develops at later times. This confirms the picture of small energy particles being able to actively interact with current sheets, because their scales are comparable, and be effectively energized (Chandran et al., 2010). This view is almost maintained in the full kinetic simulations, though some differences appear, and highlight the importance of describing both species (ions and electrons) when considering energization phenomena. In low-$\beta$ plasmas, the tail of energy distribution is less developed in the case of FPIC simulations indicating that, when electrons are also treated kinetically, the ions gain less energy from the turbulent fields. This suggests that, very likely, the electrons participate more effectively in this turbulence-particle interaction. Electrons may interact more synergistically with the structures generated by turbulence, such as current sheets and reconnection events (Drake et al., 2010; Haynes et al., 2014).

The comparison between two different numerical approaches carried out in this Section, sheds light on the consistency of our studies, especially concerning power spectra and particle diffusion dynamics. We found that a fully kinetic description of the plasma does not considerably affect diffusion properties. This was somewhat expected, as we have shown that diffusion is mostly influenced by

large-scale structures. Conversely, a noticeable difference came out when looking at particle energization. Possible competition mechanisms between species seem to arise in the presented FPIC simulations, even with an ion-to-electron mass ratio much smaller than the actual one. The fully kinetic description might open different channels for energy partitioning and therefore needs to be taken into consideration. In the next Section, we present full PIC 3D simulations and describe ongoing work on a self-consistent investigation of plasma turbulence.

## 2.9 Ongoing work: pair diffusion in 3D plasma turbulence

The 2D description given in the previous Sections, is extremely valuable since it provides realistic results, compatible with observations, with the advantage of a reduced computational cost for simulations, and reduced complexity for analytical treatment. Naturally, the 2D description carries along with some approximations that are not always appropriate for solar wind conditions. In this Section, we present a preliminary analysis of diffusion properties of particle pairs in 3D turbulence. In particular, we focus on the different diffusive properties in the case in which charged particles are moving in an anisotropic plasma (with a preferential direction along a mean field $B_0$). To investigate the properties of turbulence in the inertial range and for time intervals that are not asymptotic, we make use of particle pairs rather than single particles, as particle pairs provide an excellent tool for measurements of inertial range laws of turbulence (Boffetta & Celani, 2000; Boffetta & Sokolov, 2002; Biferale et al., 2005).

The goal is to link the Eulerian properties of fields to the Lagrangian properties of pairs. In the following Section, this intimate relationship will be derived.

### 2.9.1 Anisotropic Fokker-Planck equation

We concentrate on extending the Richardson law of turbulence (Richardson, 1926), that was developed for isotropic turbulence, to an anisotropic medium. We start from the idea that pair-particle motion is sensitive to inertial range fluctuations of turbulence when particle separation lies in this range as well, namely $d_i \ll r_{12} \ll \lambda_c$ – where $r_{12} = \sqrt{|x_1 - x_2|^2 + |y_1 - y_2|^2 + |z_1 - z_2|^2}$ is the separation between the two particles, of coordinates $\boldsymbol{r}_i = (x_i, y_i, z_i)$, composing the pair.

Following Richardson work, it is useful to define the quantity $P(r_{12}, t)$ which is the probability of having two particles, initially arbitrarily close, at a distance $r_{12}$ after a time $t$ (hereafter we will omit the subscript "12"). In the case of isotropic medium, $P(r, t)$ satisfies a Fokker-Planck equation written in spherical symmetry

$$\frac{\partial P(r,t)}{\partial t} = \frac{1}{r}\frac{\partial}{\partial r}\left[rD(r)\frac{\partial P(r,t)}{\partial r}\right] \tag{2.48}$$

with the diffusion coefficient of the form

$$D(r) \propto r^{2-\gamma}, \tag{2.49}$$

where $\gamma$ is the exponent of the turbulent field second-order structure function (Servidio et al., 2016). For anisotropic turbulence, one can expect $P(\boldsymbol{r}, t)$ to be anisotropic as well. Therefore, in analogy with the above definitions, we write a Fokker-Planck equation in the case of an anisotropic medium, in the absence of external forces, and independent directions, in the configuration space as

$$\frac{\partial P}{\partial t} = \sum_{i=1}^{3}\frac{\partial}{\partial x_i}\left\{D_{ii}\frac{\partial P}{\partial x_i}\right\}, \tag{2.50}$$

where $P$ is the probability density function and $D_{ii}$ is the diffusion coefficient along the $i$-th direction. As we learned in the previous Sections, the analytical form of the diffusion coefficient can vary and depends on the characteristics of the system in general. In our case, since we want to relate diffusion to anisotropic turbulence properties, we model the diffusion coefficient following the prescriptions of turbulence theory. As already mentioned, turbulence develops a power-law energy spectrum for the "cascading" fields, with a well-defined exponent in the so-called inertial range, say $E(k) \propto k^{-n}$. The second-order structure function is related to the exponent of the spectral power law as $S^2(\ell) \propto \ell^{n-1}$ when the increment $\ell$ falls in the inertial range, namely $\lambda_d \ll \ell \ll \lambda_c$, where $\lambda_d$ is the dissipative scale and $\lambda_c$ is the energy-containing scale (Frisch, 1995). By dimensional analysis, the diffusion coefficient can be written as $D \propto u\ell$ and $u$ can be related to spectral properties by the second-order structure function, for which $u^2 \propto \ell^{n-1}$, finally giving

$$D \propto \ell^{\frac{n+1}{2}} \tag{2.51}$$

where $\ell$, again, is the increment in a specific direction (Frisch, 1995). With

these prescriptions for the diffusion coefficient (Eq. 2.49 and Eq. 2.51), the link to Eulerian properties of the field in which particles move is immediate since $\gamma$ is the exponent of the second-order structure function, and $n$ is the scaling of the power spectrum. Moreover, Eq. 2.49 is consistent with the prediction of Eq. 2.51 as if we expect the Kolmogorov scaling, $2 - \gamma = 4/3$ and the obtained spectral index is $n = 5/3$.

Now we want to be more specific and apply these general statements to the case of turbulent anisotropic plasmas. As already shown before, when a mean field is present, turbulence has a preferential direction along the direction of the mean field (say $\hat{z}$), while the perpendicular plane can be considered isotropic. In this case, Eq. 2.50 can be written as (neglecting $y$-diffusion term without loss of generality)

$$\frac{\partial P}{\partial t} = \frac{\partial}{\partial x}\left\{ D_{xx}\frac{\partial P}{\partial x} \right\} + \frac{\partial}{\partial z}\left\{ D_{zz}\frac{\partial P}{\partial z} \right\}, \tag{2.52}$$

and the diffusion coefficients in the two directions can be written, using Eq. 2.51, as $D_{xx} = x^{\frac{n+1}{2}}$ and $D_{zz} = z^{\frac{m+1}{2}}$, where $n$ and $m$ are the slopes of the energy spectra in the $x$ and $z$ directions respectively. A solution to Eq. 2.52 is here found to be

$$P(x, z, t) = At^{-k} \exp\left(-\frac{x^{\alpha}}{\alpha^2 t}\right) \exp\left(-\frac{z^{\beta}}{\beta^2 t}\right) \tag{2.53}$$

with $\alpha = \frac{3-n}{2}$, $\beta = \frac{3-m}{2}$, and $k = \frac{\alpha+\beta}{\alpha\beta}$.

Again, as in Richardson (1926), $P(x, z, t)$ is the probability of having two particles with perpendicular separation $x$ and parallel separation $z$ (with respect to the mean field) after a time $t$. Now, we shall see if this relation can be qualitatively found in plasma turbulence simulations.

### 2.9.2 Lagrangian and Eulerian properties correlation

The above-mentioned analysis is carried out in novel simulations of 3D plasma turbulence that have been performed with the iPIC3D code described in Sec. 1.2.2. The box size is $40 \times 2\pi d_i$ in each direction, discretized with $512^3$ points. A mean magnetic field $B_0$ is present along the $z$ direction. To reduce the numerical noise of the PIC algorithm we use 401 particles per cell resulting in $55 \times 10^9$ total particles. We tracked and saved position and velocity information of about $130 \times 10^6$ to per-

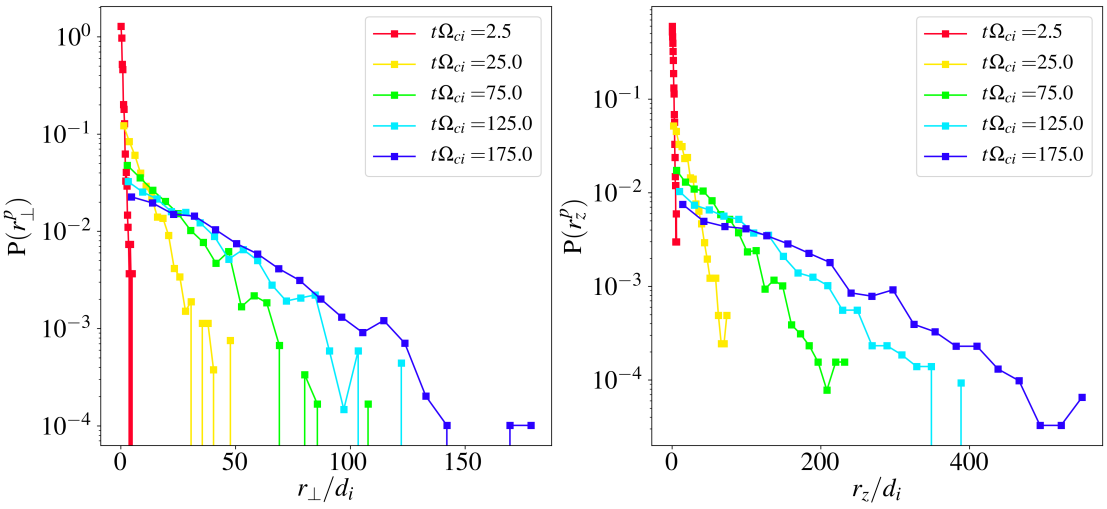


Figure 2.28: Time evolution of the (left) perpendicular and (right) parallel separation of proton pairs. The very narrow initial distribution develops non-Maxwellian tails, a symptom of extremely rapid diffusion processes.

form the following statistical analyses. Among these particles, we have identified as pairs those that have a separation $|r_{12}| = \sqrt{|x_1 - x_2|^2 + |y_1 - y_2|^2 + |z_1 - z_2|^2} = 0.1 d_i$ at the initial time set by the turbulence peak. Figure 2.28 shows the distribution of the separation of the above-determined pairs of particles. The initial distribution is extremely narrow, but it greatly grows in time also developing non-Maxwellian tails – a symptom of super-diffusive extreme events. The distributions are accumulated for proton separations (recall that iPIC3D is an FPIC algorithm, but electron analysis has still to be performed), in the perpendicular $r_\perp = \sqrt{|x_1 - x_2|^2 + |y_1 - y_2|^2}$ and parallel $r_z = |z_1 - z_2|$ directions. The possibility to incorporate $x$ and $y$ in a generic perpendicular separation comes from the isotropy of the perpendicular plane when a mean magnetic field is present.

In analogy with previous Sections, we measured the mean squared separation $\langle r^2 \rangle$, shown in Fig. 2.29, where the brackets indicate average over all pairs, as a function of the time interval $\tau$.

Because of the presence of the guiding field, the parallel separation $r_z$ has the same "free-streaming" behavior as the single-particle displacement depicted in Fig. 2.9. On the other hand, the perpendicular separation shows two regimes. The first is for separations lying in the inertial range, namely $d_i^2 \lesssim \langle r^2 \rangle \lesssim \lambda_c^2$, with $\lambda_c^2 \sim 10^2 d_i^2$. The scaling exponent of the mean squared separation in this range is $\lesssim 2$ as pointed out by Servidio et al. (2016) and depends on the spectral properties

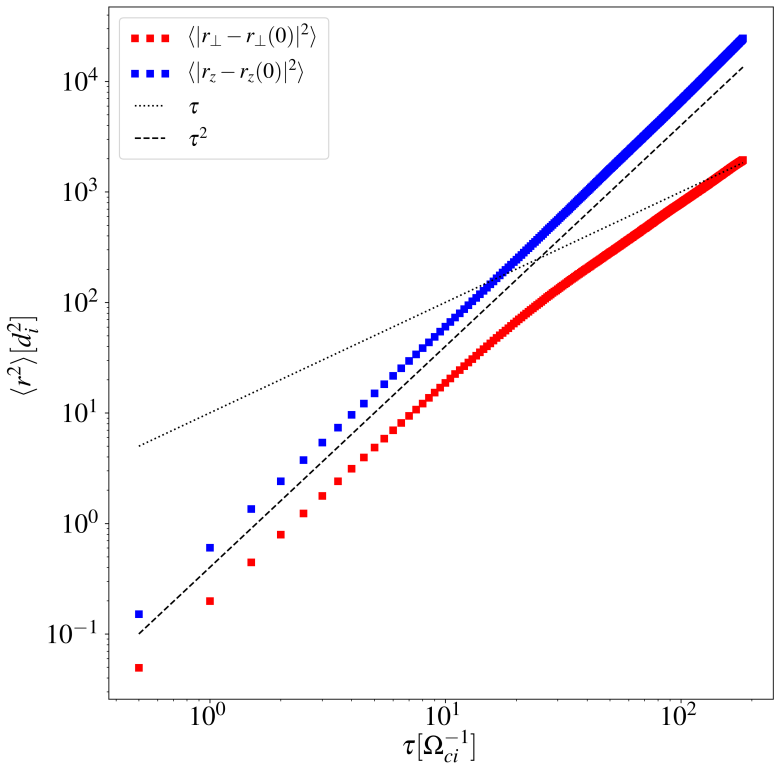


Figure 2.29: Mean squared separation of particle pairs in the perpendicular (red squares) and parallel (blue squares) directions. Lines proportional to $\tau$ (dotted) and $\tau^2$ (dashed) are reported for reference.

of turbulence as Eq. 2.53 infers, and as we qualitatively show in the following. In Fig. 2.30, we plot the distribution of the separation at two separate times. One can notice the development of anisotropy at later times. This anisotropy is modulated by the magnetic field since it develops in the parallel direction and produces non-Gaussian features.

Magnetic field structure function, defined as $S_B^2(\ell, t^*) = \langle|B(\boldsymbol{r}+\ell, t^*) - B(\boldsymbol{r}, t^*)|^2\rangle$ is shown in Fig. 2.31 at the same times of the separation distribution of Fig. 2.30.

The structure function shows the same anisotropy development of the separation distribution, suggesting a strong correlation between field Eulerian properties and particle Lagrangian behavior. The importance of this study arises from two complementary perspectives: (I) the impossibility of Lagrangian measurements from spacecraft. In this way, such properties could be inferred from the already available field data. The high-resolution measurements of the magnetic field allow precise evaluation of inertial range properties both in spectral (through the Fourier analysis) and configuration (using e.g. the structure function) spaces. As

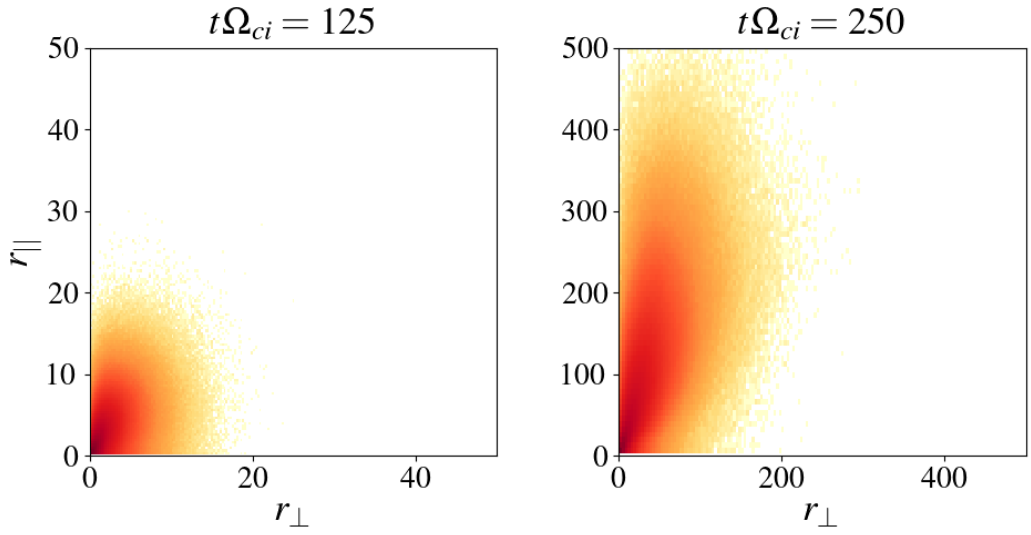


Figure 2.30: Distribution of pair separations in the parallel and perpendicular directions. At later times, the initially Gaussian distribution develops an anisotropy in the parallel direction.

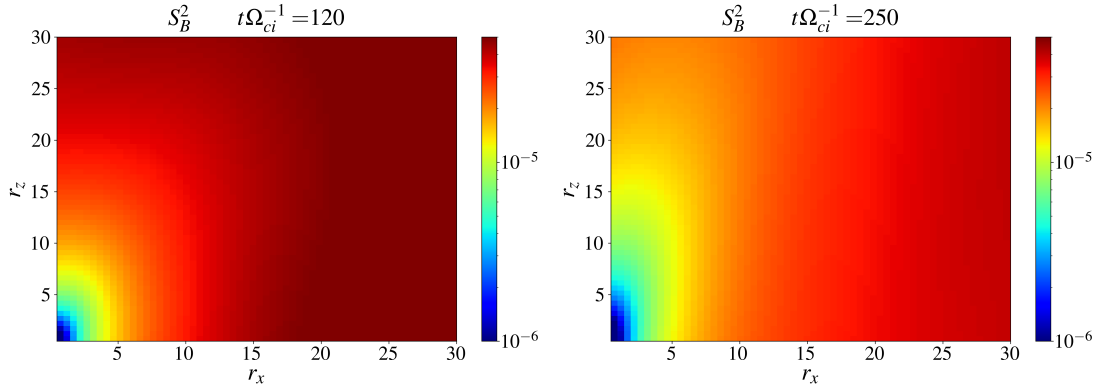


Figure 2.31: Magnetic field second order structure function with increments calculated in the perpendicular and parallel directions at initial and later times. The same behavior of pair separation is found, with anisotropy developing in the parallel direction.

described before, the presence of anisotropic structures in these analyses is reflected in particle Lagrangian properties. (II) Vice versa, observations of plasma dispersion from imaging instruments (DeForest et al., 2015; Ruffolo et al., 2020) may grant the chance to infer properties of plasma turbulence in regions that are not possible to reach with in-situ missions.

# Chapter 3

# Coherent structures in space plasmas

In the previous Chapter, in our journey through the properties of astrophysical plasma turbulence, we have investigated the microscopic effects that happen at the termination of the cascade. We have also inferred that larger scales might influence some properties of particle transport. In the following, we will focus on the mesoscopic structures of the magnetic field.

We know that the basic shape of the magnetic field permeating the heliosphere is that of an outward propagating spiral originating at the Sun's surface (Parker, 1958; Borovsky, 2010; Schwadron & McComas, 2021). There is a lot of observational evidence about the complex, structured texture of the Parker spiral at smaller scales. Some of these features arising from plasma turbulence at different scales have been depicted with simulations in the previous Chapters, and are widely described in literature (Schatten, 1971; Bruno et al., 2001; Borovsky, 2008; Khabarova & Zank, 2017; Malandraki et al., 2019; Verscharen et al., 2019). These characteristics have also been inferred through direct in-situ measurements and indirect effects, despite the impossibility to have an actual map or volume rendering of magnetic field topology, being it global or local. Standard methods of time series and spectral analysis provide only limited information from single-spacecraft measurements. Clusters of satellites provide additional information employing multispacecraft correlation techniques (Chhiber et al., 2018), including "wave telescope" (Glassmeier et al., 2001; Narita et al., 2010) and spacetime ensemble approaches (Matthaeus et al., 2016), though the visual information is still far from that obtainable from simulations.

In studying the nature of magnetic fields in the solar wind, a recurrent view is to describe it in terms of flux tubes. The presence of these structures, on average aligned with the Parker spiral, was initially suggested by McCracken and Ness (1966). This paradigm originated a number of so-called "spaghetti models" which are a particular class of observation-based flux tube models (Schatten, 1971; Bruno et al., 1999; Borovsky, 2008; Hu, 2017). These structures are found in the solar wind at a wide variety of scales. At 1 au, flux ropes of duration ranging from a few minutes to a few hours have been identified from in-situ spacecraft data and studied for decades (Moldwin et al., 1995, 2000; Feng et al., 2008; Cartwright & Moldwin, 2010; Yu et al., 2014). Despite the amount of literature regarding these magnetic field configurations, their origin is still debated. It is not clear yet if such structures originate close to the Sun and are then advected in the interplanetary space, or generate locally due to magnetic reconnection and instabilities, or both (e.g., Pegoraro et al. (1997); Khabarova et al. (2015); Lapenta et al. (2015); Khabarova et al. (2016); Khabarova and Zank (2017); Malandraki et al. (2019); Khabarova et al. (2020)). On the other hand, their large-scale counterparts, such as magnetic clouds, have a clear solar origin related to coronal mass ejections (Gosling, 1990; Webb et al., 2000; Jacobs et al., 2009; Verbeke et al., 2019).

Along with these structures at large scales, also those at small scales are a ubiquitous feature of turbulence, as seen in previous Chapters. Despite the very different typical sizes, they both are coherent structures that are typical solutions of MHD equations, characterized by a finite duration in time, and can be proven uncorrelated with random/stochastic fluctuations of plasma quantities (Greco et al., 2008; Greco, Matthaeus, Servidio, Chuychai, & Dmitruk, 2009; Dudok de Wit et al., 2013; Matthaeus et al., 2015). The abundant presence of flux tubes and current sheets does not make it an easier task to detect them, despite the large efforts of the community (Perri et al., 2012; Zheng et al., 2017; Hu et al., 2018; Zheng & Hu, 2018; Telloni et al., 2020; Zhao et al., 2020). In this Chapter, the focus is given to new methods useful to extract additional topological information from measurements recorded as single-spacecraft time series. Because multi-spacecraft missions are fewer and more expensive than single-spacecraft ones, and because the latest missions – Parker Solar Probe (Fox et al., 2016) and Solar Orbiter (Müller, D. et al., 2020) – will reach unexplored regions as single satellites, the need of extracting as much information as possible from the provided data streams is compelling.

The first method is a novel combination of two well-established techniques that use single-spacecraft 1D measurements: the Grad-Shafranov (GS) reconstruction (Hau & Sonnerup, 1999; Hu, 2017), that provides two-dimensional information about magnetic field topology, and the PVI technique (Greco, Matthaeus, Servidio, Chuychai, & Dmitruk, 2009; Greco et al., 2018), that identifies coherent magnetic structures such as current sheets. In Pecora, Greco, et al. (2019), the GS method was enhanced by synergizing it with the PVI technique, providing additional observational evidence of the complex structure of the solar wind. In fact, the large-scale texture reconstructed with the GS method, at about $10^5 - 10^6$ km, shows flux tubes that are filamentary or "spaghetti-like". The additional information provided by the PVI technique reveals where strong small-scale gradients of the magnetic fields are located. These regions are found at the boundaries of flux ropes/plasmoids where, possibly, reconnection, heating, and particle acceleration are taking place.

The second is a novel method to readily identify flux tubes in data streams, exploiting their helical nature. This novel technique, based on real-space evaluation of magnetic helicity, was developed in Pecora et al. (2020). The signal produced by this quantity shows clustered regions of high helicity that can be associated with the presence of flux tubes. Because $H_m$ signal is related to large-scale structures, it is not dedicated to detecting sharp small-scale boundaries. To identify the discontinuities usually found at the borders of flux tubes, we use again the PVI technique. This method is not intended to distinguish among all the possible classes of helical structures or discontinuities. It rather detects magnetic field topology properties, and this generality grants few-to-no assumptions and ease of implementation.

Last but not least, we will present the results of a yet unpublished work that directly correlates energetic particles with helical structures and high-PVI regions.

## 3.1 The PVI technique

Here we briefly recall and expand the definition of PVI (Eq. 2.41) introduced in Sec. 2.7.

$$\mathrm{PVI}(s,\ell) = \frac{|\Delta \boldsymbol{B}(s,\ell)|}{\sqrt{\langle |\Delta \boldsymbol{B}(s,\ell)|^2 \rangle}},$$

where $\Delta \boldsymbol{B}(s, \ell) = \boldsymbol{B}(s + \ell) - \boldsymbol{B}(s)$ are the increments evaluated at scale $\ell$ and the averaging operation $\langle \dots \rangle$ is performed over a suitable interval (Servidio, Greco, et al., 2011). Note that if $s$ is in the time domain, the lag $\ell$ will be a temporal interval; conversely, if $s$ is in configuration space, $\ell$ will be a spatial increment – the transition between the two domains is always possible when the Taylor hypothesis holds.

In its basic form, PVI is applied to a one-dimensional signal, as would be measured by a spacecraft in the solar wind, or by a fixed probe in a wind tunnel. PVI is essentially a time series of the magnitude of a vector increment with a selected time lag, normalized by its average over an appropriate interval of time (Servidio, Greco, et al., 2011; Greco et al., 2018). It is a "threshold" method, and once a threshold has been imposed on the PVI time series, a collection, or hierarchy, of "events" can be identified. It has been shown that the probability distribution of the PVI statistic derived from a non-Gaussian turbulent signal strongly deviates from that of PVI computed from a Gaussian signal for values of PVI greater than about 3. As PVI increases to values of 4 or more, the recorded "events" are extremely likely to be associated with coherent structures (those which exhibit sharp dipolar patterns, for a broader detection of all types of structures one should use a combination of methods) and therefore inconsistent with a signal having random phases (Dudok de Wit et al., 2013; Matthaeus et al., 2015). The method is intended to be quite neutral regarding the issue of what mechanism generates the coherent structures it detects. Indeed, the method is sensitive to directional and magnitude changes, and any form of sharp gradients in the vector magnetic field $\boldsymbol{B}$. A comprehensive review of the properties of the PVI method providing a broad view of its applications can be found in Greco et al. (2018). In the following, we will concentrate on large scales.

## 3.2 Derivation of the Grad-Shafranov equation

The Grad-Shafranov equation (Grad & Rubin, 1958; Shafranov, 1966) describes an ideal quasi-static MHD equilibrium for plasmas with a preferential direction of symmetry, such as axisymmetric toroidal plasma in tokamaks or flux ropes in the interplanetary space. The set of MHD equations used to obtain the GS equation is

$$\boldsymbol{\nabla} \cdot \boldsymbol{B} = 0, \tag{3.1}$$

$$\boldsymbol{\nabla} \times \boldsymbol{B} = \mu_0 \boldsymbol{j}, \tag{3.2}$$

$$\boldsymbol{\nabla} p = \boldsymbol{j} \times \boldsymbol{B}, \tag{3.3}$$

where Eq. 3.3 is the momentum equation with stationarity hypothesis with respect to both time and convective derivatives. The equations contain the magnetic field $\boldsymbol{B}$, the current density $\boldsymbol{j}$, the vacuum permeability $\mu_0$, and the pressure $p = nkT$ with $n$ being the number density, $k$ the Boltzmann constant, and $T$ the temperature. The invariance along one direction, say $\hat{\boldsymbol{z}}$, is equivalent to saying that $\partial/\partial z = 0$. In this configuration, the vector potential $\boldsymbol{A} = (0, 0, A)$ and the magnetic field can be written as

$$\boldsymbol{B} = \left( \frac{\partial A}{\partial y}, -\frac{\partial A}{\partial x}, B_z(x, y) \right), \tag{3.4}$$

or, analogously,

$$\boldsymbol{B} = \boldsymbol{\nabla} A \times \hat{\boldsymbol{z}} + B_z \hat{\boldsymbol{z}}. \tag{3.5}$$

With these conditions, both the vector potential $A$ and the kinetic pressure $p$ are constant along magnetic field lines, as their gradients are always orthogonal to them. Since $\partial p/\partial z = (\boldsymbol{j} \times \boldsymbol{B})_z = 0$, the equilibrium condition in Eq. 3.3 can be rewritten as

$$\boldsymbol{\nabla} p = j_z(\hat{\boldsymbol{z}} \times \boldsymbol{B}_\perp) + \boldsymbol{j}_\perp \times \hat{\boldsymbol{z}} B_z. \tag{3.6}$$

Writing the components $\boldsymbol{B}_\perp = \boldsymbol{\nabla} A \times \hat{\boldsymbol{z}}$, and $\boldsymbol{j}_\perp = \boldsymbol{\nabla} B_z \times \hat{\boldsymbol{z}}/\mu_0$, Eq. 3.6 becomes

$$\boldsymbol{\nabla} p = j_z \left[ \hat{\boldsymbol{z}} \times (\boldsymbol{\nabla} A \times \hat{\boldsymbol{z}}) \right] + \frac{1}{\mu_0} (\boldsymbol{\nabla} B_z \times \hat{\boldsymbol{z}}) \times \hat{\boldsymbol{z}} B_z. \tag{3.7}$$

Using triple product rules $\hat{\boldsymbol{z}} \times (\boldsymbol{\nabla} A \times \hat{\boldsymbol{z}}) = \boldsymbol{\nabla} A$, and $(\boldsymbol{\nabla} B_z \times \hat{\boldsymbol{z}}) \times \hat{\boldsymbol{z}} B_z = -\boldsymbol{\nabla} B_z$. From Eq. 3.2, $j_z = -\nabla^2 A/\mu_0$ and

$$\boldsymbol{\nabla} p = -\frac{1}{\mu_0} \nabla^2 A \boldsymbol{\nabla} A - \frac{1}{\mu_0} B_z \boldsymbol{\nabla} B_z. \tag{3.8}$$

Since $p$ and $B_z$ are constant along magnetic field lines, they can be expressed as $p = p(A)$ and $B_z = B_z(A)$ and spatial gradients become $\boldsymbol{\nabla} = (d/dA)\boldsymbol{\nabla} A$.

Finally, Eq. 3.8 becomes the well-known GS equation

$$\nabla^2 A = -\mu_0 \frac{d}{dA}\left(p + \frac{B_z^2}{2\mu_0}\right). \tag{3.9}$$

## 3.3 GS reconstruction algorithm

In literature, a lot of effort has been devoted to the development of an efficient and precise algorithm for the reconstruction of 2D cross-sections of magnetic flux ropes encountered in the solar wind by single spacecraft. In the overwhelming number of research associated with this topic in the last decades (Sonnerup et al., 1987; Sonnerup & Guo, 1996; Hau & Sonnerup, 1999; Möstl et al., 2009; González et al., 2015; Hu, 2017), some common steps can be recovered that are necessary for the reconstruction algorithm. First of all, the possible flux rope has to be identified with available data of magnetic field, plasma temperature, and density. Indeed, such structures have peculiar properties such as the rotation of the magnetic field, or particle density showing a deviation from that of the ambient solar wind. Then, from the selected interval, a set of M measurements of the magnetic field, plasma velocity, density, and temperature is extracted.

### 3.3.1 The deHoffmann-Teller frame

As a first step, it is convenient to calculate the deHoffmann-Teller (HT) frame of reference, which refers to the Galilean frame of reference in which the electric field vanishes (De Hoffmann & Teller, 1950). The existence of such a reference frame implies that the structure the spacecraft is traversing is stationary (at least to a zero-order extent). When the HT frame exists, it moves at a certain velocity $\boldsymbol{V}_{HT}$ such that the electric field $\boldsymbol{E}'$ in this frame is

$$\boldsymbol{E}' = \boldsymbol{E} + \boldsymbol{V}_{HT} \times \boldsymbol{B} = 0, \tag{3.10}$$

where $\boldsymbol{E}$ is the electric field measured by the spacecraft in its own frame of reference. The stationariety of the structure follows immediately by writing Faraday's law in the HT frame: $\boldsymbol{\nabla} \times \boldsymbol{E}' = -\partial \boldsymbol{B}/\partial t = 0$. For a set of $M$ spacecraft measurements of plasma bulk velocity $\boldsymbol{v}_m$ and magnetic field $\boldsymbol{B}_m$, $m = 1, \ldots, M$, the

HT velocity can be found as the velocity $\boldsymbol{V}$ that minimizes the quantity

$$D(\boldsymbol{V}) = \frac{1}{M}\sum_{m=1}^{M} |\boldsymbol{E}'_m|^2 = \frac{1}{M}\sum_{i=1}^{M} |\,(\boldsymbol{v}_m - \boldsymbol{V}) \times \boldsymbol{B}_m|^2. \tag{3.11}$$

Since $D(\boldsymbol{V})$ is a quadratic form of its vector argument, it must have a unique minimum that can be found with the minimization condition $\boldsymbol{\nabla}_{\boldsymbol{V}} D = \boldsymbol{0}$.

This condition can be expressed as (Paschmann & Daly, 1998)

$$K_0 \boldsymbol{V}_{HT} = \langle K_m \boldsymbol{v}_m \rangle, \tag{3.12}$$

where each $K_m$ is proportional to the projection matrix $P_m$ into a plane perpendicular to $\boldsymbol{B}_m$, namely

$$K_{m,ij} = B_m^2 \left( \delta_{ij} - \frac{B_{m,i} B_{m,j}}{B_m^2} \right) \equiv B_m^2 P_{m,ij} \tag{3.13}$$

and $K_0 = \langle K_m \rangle$, where the operation $\langle \dots \rangle$ represents an average over the set of $M$ measured quantities. Assuming $K_0$ to be non-singular, the HT velocity can be readily found with a simple matrix inversion

$$\boldsymbol{V}_{HT} = K_0^{-1} \langle K_m \boldsymbol{v}_m \rangle. \tag{3.14}$$

At this point, the system is moved into the HT reference frame, that is the reference frame with such a velocity. In this system, the spacecraft passes through the structure with velocity $-\boldsymbol{V}_{HT}$. In general, the above analysis provides a "proper", but not unique, frame of reference. The goodness of the obtained HT frame can be quantified by correlating the components of the measured electric field ($\boldsymbol{E}_m = -\boldsymbol{v}_m \times \boldsymbol{B}_m$) with the ones in the HT frame ($\boldsymbol{E}' = -\boldsymbol{V}_{HT} \times \boldsymbol{B}_m$). A correlation coefficient of 1 corresponds to the perfect HT frame ($D(\boldsymbol{V}_{HT}) = 0$). In the following treatment, $\boldsymbol{V}_{HT}$ is considered constant throughout the whole encounter, but it is possible to determine a time-varying velocity $\boldsymbol{V}_{HT}(t) = \boldsymbol{V}_{HT}(0) + \boldsymbol{a}_{HT}\, t$ (Hu & Sonnerup, 2002).

#### Negligible convective inertia terms

The HT frame, when it exists, is not unique, and it is a good practice to check if the frame obtained with Eq. 3.14 is acceptable. Indeed, when $\boldsymbol{V}_{HT}$ is found, any residual velocity in the HT frame should be aligned with the magnetic field

(Hu & Sonnerup, 2002). A measure of the deviation from this assumption can be evaluated with cross-field velocity components. Specifically, the flow velocities in the HT frame, should be much lower than the Alfvén speed. Indeed, the time-stationary momentum equation needs to get rid of the convective derivative to let GS equation to be derived from $\boldsymbol{\nabla} p = \boldsymbol{j} \times \boldsymbol{B}$. The convective derivative can be written as

$$(\boldsymbol{v} \cdot \boldsymbol{\nabla})\, \boldsymbol{v} = \boldsymbol{\nabla} \left( \frac{v^2}{2} \right) = \boldsymbol{\nabla} \left( M_A^2 \frac{v_A^2}{2} \right), \tag{3.15}$$

where $\boldsymbol{v}_A = \boldsymbol{B}/\sqrt{4\pi n m_i}$ is the Alfvén speed, and $M_A$ is the Alfvénic Mach number, namely $M_A^2 = v^2/v_A^2$. Therefore, to neglect this term, it has to be $M_A \ll 1$ or equivalently $|\boldsymbol{v}| \ll |\boldsymbol{v}_A|$. A historical way to check this constraint is the so-called Walén plot, namely a scatter-plot of $\boldsymbol{v}' = \boldsymbol{v}_m - \boldsymbol{V}_{HT}$ versus $\boldsymbol{v}_A$ for each direction. When the regression line of such a scatter plot has small values, the inertia term can be safely neglected (Sonnerup & Guo, 1996).

### 3.3.2 Reconstruction frame

Once the HT frame has been found, the next step is to determine the proper frame in which the cross-section of the structure can be reconstructed. This is a trial-and-error process that has to be repeated until a certain control parameter is small enough. Let $\boldsymbol{S} = (\hat{\boldsymbol{x}}, \hat{\boldsymbol{y}}, \hat{\boldsymbol{z}})$ be the final reconstruction frame and $\boldsymbol{S'} = (\hat{\boldsymbol{x}}', \hat{\boldsymbol{y}}', \hat{\boldsymbol{z}}')$ the first-guess coordinate system that is continuously adjusted in the system $\boldsymbol{S''} = (\hat{\boldsymbol{x}}'', \hat{\boldsymbol{y}}'', \hat{\boldsymbol{z}}'')$ until the proper frame is found.

#### First guess

The trial-and-error process starts with a first guess of the $\boldsymbol{S'}$ frame that will be adjusted by small steps. The direction $\hat{\boldsymbol{x}}'$ is placed along $-\hat{\boldsymbol{V}}_{HT}$, with $\hat{\boldsymbol{V}}_{HT}$ being the unit vector in the direction of the HT velocity. At this point, $\hat{\boldsymbol{x}}'$ is directed along the spacecraft trajectory, $\hat{\boldsymbol{y}}'$ must be orthogonal and can be found through a constrained eigenvalue problem. In fact, the first estimate for the $\hat{\boldsymbol{y}}'$ axis coincides with the direction of maximum variance obtained as the eigenvector corresponding to the largest eigenvalue of the matrix $PMP$ where $M$ is the variance matrix defined as $M_{ij} = \langle B_{m,i} B_{m,j} \rangle - \langle B_{m,i} \rangle \langle B_{m,j} \rangle$ and $P$ is the projector $P_{ij} = \delta_{ij} - \hat{V}_{HT,i} \hat{V}_{HT,j}$. The eigenvalue problem for $PMP$ returns the eigenvalues $\lambda_1 > \lambda_2 > \lambda_3$, and the corresponding eigenvectors $\hat{\boldsymbol{e}}_1, \hat{\boldsymbol{e}}_2, \hat{\boldsymbol{e}}_3$. Hence, the direction $\hat{\boldsymbol{y}}' = \hat{\boldsymbol{e}}_1$. This decision is based on the assumption that a flux rope is characterized by

one component (here $B_y$ by construction) flipping sign and the magnetic variance is likely to be larger in this direction (Hu & Sonnerup, 2002). The direction $\hat{\boldsymbol{z}}'$ completes the right-handed orthonormal triad. At this point, the iteration process begins, and is described as follows.

### Iterative steps

In the above determined triad $\boldsymbol{S}'$, the $\hat{\boldsymbol{z}}'$ direction is rotated over a hemisphere of radius one, obtaining the temporary direction $\hat{\boldsymbol{z}}''$ (at zeroth step coinciding with $\hat{\boldsymbol{z}}'$). The temporary $\hat{\boldsymbol{x}}''$ direction is along the projection of $-\hat{\boldsymbol{V}}_{HT}$ onto the plane perpendicular to $\hat{\boldsymbol{z}}''$ and $\hat{\boldsymbol{y}}''$ completes the right-handed orthonormal system. The vector potential $A(x,0)$, along the $\hat{\boldsymbol{x}}''$ direction, is calculated using Eq. 3.4, with the measured magnetic field rotated in the $\boldsymbol{S}''$ frame and sampled over a uniform grid in $\hat{\boldsymbol{x}}''$. Namely,

$$A(x,0) = \int_0^x \frac{\partial A}{\partial \xi}\, d\xi = -\int_0^x B_y(\xi,0)\, d\xi \tag{3.16}$$

with the spatial increment

$$d\xi = -\boldsymbol{V}_{HT} \cdot \hat{\boldsymbol{x}}''\, dt. \tag{3.17}$$

At this point, it is possible to verify the GS condition, for which the transverse pressure $P_t(x,0) = p(x,0) + B_z^2(x,0)/(2\mu_0)$ (rhs of Eq. 3.9) is a function of the vector potential alone. For topological reasons, the center of a magnetic island is either a local maximum or minimum of the vector potential (Servidio et al., 2010). Moreover, since the pressure is constant along field lines, it should have a symmetric profile with respect to the island's center. With these prescriptions, the scatter plot of $P_t(A)$ is expected to have two overlapping branches, one for each half of the crossed island. This double folding behavior is natural to be expected since the spacecraft crosses the same magnetic field lines in the two halves of the island. This property can be exploited to: (I) determine magnetic island boundaries, and (II) construct a measure of the goodness of the reference frame. It can be safely assumed that magnetic field measurements belonging to the same magnetic island are those limited to the overlapping branches, the so-called double folding behavior (see Fig. 3.1). Indeed, if any of the two branches extends more than the other, it means that the spacecraft encountered some magnetic field lines only on one of the two sides. Hence, the measurements to take into account for reconstruction

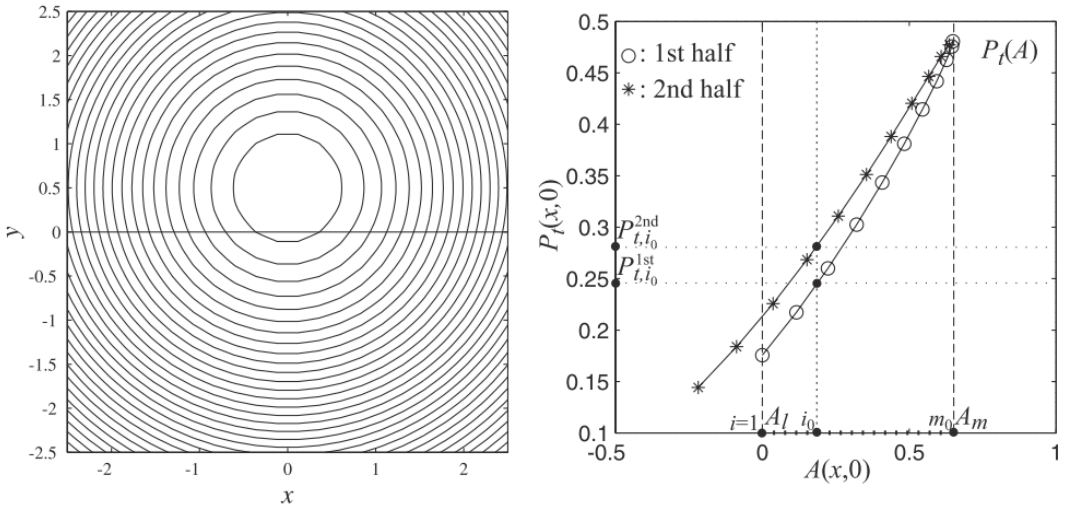


Figure 3.1: (Left) Cross-section of a flux rope centered at $(x, y) = (0, 0.5)$ with the line at $y = 0$ representing the spacecraft trajectory. (Right) Scatter plot of $P_t(A)$ along $y = 0$. Measurements on the left half ($x < 0$) are reported with circles and those of the second half ($x > 0$) with asterisks. The two branches (first and second halves) are not perfectly overlapping, indicating an incorrect choice of the reference frame. Moreover, they also show one branch (second half) that is more extended than the other. The two measurements of the second half with $A < 0$ are not considered when computing the functional form of $P_t(A)$. Adapted from Hu and Sonnerup (2002).

are only the ones that show the aforementioned double folding behavior. From the scatter plot of $P_t(A)$ it is possible to determine the minimum and maximum value of $A$ over which the island expands and discard the possible single-branched values. An example from Hu and Sonnerup (2002) is reported in Fig. 3.1. Following figure notation, the only acceptable values for the magnetic potential are $A_l \leq A \leq A_m$. A uniform grid is defined between these values (as indicated on the horizontal axis) and pressure measurements are interpolated over these points. Now it is possible to retrieve an analytical form for $P_t(A)$ that can be derived with respect to $A$, to get the complete r.h.s of Eq. 3.9. Appropriate functions to accomplish this task are exponentials and polynomials when monotonic behavior can be ensured (Hau & Sonnerup, 1999; Hu & Sonnerup, 2002; Möstl et al., 2009; Hu, 2017).

The "goodness" of the reference frame can be measured, as suggested in Hu and Sonnerup (2002), computing the point-wise distance of the pressure values belonging to the two branches, normalized to the total pressure variation. Such residual is defined as

$$\mathcal{R} = \frac{\sqrt{\sum_{i=1}^{N} \left(P_{t,i}^{1st} - P_{t,i}^{2nd}\right)^2}}{|\max\{P_t\} - \min\{P_t\}|}, \tag{3.18}$$

where $N$ is the total number of points in which the interval $[A_l, A_m]$ is divided, and $P_{t,i}^{1st}$, $P_{t,i}^{2nd}$ are the pressure values at the *i-th* point on the left and right branches respectively. The denominator is the difference between the maximum and minimum values of the pressure within the double-folding portion of data. This normalization condition ensures that minimum residual directions are not short-branched. The direction of minimum residual, of all the directions on the hemisphere that $\hat{\boldsymbol{z}}''$ points to, is the optimal frame of reference for the reconstruction, namely $\boldsymbol{S} = \boldsymbol{S}''(\min\{\mathcal{R}\})$.

### 3.3.3 GS solver

Once the optimal frame $\boldsymbol{S}$ has been found, it is finally possible to solve the full GS equation (Eq. 3.9) to reveal the cross-section of the flux rope. The grid is chosen such that the separation in the $x$ direction belongs in the MHD range; in the orthogonal direction, the step has to be small enough to capture interesting features of the cross-section, but not too much in order to avoid early exponential growth of irregularities or distorted shapes. The vector potential $A(x, y)$ at $y$ values away from the spacecraft trajectory $(x, y = 0)$ is calculated with the following second-order Taylor expansion (Sonnerup & Guo, 1996; Hu & Sonnerup, 2002)

$$A(x, y + \Delta y) \simeq A(x, y) + \left(\frac{\partial A}{\partial y}\right)_{x,y} \Delta y + \frac{1}{2}\left(\frac{\partial^2 A}{\partial y^2}\right)_{x,y} (\Delta y)^2, \tag{3.19}$$

where each term on the rhs is known at any given $(x, y)$ position, and steps are taken at $\pm|\Delta y|$ away from $y = 0$. The second-order derivative is calculated from Eq. 3.9 as

$$\frac{\partial^2 A}{\partial y^2} = -\frac{\partial^2 A}{\partial x^2} - \mu_0 \frac{dP_t}{dA}. \tag{3.20}$$

The second-order derivative in the $x$ direction can be computed with a central finite-difference scheme

$$\left(\frac{\partial^2 A}{\partial x^2}\right)_i = \frac{A_{i-1} - 2A_i + A_{i+1}}{(\Delta x)^2}; \qquad i = 2, \ldots, M-1 \tag{3.21}$$

with the error $O(\Delta x^2)$. The first and the last point of the grid are calculated with forward and backward schemes with the same precision as the central scheme

$$\left(\frac{\partial^2 A}{\partial x^2}\right)_1 = \frac{2A_1 - 5A_2 + 4A_3 - A_4}{(\Delta x)^2}, \tag{3.22}$$

$$\left(\frac{\partial^2 A}{\partial x^2}\right)_M = \frac{-A_{M-3} + 4A_{M-2} - 5A_{M-1} + 2A_M}{(\Delta x)^2}. \tag{3.23}$$

If the first and last points are not computed, the reconstruction domain will be rhombus-shaped due to the progressive restriction of the reconstructed line (Sonnerup & Guo, 1996; Hau & Sonnerup, 1999). The magnetic field component $B_x$ is advanced at farther $y$ positions, using a first-order Taylor expansion and exploiting the vector potential second-order derivative calculated above

$$B_x(x, y + \Delta y) = B_x(x, y) + \left(\frac{\partial^2 A}{\partial y^2}\right)_{x,y} \Delta y. \tag{3.24}$$

As pointed out by Hau and Sonnerup (1999), solving the GS equation with boundary conditions is formally equivalent to integrating a Laplace's equation as a Cauchy problem, and these problems are prone to developing singularities after a finite amount of integration steps. The reason lies in the numerical scheme intercepting spurious exponential solution of the equation, associated with small wavelengths in the $x$ direction. The growth rate of these solutions along the transverse direction ($y$), is larger the shorter the characteristic wavelength of the "anomaly". The development of such singularities can be suppressed with a running three-point average of the vector potential at each step of integration. Namely,

$$\bar{A}_1 = w(y)A_1 + \frac{1 - w(y)}{2}\left(A_1 + A_2\right), \tag{3.25}$$

$$\bar{A}_i = w(y)A_i + \frac{1 - w(y)}{2}\left(A_{i-1} + A_{i+1}\right), \qquad i = 2, M-1, \tag{3.26}$$

$$\bar{A}_M = w(y)A_M + \frac{1 - w(y)}{2}\left(A_{M-1} + A_M\right), \tag{3.27}$$

where $w(y)$ is a weight function defined as

$$w(y) = 1 - \frac{1}{3}\frac{|y|}{|L_y|}, \tag{3.28}$$

and $L_y$ is the total length to which the reconstruction domain is extended to (Hau & Sonnerup, 1999; González et al., 2015).

## 3.4 The GS and PVI method in space data

As already depicted, turbulent plasmas can be imagined as a carpet of large-scale structures, bounded by intermittent, dynamical small-scale regions (Kraichnan & Panda, 1988; Servidio et al., 2008). To confirm this view, in Pecora, Greco, et al. (2019) we proposed a novel technique for describing and visualizing the local topology of the magnetic field using single-spacecraft data. The approach merges two established techniques: the GS reconstruction method, described in previous Sections, which provides a plausible two-dimensional map of the magnetic field surrounding the spacecraft; and the PVI technique, described in Sec. 3.1, that identifies small-scale coherent structures, such as current sheets. Our view, supported not only by observational analysis but also extensively by numerical simulations over a wide range of scales (Greco, Matthaeus, Servidio, Chuychai, & Dmitruk, 2009; Greco, Matthaeus, Servidio, & Dmitruk, 2009; Servidio, Greco, et al., 2011), maintains that the presence of small-scale magnetic flux ropes or islands is intrinsic to strictly 2D-MHD turbulence. Small-scale quasi-2D flux ropes are believed to be the byproduct of the solar wind turbulence dynamic evolution process, resulting in the generation of coherent structures including small random current, current cores, and current sheets over the inertial range length scales (Matthaeus & Montgomery, 1980; Veltri, 1999; Greco, Matthaeus, Servidio, Chuychai, & Dmitruk, 2009).

For this work, the GS equation has been solved with an automated numerical solver to quicken the procedure of finding GS equilibrium structures and reconstructing their topology. A detailed description of the steps of this method is given in previous Section and in Hu and Sonnerup (2002) and Hu (2017) (see also recent different applications in the Magnetospheric Multiscale Mission (MMS) community; Sonnerup et al. (2016); Hasegawa et al. (2019)). The output of the GS method that we analyzed provides the magnetic field and the electric current

density over a rectangular domain surrounding the spacecraft path.

We employed in situ measurements of the interplanetary magnetic field and plasma parameters from the Wind spacecraft. Specifically, for 2016 January, we use 1-minute cadence data sets from the Magnetic Field Investigation (MFI; Lepping et al. (1995)) and the Solar Wind Experiment (SWE; Ogilvie et al. (1995)) instruments. All data are accessed via the NASA Coordinated Data Analysis Web (CDAWeb). For this period, we obtained $\sim 400$ magnetic islands, or flux tube cross-sections, via the GS reconstruction and $\sim 400$ PVI events, calculated with a time lag $\tau = 2$ minutes, applying a typical threshold $\theta = 3.7$ on the PVI signal that is more likely to detect coherent structures (Greco et al., 2018; Chhiber, Goldstein, et al., 2020). The average that appears in the denominator of Eq. 2.41 has been computed over an appropriately long dataset (Servidio, Greco, et al., 2011). In Fig. 3.2 we show an example of how the PVI and the GS methods work in synergy. The plot is a 2-day-long time series of solar wind speed and magnetic field measurements. The occurrence of flux ropes is indicated with horizontal lines, each above-threshold PVI event extends within consecutive star and circle. The vertical arrows point to the more extreme PVI events that clearly appear at the borders of the magnetic islands. The inset provides an expanded view of a shorter period of about 9 hours. Applying both methods simultaneously enables plausible identification of both flux tubes and coherent current structures at their boundaries, and it can be done in any single (or multiple) spacecraft measurements.

Some examples of reconstructed flux ropes (in 2D grids of $21 \times 141$ points), and magnetic discontinuities detected with the PVI method are shown in Fig. 3.3. Cross-sections of flux tubes are represented with color shading of the out-of-plane current density (top panels) and magnetic field (bottom panels), along with vector potential contour lines. PVI events extensions are delimited with stars (beginning) and circles (end). For larger structures, PVI events are quasi point-wise (stars and circles are overlapped) since their extension is not appreciable. The cross-sections of the flux ropes are represented in the local reconstruction frame $(x, y, z)$, with the $z$-axis representing the symmetry axis of the flux rope.

Three cases are shown: (I) left panels show a large magnetic island with strong PVI events, probably X-points, localized at the borders. The perpendicular extent of this island is about $2 \times 10^6$ km. Its $z$-axis is mainly in the GSE $x - y$ plane. (II) Within the large structure shown in middle panels, we found PVI events at the external boundaries – as in the previous case –, but also at internal boundaries

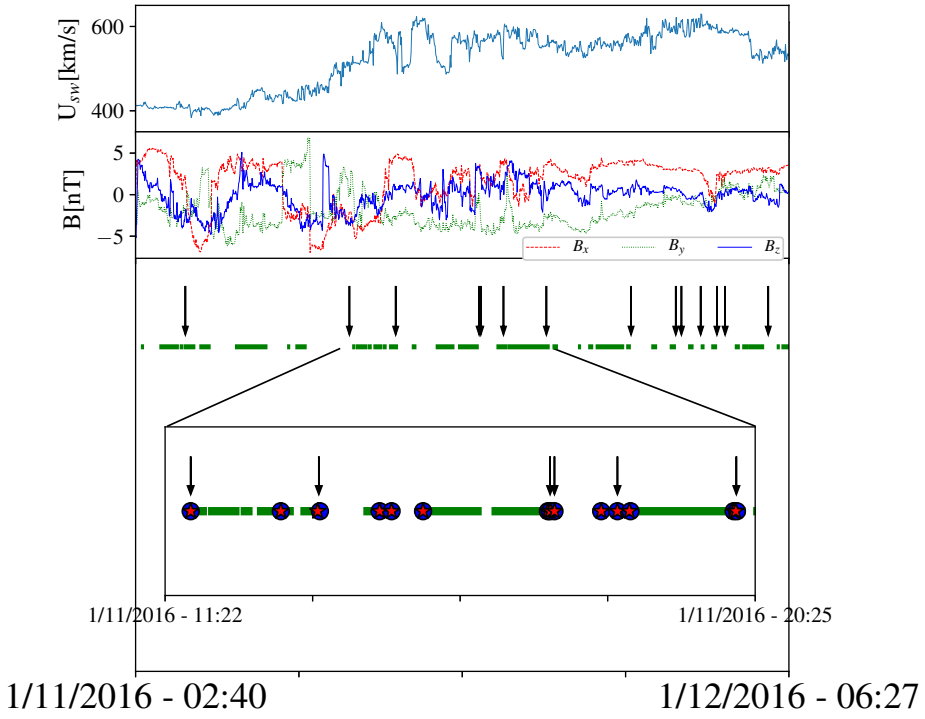


Figure 3.2: Short time window of the 2016 January data set (approximately 2 days). The two top panels display the solar wind bulk speed and magnetic field components. The green horizontal lines represent the duration of the reconstructed flux ropes, the red stars and the blue circles (indicated in the inset) are the start and end times of PVI events respectively. The black arrows indicate locations of larger PVI values. From Pecora, Greco, et al. (2019).

between two smaller structures enclosed within the larger one, showing a more complex magnetic field texture. The internal PVI could be interpreted as a core current; however, since it is located between two secondary islands, it could also be associated with a reconnection event. Here, the local $z$ and GSE $z$-axes almost coincide. (III) The right panels show a PVI event found within the core of a small magnetic island – about $3 \times 10^4$ km across. This is probably a current sheet internal to the flux tube, associated with the bunching of magnetic flux near the central axis, which can be classified as an O-point. In this case, the axis of the flux rope points along the GSE $y$-axis.

In the GS method, the boundaries of a given flux tube are determined by the double-folding requirement on $P_t(A)$. In contrast, the PVI method identifies a boundary as a local condition on the magnetic field vector increment. The boundaries are therefore determined independently in the two cases, and the finding

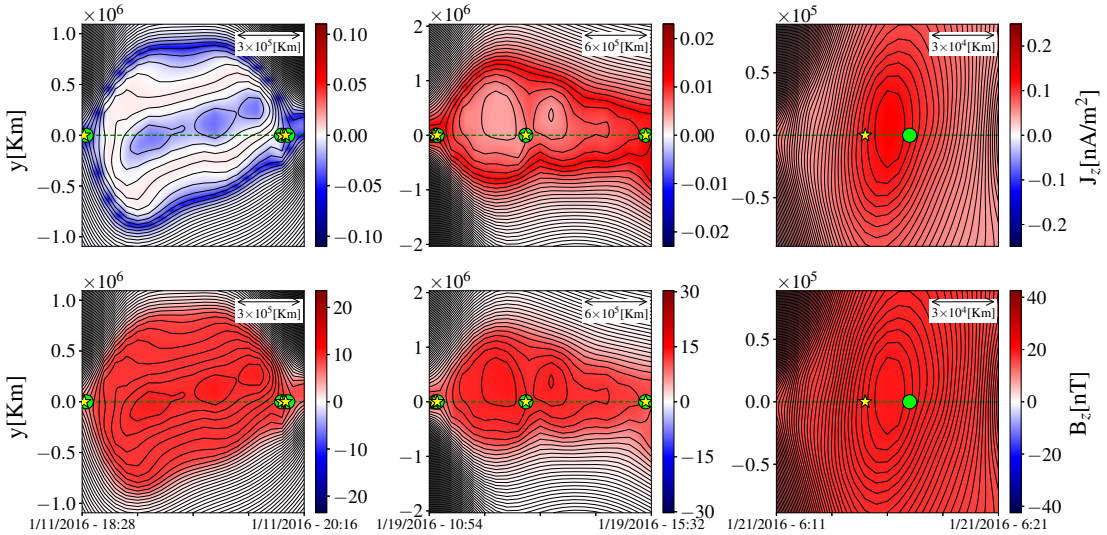


Figure 3.3: Reconstructed flux ropes for Wind 2016 January in the local frame $(x, y)$, with the $z$-axis representing the cylindrical axis of the flux rope. Magnetic potential contour lines with filled color plots of $J_z$ (top panels) and $B_z$ (bottom panels). The dashed lines at $y = 0$ are the projection of the spacecraft path on the flux rope cross-section. The yellow stars and the green circles represent the start and endpoints of the PVI events, respectively. The distances in the transverse directions are in km, and they may be considered directly proportional to the magnetic flux across the flux rope. The $x$-axis of the figures represents the observation period, which we transformed into spatial dimensions (indicated by the insets with the rulers) applying the Taylor hypothesis. From Pecora, Greco, et al. (2019).

that they frequently occur at the same or similar positions (see Figs. 3.2 and 3.3) indicates a good synergy between the GS and the PVI methods. One should be cognizant of the fact that current sheets in weakly 3D turbulence (Wan et al., 2014) may also appear within flux tubes but separated both from the magnetic axis (core) and the X-points that may be found at the boundary. We are not aware that such current configurations have been reported as emerging in the purely 2D geometry assumed in the GS method. Evidently, at least a generalization to a weakly 3D reduced MHD model is required (Rappazzo & Velli, 2011; Wan et al., 2014). Nevertheless, the GS method may detect signatures of such currents in the solar wind, even if this cannot emerge in a purely 2D dynamical model. The reconstruction method assumes a local 2D geometry that is organized by a strong local, out-of-plane guide field $B_z$ (Oughton et al., 2015); this state is characterized by spatial derivatives along the $z$ direction that are weak relative to those com-

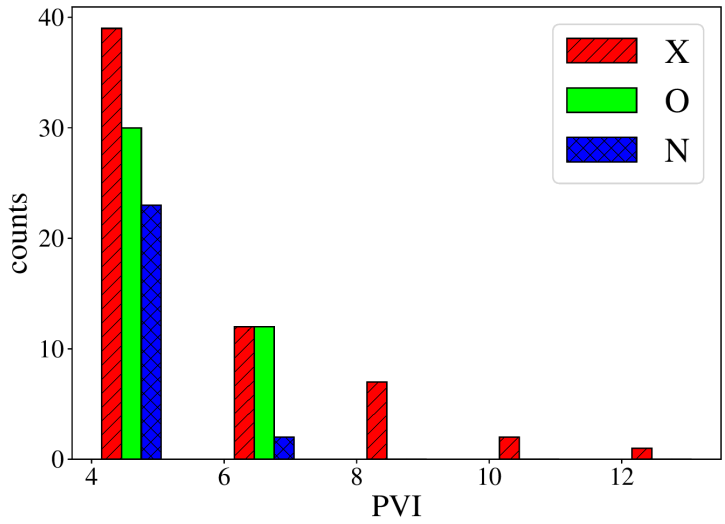


Figure 3.4: Histograms of PVI events classified as X (striped red), O (plain green), and N (crossed blue). The histogram bins have the same width equal to 2, starting from PVI = 3.7. From Pecora, Greco, et al. (2019).

puted in the perpendicular plane. Consequently, a measure of the goodness of the reconstruction may be given by the quantity

$$\mathcal{A} = \frac{\sqrt{\langle \boldsymbol{B}_\perp^2 \rangle}}{B_z} \tag{3.29}$$

where the averaging operation $\langle \dots \rangle$ is made over a moving window. By requiring that this quantity is less than 1 we may exclude some of the reconstructed flux ropes. Typical values of $\mathcal{A}$ are of the order of $0.1 - 0.2$ for the "good cases". However, in a few cases, we also found values of $\mathcal{A}$ around $0.6 - 0.8$ for good reconstructions. At this point, it is interesting to examine the statistics of the location of PVI events with respect to the magnetic islands. For example, are the more intense current sheets occurring at the boundaries of the islands (X-points)? To answer this question, we classified the PVI events as X (possibly associated with reconnection events), O (core currents), or N (no classification). One explanation for N-events could be that the spacecraft moving in the solar wind may not come directly across the X- or O-points, and the resulting topology cannot be clearly distinguished. The statistical analysis of over 150 classified events is shown in Fig. 3.4.

The histogram confirms that the events with the highest PVI values are located at the borders of magnetic islands (where one expects tangential discontinuities and possible X-points); instead, the cores of the flux ropes (O-points) are charac-

terized by smaller PVI values. The unclassified events are fewer and at relatively small PVI values. This observational evidence is in agreement with the numerical results obtained from the 2D compressible MHD simulation shown in Greco, Matthaeus, Servidio, Chuychai, and Dmitruk (2009). A physically appealing interpretation emerged: very low values of current lie mainly in wide regions (lanes) among magnetic islands. These are associated with local small-amplitude nonlinearities, and possibly wave-like activity (Howes et al., 2018) and other transient random currents (Greco et al., 2016; Franci et al., 2017). Moderate currents, required by Ampere's law for any flux tube carrying nonzero current, populate the central regions of magnetic islands (or flux tubes). And, finally, strong current sheet-like structures form narrow regions (sharp boundaries) between magnetic islands (Bruno et al., 2001). Current sheets represent the well-known small-scale coherent structures of MHD turbulence that are linked to magnetic field intermittency. This classification provides a real-space picture of the nature of intermittent MHD turbulence, and it also found confirmation in the observational data (Matthaeus & Montgomery, 1980; Veltri, 1999; Servidio et al., 2008).

We now turn to a comparison of the electric current densities implied by the GS and the PVI methods. The GS method, within the parameters of its approximations, returns directly, and at each point, a value of the current density. For the PVI method, we can use the empirical result shown in Fig. 7 of Greco et al. (2018) as a basis for estimating the current density magnitude at sharp discontinuities. The quoted result demonstrates a statistical relationship between the normalized current density, estimated with the curlometer technique (Dundovic et al., 2020), and the multispacecraft PVI index computed from MMS measurements in the Earth's magnetosheath. The relationship is found employing normalization of the current by its rms value $\sigma_J$, a procedure needed to compare current measurements with the PVI that is a non-dimensional quantity. What Greco et al. (2018) suggested, is a correlation between PVI and current density values that can be expressed as

$$\frac{J}{\sigma_J} \simeq 2 \text{ PVI}. \tag{3.30}$$

We suppose that this statistical relationship also applies to the Wind data in the solar wind, and we can use Eq. 3.30 to obtain a measure of $J$. To be useful, this procedure requires the estimation of $\sigma_J$ in the absence of a direct measure of the current (otherwise, one would not need to use Eq. 3.30). A reasonable estimate of

$\sigma_J$ may be obtained based on computing the rms value of the (single-spacecraft) measured vector magnetic field increments $|\Delta \boldsymbol{B}|$. To convert this value in units of current, one divides by the magnetic permeability $\mu_0$ and a length $L \sim 10^4$ km, which may be the typical scale of the current sheets. This estimate comes from the statistical distribution of PVI event duration multiplied by the solar wind speed, and it is consistent with existing values in literature (e.g. Gosling and Szabo (2008)). In this approximation $\sigma_J(\mathrm{Am}^{-2}) = \mathrm{rms}(|\Delta \boldsymbol{B}|/(L\mu_0))$, where the average has been computed over the whole data set. Having $\sigma_J \sim 15 \times 10^{-11} \mathrm{Am}^{-2}$, and the entire PVI signal, $J$ values come from the empirical expression in Eq. 3.30:

$$J_{PVI}\,(\mathrm{Am}^{-2}) \sim 2\ \mathrm{PVI}\ \sigma_J\,(\mathrm{Am}^{-2}). \tag{3.31}$$

The current density values obtained in this way may be compared with those of the current obtained from the GS reconstruction, say $J_{GS}$, within each flux rope, sampled along the spacecraft path ($y = 0$). The PDFs of $J_{PVI}$ and $J_{GS}$ are shown in Fig. 3.5. We emphasize that the currents computed from the two methods are not expected to agree, given that the GS current is effectively based on island cores, while that related to PVI is based on the boundaries. Indeed, Fig. 3.5 shows that the $J_{PVI}$ distribution is shifted toward considerably larger values than the $J_{GS}$ distribution. The most probable GS current occurs at a value that is about two orders of magnitude smaller than the most probable PVI current. The PVI current distribution also exhibits a noticeable extended tail at large values. This finding is consistent with the typical scale of application of the two methods. The PVI looks for small intense gradients, while the GS reconstruction is focused on necessarily smoother MHD structures.

In the next Section, we will present a novel technique developed for the detection of more general equilibrium structures.

## 3.5 Detection of flux ropes via magnetic helicity

Despite the peculiar common signatures that flux tubes show, such as the rotation of one magnetic field component accompanied by large magnetic field magnitude and density lower than the surrounding, ambient solar wind, their identification is not an easy task. Previous studies used the aforementioned properties to find flux tubes (or flux ropes or filaments) in the solar wind beginning with very detailed approaches that examine a number of parameters (McCracken & Ness, 1966;

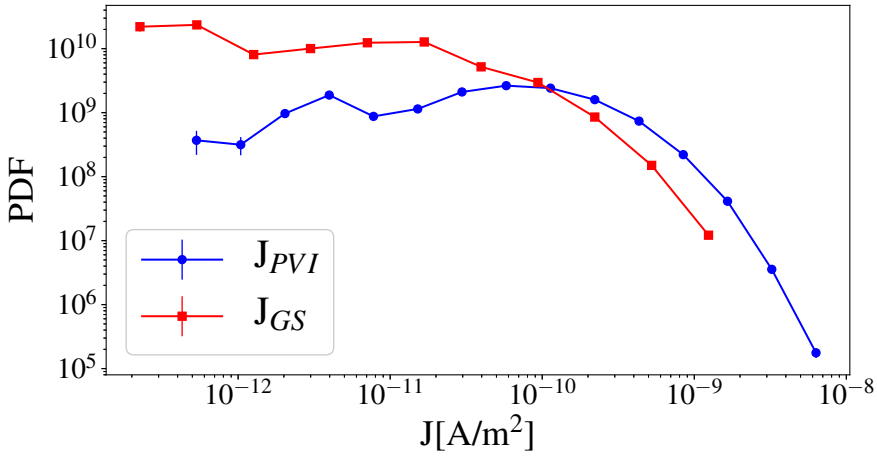


Figure 3.5: Probability density function of the current density evaluated with the GS method (red line) and from the PVI signal (blue line). From Pecora, Greco, et al. (2019).

Burlaga, 1969; Borovsky, 2008). These approaches allow a precise classification of different types of magnetic flux structures. For example, the magnetic fields can be fitted to a Lundquist model to identify relaxed force-free states in magnetic clouds (Burlaga, 1988). Other techniques also enable the identification of other classes of flux tubes or flux ropes. Small-scale flux ropes, such as "plasmoids" associated with byproducts of magnetic reconnection (Matthaeus & Lamkin, 1986), can be implicated in particle energization (Ambrosiano et al., 1988; Drake et al., 2006; Khabarova et al., 2016) and frequently occur in turbulence (Wan et al., 2014). The detection of these structures has been proposed based on cross helicity, residual energy, and magnetic helicity evaluated using a wavelet analysis (Zhao et al., 2020). In the realm of more elaborate techniques, one may also identify flux ropes for special cases that are near-equilibrium and quasi-two-dimensional. Then, the reconstruction methods based on Grad-Shafranov equilibrium (Sonnerup & Guo, 1996; Hu & Sonnerup, 2002) provide a pathway to visualize a 2D map of flux tube cross-sections. It is important to bear in mind that the application of a technique such as GS reconstruction requires the special conditions mentioned in the previous Sections. A "good reconstruction," and therefore a reasonable detection of a GS flux tube, will be possible only when such auxiliary conditions are fulfilled (Y. Chen et al., 2020). On the other hand, if a precise classification of the structure is not needed, one may look for more general properties with which flux tubes in the solar wind can be associated. In particular, MHD equilibrium states can be

found from Eqs. 3.1–3.3 both in the force-free and force-balanced approximations (the latter leading to GS equation). Force-free MHD equilibria can be described by the condition

$$\boldsymbol{\nabla} \times \boldsymbol{B} = \alpha \boldsymbol{B}, \tag{3.32}$$

where $\alpha$ is a scalar function. By taking the divergence of Eq. 3.32, it turns out that $\boldsymbol{B} \cdot \boldsymbol{\nabla}\alpha = 0$. Hence, magnetic field lines lie on constant-$\alpha$ surfaces. Using Hopf's theorem (Alexandroff & Hopf, 2013), it can be shown that the simplest allowed shape for such constant-$\alpha$ surfaces is a torus, and the vector field has helix-like lines of force that wind about the toroidal surface. The result can be generalized in the case of force-balanced equilibria noticing that the surfaces at constant pressure play the same role of the surfaces at constant $\alpha$. In fact, Eq. 3.3 implies $\boldsymbol{B} \cdot \boldsymbol{\nabla} P = 0$. The helix-like shape of magnetic field lines that arises as a solution of MHD equilibrium configurations, suggests that magnetic helicity is a good candidate to be used for the identification of flux tubes in the solar wind.

### 3.5.1 The $H_m$ and PVI method

In the previous Sections, we described the GS method employed in conjunction with the PVI technique to identify near-equilibrium flux tubes and nearby discontinuities (Pecora, Greco, et al., 2019). The result was that magnetic discontinuities are often found to populate both peripheral boundaries of GS flux tubes as well as, in some cases, internal boundaries within the flux tubes when more complex topologies are present (Bruno et al., 2001). In these recent studies, one begins to find verification of the original conjectures that the interplanetary magnetic field consists of filamentary tubes bounded by discontinuities (McCracken & Ness, 1966; Burlaga, 1969), while recent advances provide much more detail to this picture (Khabarova et al., 2016). At this point, it may be useful to distinguish between detection and identification methods. The latter are more complex and involve specialized assumptions, such as the GS methodologies or the quantitative interpretation of fitting to Lundquist states. These more elaborate methods, which one might also call reconstruction methods, typically provide more advanced information about the identified structures when they work; however, they do not always work. While reconstruction methods can provide more information, detection methods can be more versatile and easier to implement. Moreover, reconstruction

methods can also benefit from a preliminary detection step. We will focus on this point.

In this Section, we show the employment of two complementary methods that characterize both the large- and small-scale coherent structures of the turbulent solar wind. This time, instead of GS reconstruction, we use a quantitative evaluation of the magnetic helicity ($H_m$) to detect the presence of flux tubes, again in synergy with the PVI technique to estimate the position of their boundaries. The evaluation of local magnetic helicity employs the novel real-space method, developed in Pecora et al. (2020), that has been shown to readily detect helical flux tubes. The PVI technique is used to detect magnetic discontinuities as potential, both internal and external, boundaries of magnetic flux tubes. We exploit the frequently encountered helical nature of flux tubes to suggest a relatively straightforward alternative to the assumptions of two-dimensionality and equilibrium conditions that are adopted in Grad-Shafranov methods. We may thus understand the $H_m$ and PVI methods to provide complementary information. The proposed technique identifies a certain class of self-organized magnetic structures, with a minimum of hypotheses, and no claim of exhaustive identification.

The approach is based on the assumption that magnetic flux tubes carry a finite amount of current density along their magnetic axis – as we also found in the previous Section. These flux ropes are necessarily characterized by helical magnetic field lines near their magnetic axis, as a consequence of Ampere's law, in a case in which there is a non-null parallel (to the current) magnetic field component. Typically, in simplified representations these structures are treated as 2.5D, with spatial gradients that mainly develop in the 2D plane perpendicular to the electric current density. In addition, a net magnetic field component may lie along the current axis. In envisioning (and simplifying) turbulence as an ensemble of quasi-parallel, large-scale flux tubes, those with the same polarity are often bounded by steep gradients such as small-scale, tangential discontinuities. In anisotropic turbulence, these represent regions of dynamical interactions between adjacent tubes, and they are often observed in simulations (e.g., Matthaeus and Montgomery (1980); Servidio et al. (2009)). When present, these boundaries can be readily identified by a method such as the PVI. The starting point is the magnetic helicity, a rugged invariant of MHD turbulence, defined as

$$H_m = \langle \boldsymbol{a} \cdot \boldsymbol{b} \rangle, \tag{3.33}$$

where $\boldsymbol{a}$ is the magnetic potential associated to the fluctuating magnetic field $\boldsymbol{b}$, and $\langle \dots \rangle$ represents an average over a very large volume, or over a whole isolated system (Woltjer, 1958; J. B. Taylor, 1974; Matthaeus & Goldstein, 1982). This invariant can be estimated by single-spacecraft, 1D measurements, as the out-of-diagonal part of the autocorrelation tensor (Matthaeus et al., 1982), namely

$$H_m = \int_{\infty}^{0} ds_i \; \epsilon_{ijk} \; R_{jk}(\boldsymbol{\gamma}(s)). \tag{3.34}$$

Here $R_{jk}(\boldsymbol{\gamma}) = \langle b_j(\boldsymbol{r}) b_k(\boldsymbol{r}+\boldsymbol{\gamma}) \rangle$ is the correlation tensor evaluated at vector spatial lag $\boldsymbol{\gamma}$, and the fluctuations are assumed to be well described by spatially homogeneous statistics, up to the second order correlations. The line integral is evaluated along a specified curve, parameterized as $\boldsymbol{\gamma}(s)$, from a specified origin at $\boldsymbol{\gamma} = \boldsymbol{0}$, to infinity. The differential line element along $\boldsymbol{\gamma}$ is $d\boldsymbol{s} = ds \; d\boldsymbol{\gamma}(s)/ds$, where $s$ is the scalar displacement along the curve and $d\boldsymbol{\gamma}(s)/ds$ is a unit vector tangent to the curve.

Generally, helicity measurement has been implemented using wavelet transforms (Farge, 1992; Bruno et al., 1999, 2001; Telloni et al., 2012; Zhao et al., 2020). The alternative approach, implemented here, is based on the consideration of the real-space formulation of Eq. 3.34. This defining equation may be arbitrarily decomposed as

$$H_m = \int_{\infty}^{\ell} ds \; \hat{e}_i \; \epsilon_{ijk} \; R_{jk}(s) + \int_{\ell}^{0} ds \; \hat{e}_i \; \epsilon_{ijk} \; R_{jk}(s) = \tag{3.35}$$

$$= H_m^+(\ell) + H_m^-(\ell), \tag{3.36}$$

where the integral is now specialized to the case integration path in a fixed direction $\hat{\boldsymbol{e}}$ with scalar lag $s$. The obvious interpretation is that $H_m^+(\ell)$ is the contribution to helicity from structures larger than $\ell$, while $H_m^-(\ell)$ is the contribution to helicity from structures smaller than $\ell$. The method employed below is the direct evaluation of the special case

$$H_m^-(\ell) = \int_{\ell}^{0} ds \; \hat{e}_i \; \epsilon_{ijk} \; R_{jk}(s), \tag{3.37}$$

where the integral was again calculated in the direction $\hat{\boldsymbol{e}}$ with scalar lag $s$. Hereafter, we refer to $H_m^-$ as $H_m$ when not stated otherwise. It is important to emphasize that this approach provides a cumulative measurement for the helicity

of the fluctuations that have spatial scales less than $\ell$, for which the principle assumption is that the turbulence is spatially homogeneous.

### Implementation

In the usual way, the above mathematical formulation requires a practical interpretation of the ensemble average (usually accomplished by averaging in space or time), which relies on an ergodic theorem (Panchev, 1971). Assuming that single spacecraft measurement is available and that the measurement point is fixed in space, averaging is done in one Cartesian direction, using the Taylor hypothesis (Jokipii, 1973). In this familiar approximation, a spatial lag $s$ is inferred by computing a convected distance in a given time lag, assuming no distortion during this time interval. Therefore, with solar wind speed $\boldsymbol{V} = V\hat{\boldsymbol{e}}$, one approximates $s = -V\tau$, where $\tau$ is the time lag.

With these assumptions, the magnetic helicity of the fluctuations, and other derived quantities, such as its reduced one-dimensional spectrum, may be derived from interplanetary spacecraft data (Matthaeus & Goldstein, 1982). Here we propose a procedure to calculate a local estimate of Eq. 3.37. To obtain an estimate of the requisite elements of the correlation matrix at the point $x$, we averaged the local correlator (symbolically, "$b_2 b_3' - b_3 b_2'$") over a region of width $w_0$ centered about $x$. To avoid effects of large fluctuations at the edges of the investigated data interval, a window was employed to smoothly let the estimates reach zero at the edges, which is a common procedure in correlation analysis (Matthaeus & Goldstein, 1982). Specifically, in the first step, the raw helicity was estimated as

$$C(x,l) = \frac{1}{w_0}\int_{x-\frac{w_0}{2}}^{x+\frac{w_0}{2}} \left[b_2(\xi)b_3(\xi+l) - b_3(\xi)b_2(\xi+l)\right] d\xi. \tag{3.38}$$

This was followed by windowing the correlation function $C(x,l)$ as

$$H_m(x,\ell) = \int_0^{\ell} dl\ C(x,l)h(l) \tag{3.39}$$

where $h(l) = \frac{1}{2}\left[1+\cos\left(\frac{2\pi l}{w_0}\right)\right]$ is the Hann window. The interval of local integration $w_0$ is arbitrary, but we typically chose it as an order unity multiple of the scale $\ell$, such as $w_0 = 2\ell$. The above formulas convert directly to the time domain directly by using the Taylor hypothesis. The boundaries of high-helicity regions will be inferred through the PVI as described in previous Sections. In

the following, we will present some examples of identification with this combined technique, in both simulations and spacecraft measurements using the PSP data.

### 3.5.2 Identification in turbulence simulations

We tested our novel technique by using direct numerical simulations of compressible MHD. We solved the equations (see below) in 2.5D, in a periodic square box of length $2\pi L_0$. All the quantities were normalized to classical Alfvén units. The simulations were performed in the $x$-$y$ plane and a mean magnetic field $B_0 = 1$ is present along the $z$ axis. The velocity and magnetic field fluctuations have all three Cartesian components. The code, based on a very accurate pseudo-spectral method (Gottlieb & Orszag, 1977; Ghosh et al., 1993), as described in Perri et al. (2017), makes use of logarithmic density. In order to preserve the solenoidal condition of the magnetic field, the algorithm solves equations for the magnetic potential $a$ and parallel variance $b_z$ directly, so that the total magnetic field is decomposed as $\boldsymbol{B} = B_z\hat{\boldsymbol{z}} + \boldsymbol{\nabla} a \times \hat{\boldsymbol{z}}$. Here, $B_z = B_0 + b_z$ is the out-of-plane magnetic field, and $\boldsymbol{\nabla} = (\partial/\partial x, \partial/\partial y, 0)$ is the in-plane gradient. The equations that are solved are thoroughly described in Vásconez et al. (2015); Perri et al. (2017), and read:

$$\frac{\partial \rho}{\partial t} = -\boldsymbol{\nabla} \cdot (\rho \boldsymbol{u}) \,, \tag{3.40}$$

$$\frac{\partial \boldsymbol{u}}{\partial t} = -(\boldsymbol{u} \cdot \boldsymbol{\nabla})\, \boldsymbol{u} + \frac{1}{\rho} (\boldsymbol{\nabla} \times \boldsymbol{B}) \times \boldsymbol{B} - \frac{\beta}{2\rho} \boldsymbol{\nabla} (\rho T) - \nu_4 \nabla^4 \boldsymbol{u}, \tag{3.41}$$

$$\frac{\partial \boldsymbol{B}}{\partial t} = \boldsymbol{\nabla} \times (\boldsymbol{u} \times \boldsymbol{B}) - \eta_4 \nabla^4 \boldsymbol{B}, \tag{3.42}$$

$$\frac{\partial T}{\partial t} = -(\boldsymbol{u} \cdot \boldsymbol{\nabla})\, T - (\gamma - 1)(\boldsymbol{\nabla} \cdot \boldsymbol{u}) T - \chi_4 \nabla^4 T, \tag{3.43}$$

where $\rho$ is the mass density, $\boldsymbol{u}$ the bulk velocity, $\boldsymbol{B}$ the total magnetic field, $T$ the temperature, $\gamma = 5/3$ the adiabatic index. The algorithm is stabilized via hyperviscous dissipation with the coefficients $\nu_4$, $\eta_4$, $\chi_4$ of the order of $10^{-9}$. The fourth-order hyperviscosity prevents spurious numerical effects at very small scales (very high $k$-vectors).

The numerical tool described by Eqs. 3.40–3.43 has extensively been tested and used in the past decade for the study of 2D plasma turbulence (Servidio et al., 2009), and also for the study of solar wind discontinuities (Matthaeus et al.,

| ID | $N_x$ | $N_y$ | $\beta$ | $B_0$ |
|---|---|---|---|---|
| ML03 | 4096 | 4096 | 1.0 | 1.0 |
| ML04 | 2048 | 2048 | 1.0 | 1.0 |
| ML05 | 4096 | 4096 | 1.0 | 1.0 |
| ML06 | 4096 | 4096 | 1.0 | 1.0 |
| ML07 | 4096 | 4096 | 0.5 | 1.0 |
| ML08 | 4096 | 4096 | 0.2 | 1.0 |
| ML09 | 4096 | 4096 | 3.0 | 1.0 |
| ML10 | 4096 | 4096 | 0.5 | 1.0 |

Table 3.1: Numerical and physical parameters used for the compressive MHD simulations. ID is the run identifying label, $N_x$ and $N_y$ are the number of grid points in $x$ and $y$ directions, $\beta$ is the ratio between plasma kinetic and magnetic pressures, and $B_0$ is the magnitude of the mean magnetic field.

2015). The parameters we use are, for the most, close to solar wind conditions with a few being closer to those of the magnetosphere and solar corona. Parameter details are listed in Table 3.1.

The initial fluctuations were chosen with random phases, for both magnetic and velocity fields in a shell of Fourier modes with $3 \leq |\boldsymbol{k}| \leq 5$, where the components of wave vector are in units of $1/L_0$. The decaying MHD simulations quickly develop turbulence and small-scale dissipative structures. The magnetic field power spectrum manifests a power-law typical of Kolmogorov turbulence, with a scaling of $P(k) \propto k^{-5/3}$.

The turbulent pattern that arises from the evolution of the system is reported in Fig. 3.6, where we show the current density $j_z$ (color shading) with superimposed 2D contour lines of constant magnetic potential $a$ (black solid lines), which are readily identified with the in-plane projection of the magnetic field lines. The typical features of 2D turbulence are evident, with large-scale coherent structures and narrow, discontinuous contact regions, where one frequently finds that reconnection is occurring (Servidio et al., 2009). These magnetic islands are also the regions where magnetic helicity, computed as $H_m = a\, b_z$ (the 2.5D version of Eq. 3.33), is concentrated and retained throughout the whole simulation, as Fig. 3.7 shows. The visual inspection of $H_m$ maps confirms that magnetic helicity is conserved in our simulations of fully developed turbulence, as expected from (Matthaeus & Goldstein, 1982). In the following, we will look for these helical structures in simulations (to test the technique) and in the solar wind.

Though Fig. 3.7 shows that magnetic helicity concentration is unambiguously

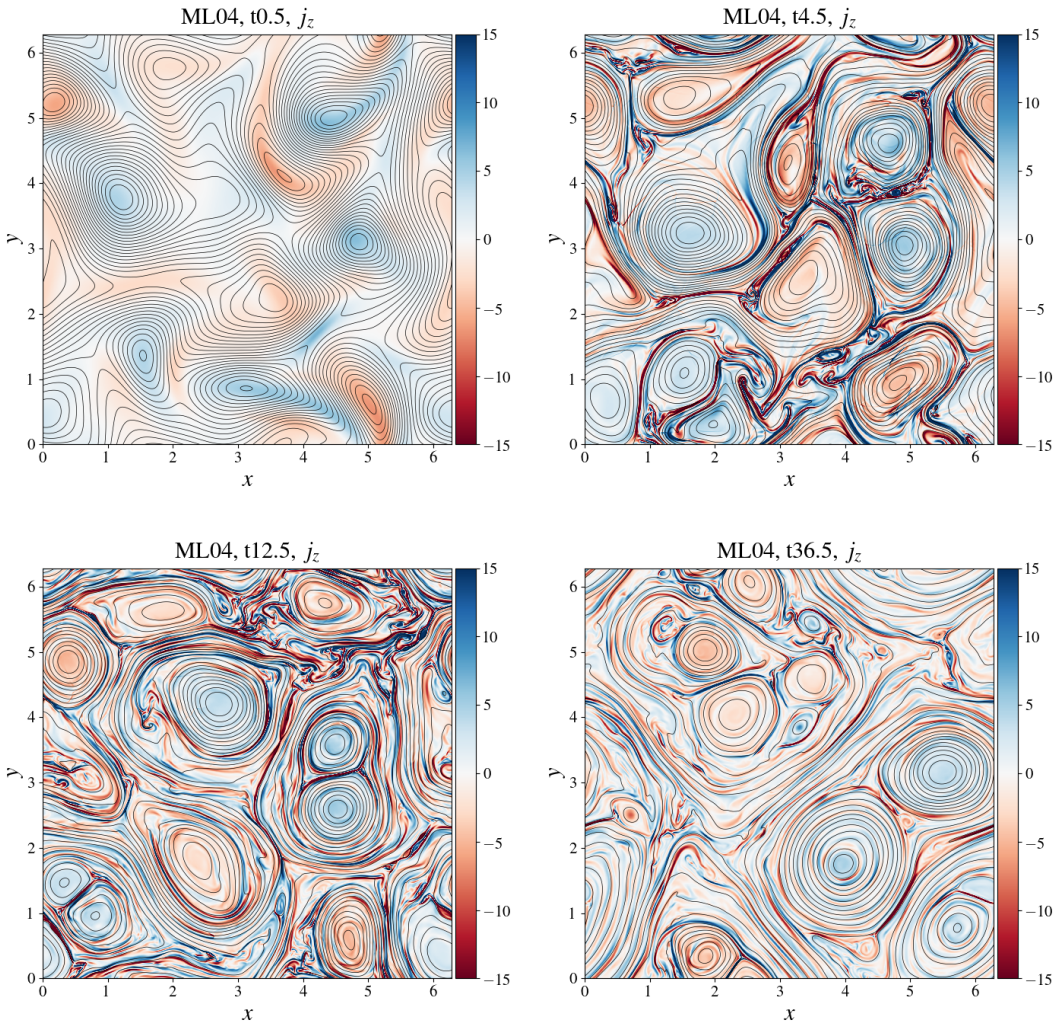


Figure 3.6: Current density (color shading) in the out-of-plane direction along with the vector potential (iso-contours) for ML04 simulation. The time sequence evidences the evolution of turbulence and the generation of strong current sheets in between magnetic islands.

correlated to the presence of magnetic islands, we use an independently developed method to test the technique. In Fig. 3.8, we report, as shaded areas, magnetic flux tubes and reconnecting current sheets that were identified using a cellular automaton (CA) procedure described in Servidio, Greco, et al. (2011). This CA was built on the topological properties of the magnetic potential. First, it identifies the critical points (maxima, minima, and X-points), and then propagates information away from these critical points, thus identifying the strongest, large-scale islands (starting from the O-points) and the reconnection regions (starting

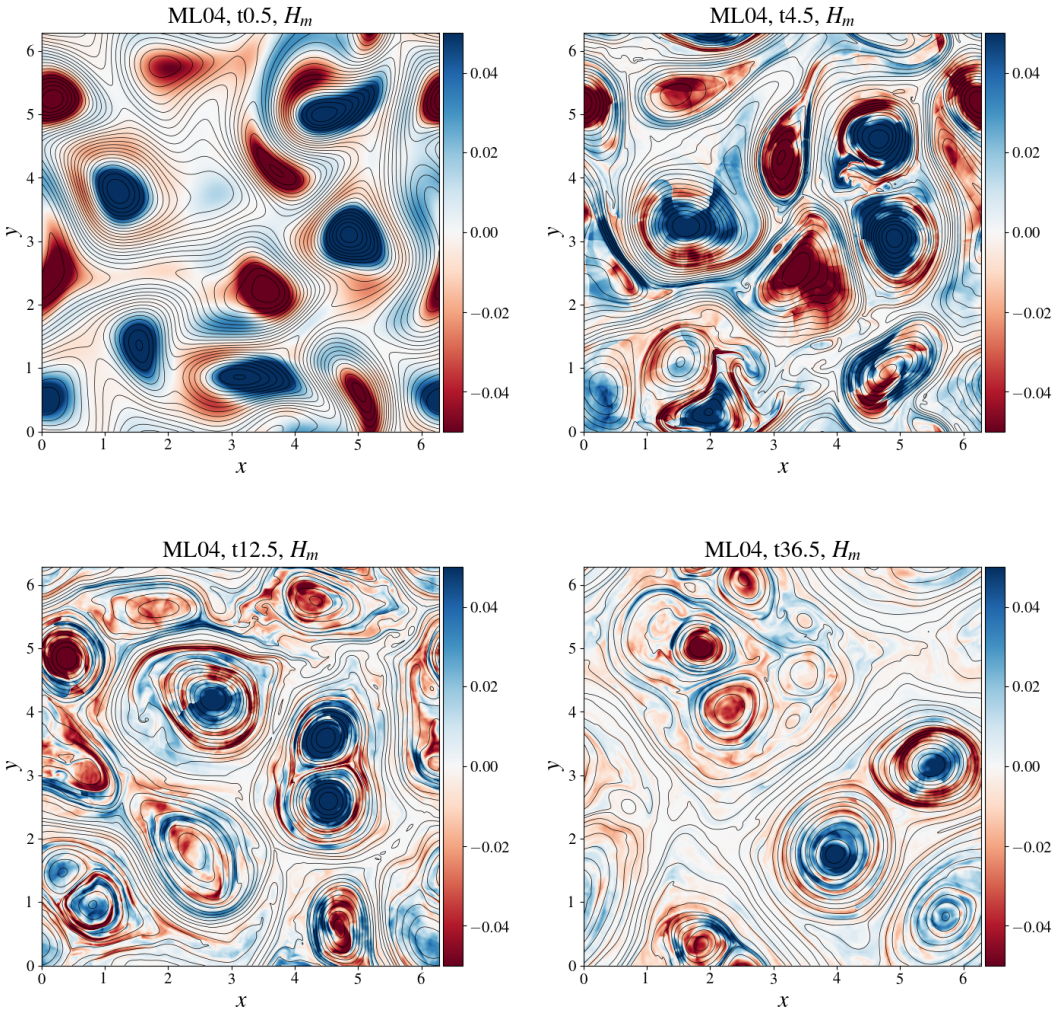


Figure 3.7: Magnetic helicity (color shading) along with the vector potential (isocontours) for ML04 simulation. The time sequence evidences that $H_m$ is concentrated and maintained within magnetic islands.

from the X-points). The result of this procedure is a cellularization of turbulence (Matthaeus et al., 2015), as it is clear from the figure.

On this magnetic skeleton, we tested our 1D algorithm, based on the combination of the local magnetic helicity in Eqs. 3.38–3.39 and the PVI in Eq. 2.41. In order to test the method and to establish a direct comparison between plasma simulations and the PSP data, we sent a virtual spacecraft through the periodic domain. Its trajectory is represented in Fig. 3.8 with oblique blue lines, which intersects both large-scale helical structures (cyan) and small-scale discontinuities (orange).

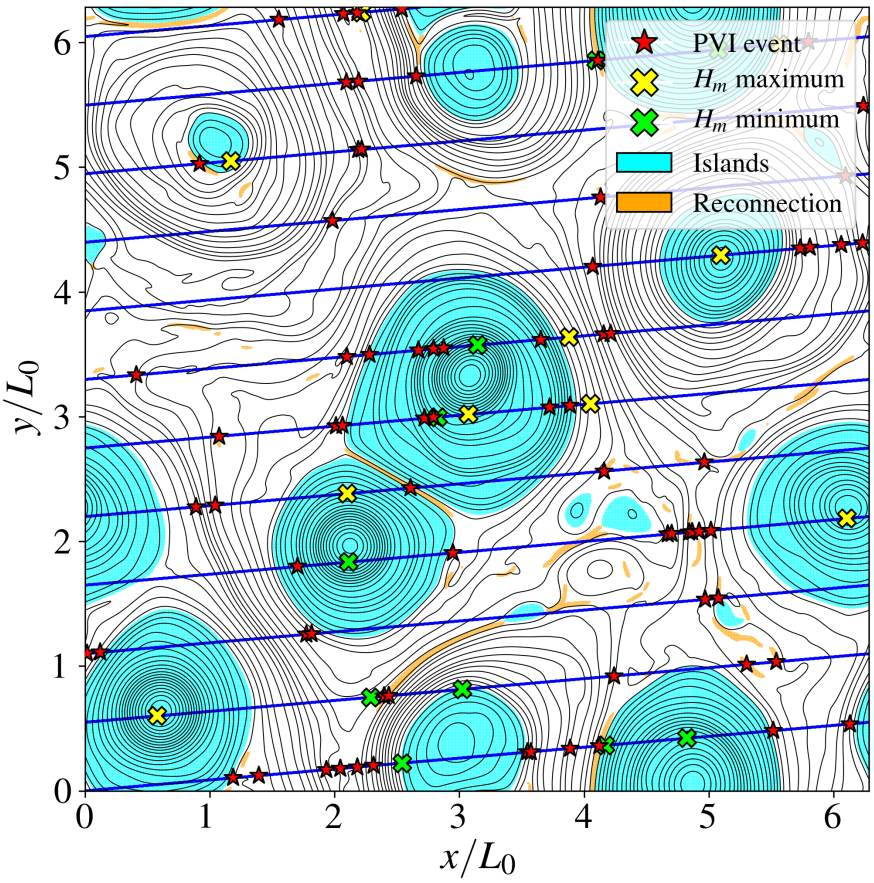


Figure 3.8: 2D line contours of the magnetic potential $a$ (black solid) at the maximum of the turbulent activity of the analyzed MHD simulation. The shaded areas in cyan and orange are magnetic islands and strong current sheets, respectively, individuated by the CA algorithm. The oblique blue lines represent the trajectory of a virtual satellite that sweeps through turbulence. Yellow and green crosses indicate the maxima and minima of the local magnetic helicity, respectively, while red stars are strong PVI events. From Pecora et al. (2020).

In Fig. 3.9–(a), we report the turbulent magnetic field, as observed along the virtual satellite trajectory. The 1D signals are shown over the entire trajectory along the oblique coordinate $s$ measured in units of $L_0$. In (b) we show the out-of-plane current $j_z$ which is very intermittent, indicating the presence of magnetic discontinuities. To identify these intermittent spots using the magnetic field (that has to be interpolated from grid points to the oblique trajectory), we computed the PVI signal, as described in Eq. 2.41. We used very small increment lags, namely $\mathrm{PVI}(s, \ell = \lambda_T/10)$, where $\lambda_T = \sqrt{\delta b^2_{rms}/j^2_{rms}}$ is the magnetic Taylor microscale (already mentioned in Sec. 2.7.2). At these lengths, the time series generated

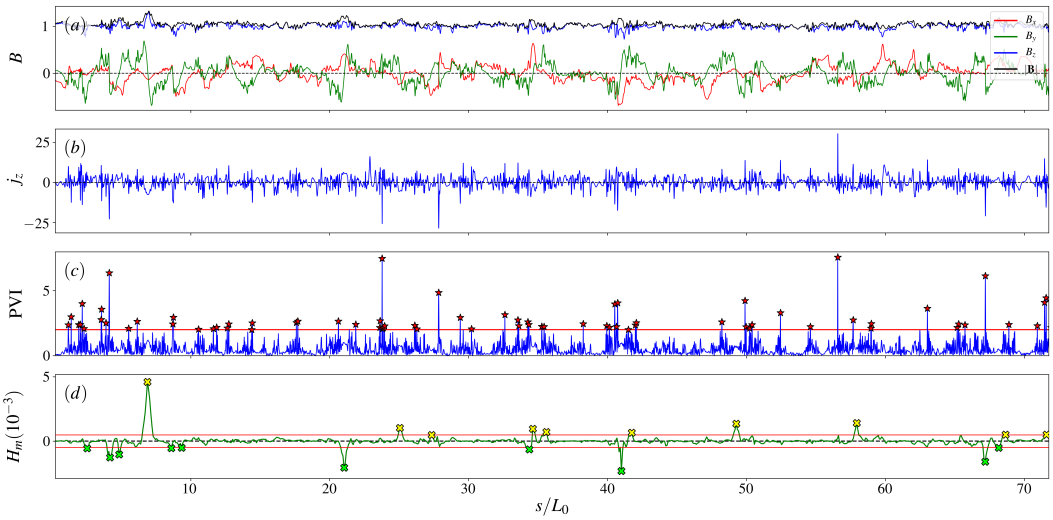


Figure 3.9: Measurements and analyses along the virtual spacecraft trajectory shown in Fig. 3.8. (a) Magnetic field components and magnitude. (b) Current density $j_z$ in the out-of-plane direction. (c) Time series of PVI$(s, \ell = \lambda_T/10)$. (d) Filtered magnetic helicity evaluated at a correlation scale $H_m\left(s, \ell = \frac{\lambda_c}{2}\right)$. The horizontal red lines in (c) and (d) represent the thresholds of the method, and the symbols represent over-threshold peaks. From Pecora et al. (2020).

by the PVI method becomes a good surrogate for the current density, as is suggested by comparing panel (b) and panel (c) of the same figure (for more on this comparison, see Greco et al. (2018)).

To complete the analysis, we computed the filtered magnetic helicity in Eqs. 3.38–3.39. First, we rotated the magnetic field $\boldsymbol{b}$ from the Cartesian $(b_x, b_y, b_z)$ frame to the trajectory coordinates $(b_1, b_2, b_3)$, where $b_1$ is the component along the trajectory direction $\hat{\boldsymbol{e}}$, $b_3$ remains along $z$, and $b_2$ completes the right-handed frame. Second, from this rotated field, we computed the $H_m$ signal at the (cumulative) scale $\ell = \lambda_c/2$, where $\lambda_c$ is the correlation length described in Sec. 2.3.

By using both the surrogate $H_m$ measurement and the PVI signals, we established a threshold-based method in order to identify the most significant events. For the $H_m$, we identified as strong flux tubes the events with helicity values larger than one standard deviation of the $H_m$ distribution. For the PVI method, we chose a typical threshold of PVI = 2. It has been shown that the probability distribution of the PVI statistic derived from a non-Gaussian turbulent signal strongly deviates from the probability density function of the PVI computed from a Gaussian signal for values of PVI that are greater than about 2. As PVI increases, the recorded "events" are extremely likely to be associated with coherent

structures and therefore inconsistent with a signal having random phases (Greco et al., 2018).

The selected peaks are reported for both $H_m$ and PVI in panel (c) and (d) of Fig. 3.9, respectively. At this point, we have a list of events, namely the position of the possible flux ropes (peaks of the filtered magnetic helicity signal) and the reconnection events (peaks of the PVI signal). The position of these events is reported over the full 2D map in Fig. 3.8, and one may observe a very good qualitative agreement of these events with the magnetic potential and the CA painting. Magnetic helicity peaks are located well inside helical islands, close to their cores. A few are located outside and coincide with PVI events, indicating the presence of complex structures in between islands, which is possibly due to a reconnection-induced reorganization of magnetic field topology. On the other hand, red stars – the PVI events – are found at the boundaries of magnetic islands. This precise positioning of magnetic helicity and PVI peaks suggests that the core of a magnetic island can be identified, with noteworthy precision, by a magnetic helicity extremum, and its boundaries coincide well with the closest PVI events on either side. The new method is therefore able to identify the strongest helical flux tubes and the more intermittent magnetic structures, which are likely to be reconnection events.

Fig. 3.10 shows a close-up of the relevant quantities measured along the first segment of the synthetic trajectory. From this 1D information, the identification of magnetic islands is rather straightforward: the oscillations of the PVI signal tend to drop in magnitude near a local extremum of $H_m$, and the boundaries of the islands are well-defined by a sharp increase in PVI. Moreover, inside island cores, it is evident that the total current is smaller in general, but not zero, in view of Ampere's law. The net magnetic helicity in a flux rope is indicated by a nonzero component of the out-of-plane magnetic field fluctuation $b_z$. It is interesting to notice how well the $H_m$ peaks fall in a PVI-quiet region in between two strong PVI events.

### 3.5.3 Identification in Parker Solar Probe data set

We applied the $H_m$–PVI technique to magnetic field measurements obtained from the Fluxgate Magnetometer on the PSP FIELDS instrument suite (Bale et al., 2016). In particular, we analyzed the results obtained from the first perihelion (Bale et al., 2019), which will be further discussed in comparison with other iden-

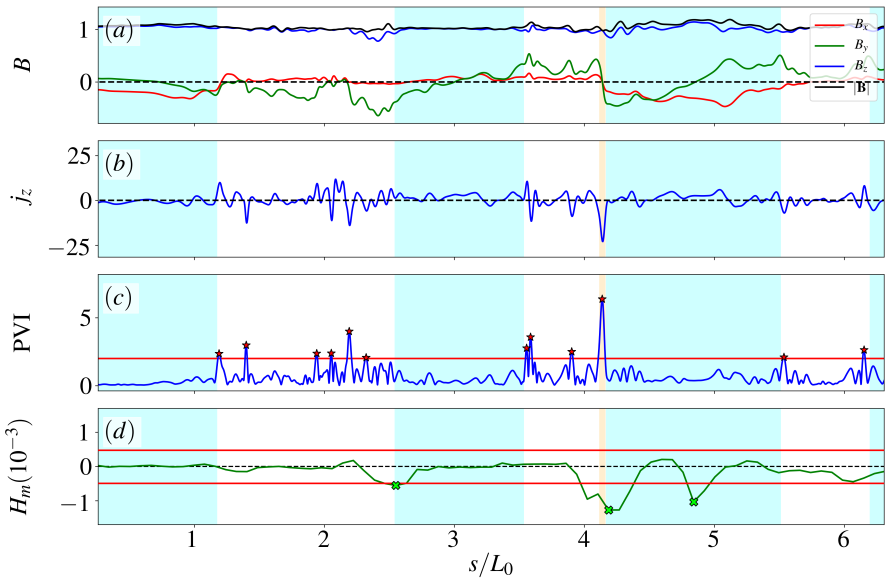


Figure 3.10: Zoom on (a) magnetic field, (b) current density, (c) PVI, and (d) $H_m$ for the first segment of the trajectory, where three peaks of helicity and twelve PVI events have been identified. Shaded cyan and orange areas represent the CA structures reported in Fig. 3.8. The $H_m$ peaks fall in PVI-quiet regions, in between consecutive, strong PVI clusters. From Pecora et al. (2020).

tification techniques (Zhao et al., 2020; Y. Chen et al., 2020). The FIELDS magnetic data were resampled from full resolution to 1-second cadence. Moreover, the first encounter data were divided into 8-hour-long subsets, so that each contains several correlation times. The correlation time $\tau_c$, in the spacecraft frame, is about $10 - 40$ minutes at radial distances of $0.17 - 0.25$ au (Parashar et al., 2020).

The correlation time, which will also be used in the following, is intended to only provide a rough estimate of local large-scale structure duration. The large uncertainties that affect the determination of the correlation time are still an open issue and prevent the application to rigorous treatments (Krishna Jagarlamudi et al., 2019).

We analyzed several such intervals in the first encounter; however, to make close contact with the above-mentioned published works (Zhao et al., 2020; Y. Chen et al., 2020), we concentrate below on the following particular interval: 2018 November 13 from 8:00 to 16:00 UTC. Figure 3.11 shows (a) the magnetic field time series in the RTN coordinate system, (b) the PVI computed at 1s lag, and (c) the magnetic helicity evaluated at the scale of one correlation time. In this interval, the average plasma $\beta \sim 1$ (Chhiber, Goldstein, et al., 2020; Zhao et al.,

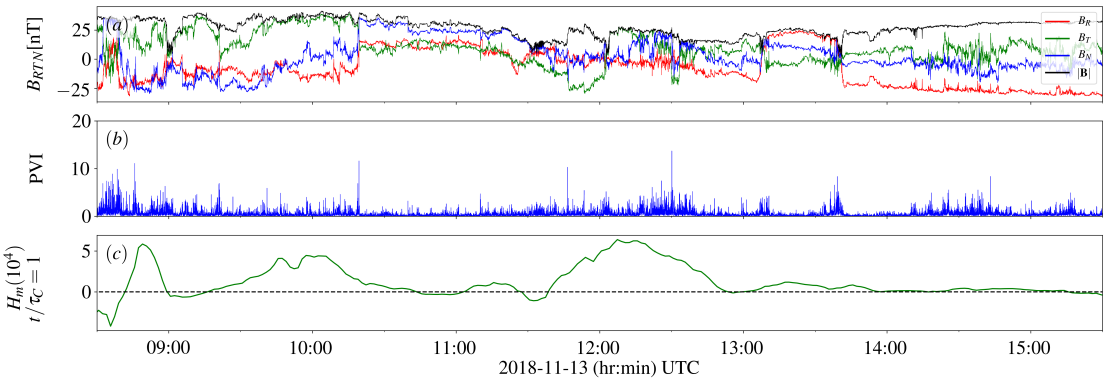


Figure 3.11: (a) PSP FIELDS Fluxgate Magnetometer (MAG) data in RTN coordinates resampled at 1s on 2018 November 13 from 8:30 to 15:30 UTC. In this interval, the correlation time $\tau_c \sim 25$ minutes. (b) PVI signal and (c) $H_m$ computed at one correlation time. From Pecora et al. (2020).

2020; Y. Chen et al., 2020).

Figure 3.12 shows the analysis of two subintervals of the data shown in Fig. 3.11, specifically from 9:15 to 12:45 (left panels) and from 13:00 to 13:45 (right panels). Each column shows stacked plots of the magnetic field time series, PVI, and local magnetic helicity, which was computed with different maximum lags. The spatial increment used in the definition of Eq. 2.28 can be converted in temporal increments using the Taylor hypothesis – for which time evolution of structures can be neglected as they sweep through the satellite –, one can revert back the temporal lag to spatial lag using the average solar wind speed in the considered interval, namely $\ell = V_{sw}\tau$. The largest lag was chosen to be one correlation time $\tau_c$, while the smallest was $t/\tau_c = 1/3$. Regions of high helicity are shaded in cyan, while nearby PVI events in orange, in analogy with the procedure employed in the simulation. Pairs of PVI events that bound helical regions are also highlighted with dashed vertical lines. It is evident that the $H_m$ time series suggest a multi-scale nature of helical structures. We recall that the helicity diagnostic incorporates contributions from all scales smaller than the maximum lag.

The left panels of Fig. 3.12 show two helical structures that are bounded by two strong PVI events each (cyan lines for the first event and magenta lines for the second). At scales smaller than one correlation time (panels (d) and (e)), the $H_m$ signal shows a fragmentation of the structures, highlighting smaller features within the larger helical structure. Moreover, the two identified cores (cyan shaded regions) might be enclosed within a larger helical structure, possibly bounded by

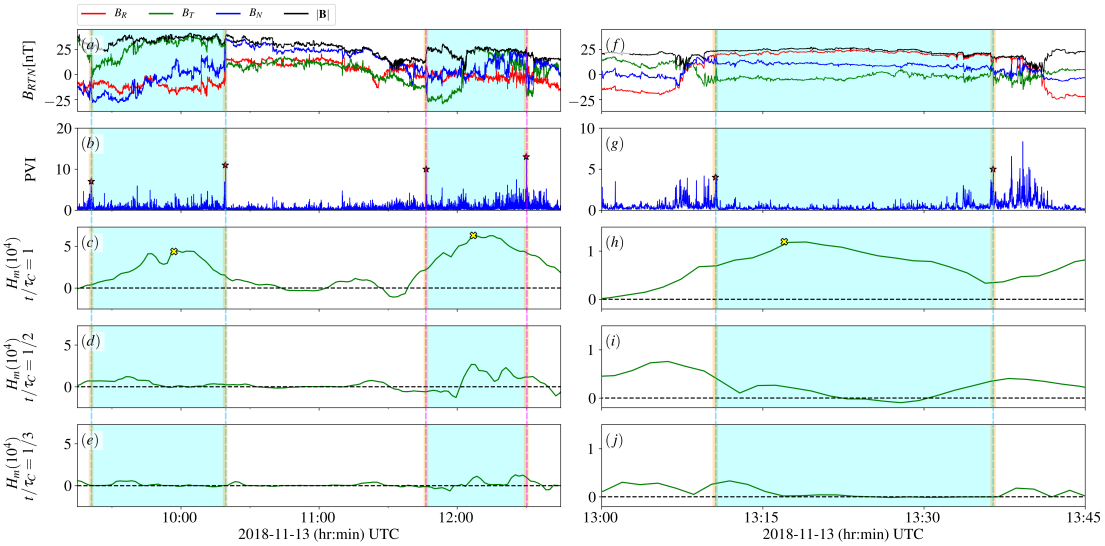


Figure 3.12: Two close-ups of Fig. 3.11 (left panels) from 9:15 to 12:45 and (right panels) from 13:00 to 13:45. The figure reports the magnetic field (a) and (f); the PVI signal (b) and (g); and the magnetic helicity evaluated at one correlation time (c), (h), 1/2 correlation time (d), (i), and 1/3 of the correlation time (e) and (j). It is interesting to notice that the $H_m$ shape heavily depends on the chosen window, suggesting a multi-scale nature of helical structures. The vertical cyan and magenta lines highlight the position of strong PVI events edging high-helicity regions (cyan shaded regions). The left panels show two structures that are bounded by two strong PVI events each (cyan lines for the first event and magenta lines for the second). At scales smaller than one correlation time, the $H_m$ signal shows a fragmentation of the structure, highlighting sub-features within the helical structure. Moreover, the two identified cores might be enclosed within a larger helical structure, possibly bounded by the leftmost cyan and rightmost magenta lines. This description is also consistent with the GS reconstruction performed in Y. Chen et al. (2020) (their Fig. 4), which shows a large island with two inner structures. The right panels, instead, show a smaller structure at $t/\tau_c = 1$, clearly bounded by PVI events, which has no internal features. From Pecora et al. (2020).

the leftmost cyan and rightmost magenta lines. This description is also consistent with the GS reconstruction performed in Y. Chen et al. (2020), which shows a large island with two inner structures at about the same period. The right panels, instead, show a single structure at $t/\tau_c = 1$, which is clearly bounded by PVI events (panel (h)). At smaller scales, $t/\tau_c = 1/2$ (panel (i)), $t/\tau_c = 1/3$ (panel (j)), and the $H_m$ signals suggest the absence of relevant internal structures, envisioning a "pristine" flux rope.

We have found that flux tubes, identified in several independent ways in sim-

ulations, have a precise pattern of the $H_m$–PVI signals. The same patterns have been recovered in the application to the PSP measurements, confirming that the $H_m$–PVI method can be a reliable tool for the detection of such structures. In the following Section, we present an ongoing work for the development of an algorithm that automatically detects flux tubes with the above $H_m$–PVI technique, and performs local GS reconstructions.

### 3.5.4 GS solver with $H_m$ support in MHD simulations

In this Section, we will show the application of our novel GS solver to the simulations of MHD turbulence described in Sec. 3.5.2. The preliminary results shown here are of great interest since, as far as we know, it is the first time a GS solver is applied to numerical simulations of plasma turbulence. Simulations grant the unique opportunity for visual comparison and analytical estimation of the error in the reconstruction. Our GS solver was enhanced by adding a first automatic detection step based on the helical properties of flux tubes shown in previous Sections. Each reconstruction is also performed automatically and guided by physical parameters. Given a 1D trajectory in the simulation, $H_m$ extrema are individuated as described previously. In Fig. 3.13 we show the magnetic potential $a_z$ (dashed black lines) that outlines magnetic structures. The virtual trajectory along which the analysis is performed is the oblique line, and the over-threshold magnetic helicity extrema are also indicated. The reported values of magnetic field components along the virtual satellite path show the typical behavior of flux ropes, with the rotation of one component and an enhancement of magnetic field magnitude. Also, the current density becomes smoother as large gradients are expected to take place mostly at the boundaries of the flux tubes (recall that the PVI is a good surrogate of the current).

After the identification of the potential flux tube cores (as over-threshold $H_m$ extrema), the algorithm passes to the GS solver an interval of measurements that extends for one correlation length and is centered about each local $H_m$ extremum. Recall that the correlation length is about the typical size of magnetic islands (in these simulations $\lambda_c \sim 0.5$). For each of these sets, the algorithm performs the steps described in Sec. 3.3. Figure 3.14 shows the relevant quantities in the final optimal reconstruction frame $(\hat{x}, \hat{y}, \hat{z})$. The magnetic field component show the typical features of flux tubes, with one that is small and almost constant, one that flips sign and the latter that is bell-shaped (Sonnerup & Guo, 1996; Hau &

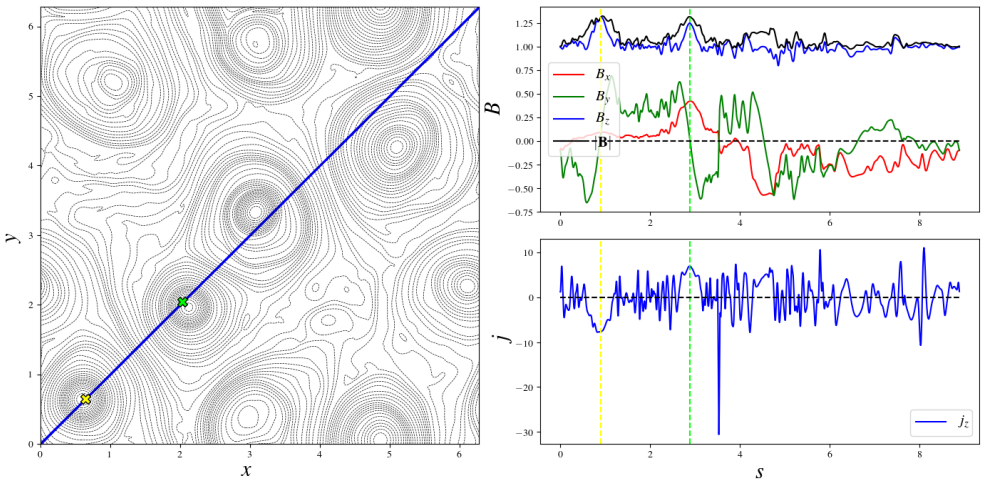


Figure 3.13: (Left) Magnetic potential iso-contours (black dashed lines) for ML02 simulation (for details refer to Table 3.1). The blue oblique line is the virtual satellite trajectory. Over-threshold magnetic helicity extrema are indicated with yellow (positive) and green (negative) cross marks. (Top right) Magnetic field components and (bottom right) current density measured along the trajectory direction $s$. The vertical yellow and green dashed lines mark the position of the corresponding $H_m$ extrema.

Sonnerup, 1999). The transverse pressure has a maximum at the center of the island, and the magnetic potential is a symmetric parabola. The requirement for GS equilibrium that the pressure is a function of the vector potential alone is well respected. The values of $P_t(A)$ are very well overlapping between the two branches (the two halves of the island) and a numerical fit returns the analytical exponential form of this correlation. Notice that only the first and the last point of this scatter plot are considered non-overlapping by the algorithm.

Once the analytical form of $P_t(A)$ is obtained, the rhs of GS equation is completely determined and the reconstruction in the perpendicular direction can be performed. The "local" plane in which reconstruction is performed is indicated as $x_{rec} - y_{rec}$. As mentioned before, once a peak of magnetic helicity has been individuated, the length of the $x_{rec}$ axis is set to be one correlation length (of the magnetic field), centered at the peak. Along this direction, original data is re-sampled at a cadence of $\lambda_T/2$, where $\lambda_T$ is the in-plane magnetic field Taylor length and for these simulations is $\lambda_T \sim 0.05 \sim \lambda_c/10$. The reconstruction step in the perpendicular direction, $y_{rec}$, is also a fraction of the Taylor length (in particular, it is chosen $\Delta y = \lambda_T/10$). Numerical simulations allow to estimate the

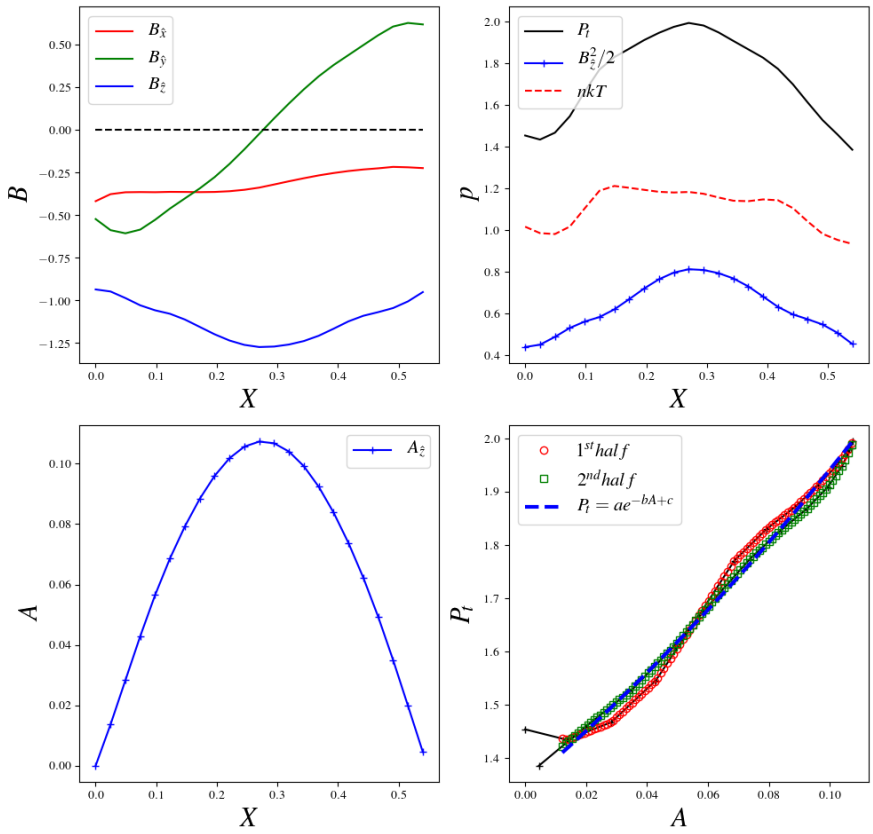


Figure 3.14: Quantities in the reconstruction optimal frame. (Top left) Magnetic field components. The component along the projected satellite path is close to zero, that in the perpendicular direction shows a smooth rotation, and the third indicates the presence of a strong mean field. (Top right) kinetic (red dashed), magnetic (blue crossed) and transverse (black) pressures. (Bottom left) magnetic potential along the projected satellite trajectory; the peak identifies the center of the island. (Bottom right) the double folding of the pressure in the two branches of the island that are almost perfectly overlapping. A fit is performed through an exponential function so to have the complete rhs of the GS equation.

deviation of the reconstructed field from the exact ones, and we defined an error as

$$\epsilon = \sqrt{\frac{|A_{rec} - A_{ex}|^2}{N_x\ N_y}}, \tag{3.44}$$

where $A_{rec} - A_{ex}$ is the point-wise (on the numerical grid) difference between the reconstructed and exact vector potential, over the reconstructed domain composed of $N_x \times N_y$ points. Figure 3.15 shows $\epsilon$ as a function of the increasing number of

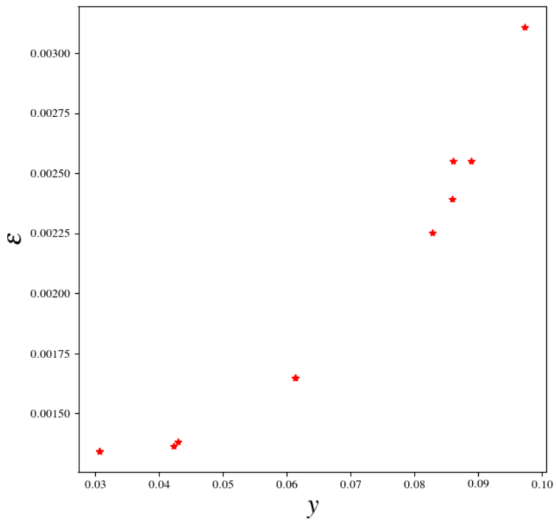


Figure 3.15: Deviation of reconstructed vector potential from the exact one. The error grows exponentially as a function of the increasing extension of the reconstruction domain.

$N_y$ points used for the reconstruction. As expected, the farther the reconstruction is performed, the larger the deviation from the exact values.

The optimal extent of the reconstruction in the perpendicular direction is then inferred through physical quantities rather than imposed numerically. At each step of reconstruction away from $y_{rec} = 0$ line, a sort of Taylor length for the magnetic potential is calculated as:

$$\lambda_T(A) = \sqrt{\frac{\langle |A - \langle A \rangle|^2 \rangle}{\langle |\partial A/\partial x|^2 \rangle}}, \tag{3.45}$$

where the averages $\langle \dots \rangle$ are taken over the horizontal axis, at the current $y$ position, and $A$ is the reconstructed vector potential. The meaning of this length can be described as follows: while the reconstruction algorithm spans regions farther away from satellite trajectory ($y_{rec} = 0$), spurious scales are formed. As soon as this length keeps growing, the smallest describes scale is growing too, so no additional fictitious information is added. When this length starts decreasing, scales smaller than the previous ones are created, so non-physical information is added in the reconstruction and the algorithm can stop. Figure 3.16 shows this procedure at work.

The panel on the left shows the Taylor length for the vector potential as a function of the increasing reconstruction position in the upward direction (at this

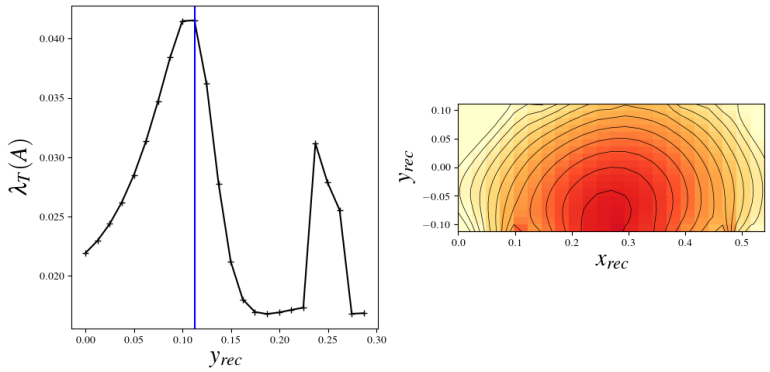


Figure 3.16: (Left) Vector potential Taylor length as a function of the increasing distance of reconstruction. The vertical blue line indicates the position where numerical spurious glitches start to appear. (Right) Reconstruction domain (color shading is vector potential magnitude) cropped at the so-determined $y$-position.

point it is assumed to be symmetric in both directions, but it is possible to measure different $\lambda_T(A)$ for both the upward and downward directions). As stated above, this length increases up to a certain position and then starts decreasing when numerical instabilities start to grow and add nonphysical information at smaller scales. The vertical blue lines indicates the maximum extension in the $y$ direction determined by the algorithm. On the right, the domain of a reconstructed island, cropped at the distance where $\lambda_T(A)$ starts decreasing. Using a non-symmetric domain would prevent the appearance of the small glitches that are present, in this case, at far negative $y_{rec}$ values. As one would expect, when the starting sampling line is closer to the island center, the reconstruction domain can be extended farther away. The more the island is sampled close to the edges, the sooner numerical glitches appear resulting in a reduced reconstructed domain as Fig. 3.17 shows.

Figure 3.17 also suggests a possible application to multi-spacecraft mission as a synergistic work between any spacecraft close (or distant) enough. In fact, if a flux tube sweeps through different spacecraft at different positions, a reconstruction can be performed with the measurements taken at each of them. The final result can be a larger reconstructed domain composed of the overlapping single ones. Also, fields magnitudes obtained by reconstruction at one satellite can be compared to the values measured by the others confirming the "goodness" of the result (e.g. Möstl et al. (2009)). Finally, Fig. 3.18 shows the consecutive reconstructions performed in the simulation along the oblique line.

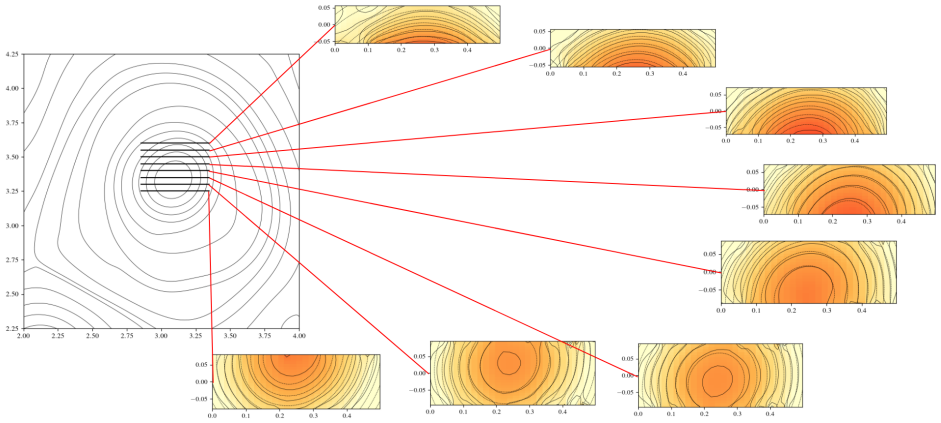

Figure 3.17: Reconstructions performed starting from different trajectories. The reconstruction domain can expand farther when the sampling trajectory is closer to the island center. In the reconstructed domains are reported simulation (dashed) and reconstructed (solid) vector potential, along with its magnitude (color shading). The figure also suggests that application to multi-spacecraft mission is possible in order to expand the total reconstructed domain by overlapping different local reconstructions.

This automatic detection-reconstruction algorithm shows promising results even in its not yet final version. Also, using physical constraint rather than numerical parameters lets the algorithm adaptively adjust to obtain the best possible reconstruction based on local properties. In the following, we present another application of the $H_m$–PVI technique on the PSP orbit 5 data.

## 3.6 Flux tubes and energetic particles

In this last Section, using the $H_m-$PVI technique described in Sec. 3.5.1, we show an ongoing work that gives observational evidence about the influence of helical flux tubes on the modulation of energetic particle populations. Energetic particle transport in the interplanetary medium is known to be affected by magnetic structures. This has been demonstrated in various near-Earth orbit studies for solar energetic particles (SEPs) (Klein, K.-L. et al., 2008; Trenchi et al., 2013), as well as for more energetic galactic cosmic rays, whose modulation depends on solar activity (Van Allen, 2000). A variety of indications, both theoretical (Ambrosiano et al., 1988; Drake et al., 2006; Dalena et al., 2012) and observational (Mazur et al., 2000; J. Tessein et al., 2013; J. A. Tessein et al., 2016; Khabarova & Zank, 2017) build a case that interactions of particles with turbulence is structured and

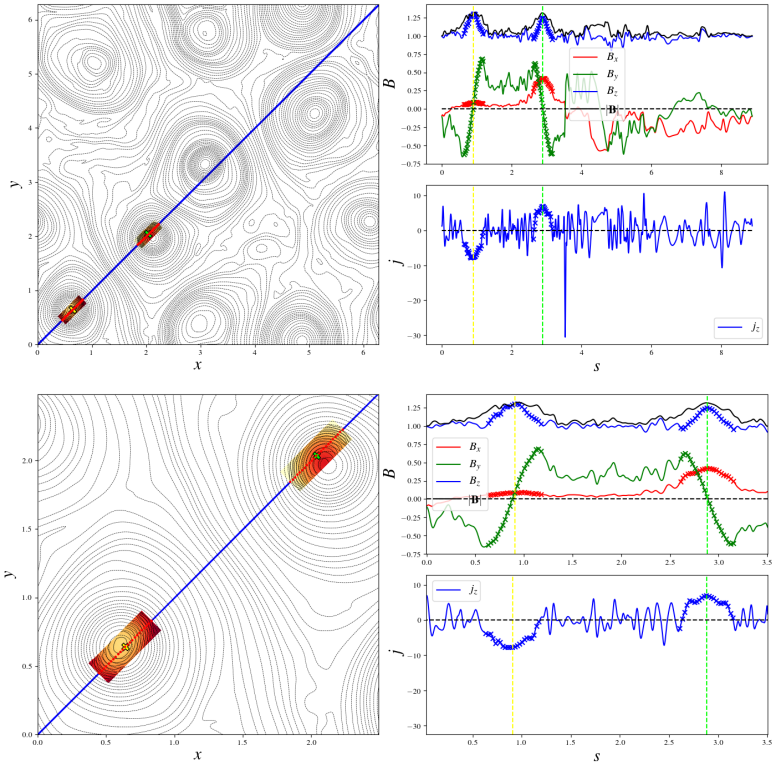

Figure 3.18: Consecutive automated reconstructions (color shaded regions) performed by the algorithm. The figure is organized in the same fashion as Fig. 3.13. The discrete marks on magnetic field and current density plots represent the resampled values used for the reconstructions.

inhomogeneous. These interactions may involve temporary trapping (Ruffolo et al., 2003), as well as exclusion from certain regions of space (Kittinaradorn et al., 2009), generally controlled by the topology and connectivity of the magnetic field. In some cases, such as SEPs "dropouts", the influence of the magnetic structure is dramatic (Mazur et al., 2000); in other cases, it is more subtle, as in edge effects in SEP confinement (J. A. Tessein et al., 2016; Khabarova et al., 2016). With PSP now closer to the Sun that any previous mission, novel opportunities are available for examining the relationship between magnetic flux structures and energetic particle populations. In particular, IS⊙IS energetic particle (EP) (McComas et al., 2016) along with FIELDS magnetic field (Bale et al., 2016), and SWEAP plasma moments (Kasper et al., 2016) measurements, are enabling the characterization of EPs observations closer to their sources than ever before possible.

During PSP orbit 5, from 2020 May 23rd to 2020 June 3rd, a sequence of five energetic particle events have been measured and have been the subject of several

studies (Cohen et al., 2020; Chhiber, Matthaeus, et al., 2020). We analyzed selected properties of these events using several PSP data products. We employ magnetic field data from the MAG instrument on the FIELDS suite, resampled from the original 4 samples per cycle (4Hz) to a 1-second resolution. PVI is calculated at this scale. Magnetic helicity is calculated using Eq. 3.39 – replacing spatial lag with temporal lag –, at different window sizes scaled to multiples of the correlation time $\tau_c$. Its normalized version is $\tilde{H}_m = H_m/(\langle \delta b^2 \rangle \tau_c)$, where $\langle \delta b^2 \rangle$ is the rms fluctuating energy in the considered interval. Particle measurements are obtained from the IS⊙IS EPI-Lo and EPI-Hi instruments. The IS⊙IS instruments EPI-Lo and EPI-Hi measure ions in energy ranges 20 keV/nucleon – 15 MeV total energy, and 1 – 100 MeV/nucleon respectively. Electrons are measured in the interval 25 keV – 1 MeV for EPI-Lo, and 0.5 – 6 MeV for EPI-Hi. We use EPI-Lo ChanP and ChanE for proton and electron count rates. For EPI-Hi we show the end A of both the High Energy Telescope (HET A), and the Low Energy Telescope 1 (LET1 A). All public data are available from the IS⊙IS database and on Coordinated Data Analysis Web (CDAWeb). Priority buffer (PBUF) rates measurements are not public as they are uncalibrated (engineering) data. These are integrated counts measured at different stopping depths within the telescope and cannot be calibrated to fluxes. In the following, we do not intend to use these measurements to obtain quantitative estimates, rather they are used to show a more resolved envelop of the hourly-averaged fluxes ( panels (j) and (k) of the following Figures).

An overview of the five events occurring during the selected period is shown in Fig. 3.19. Even at this scale of 11 days, the sets of measurements show interesting behavior and a correlation between energetic particles (both protons and electrons) and magnetic field helical properties. In particular, it is possible to notice that the large helical structure appearing around May 28th encloses both the energetic electrons (panels (g) and (i)), and the higher-energy portion of the energetic proton population (panels (f) and (k)). On the other hand, the lower-energy portion of the energetic proton population is less confined and more dispersed (panels (e) and (j)). We will focus on the first three events – identifiable with the sudden onsets (before May 29th) of energetic fluxes in panels (j) of Fig. 3.19.

Figure 3.20 shows the same quantities of Fig. 3.19, but the analysis is performed over the restricted time interval from May 24th 00:30 to 23:30 UTC during which $\tau_c \sim 38$ minutes. The restriction to a shorter time-scale enhances the smaller-scale

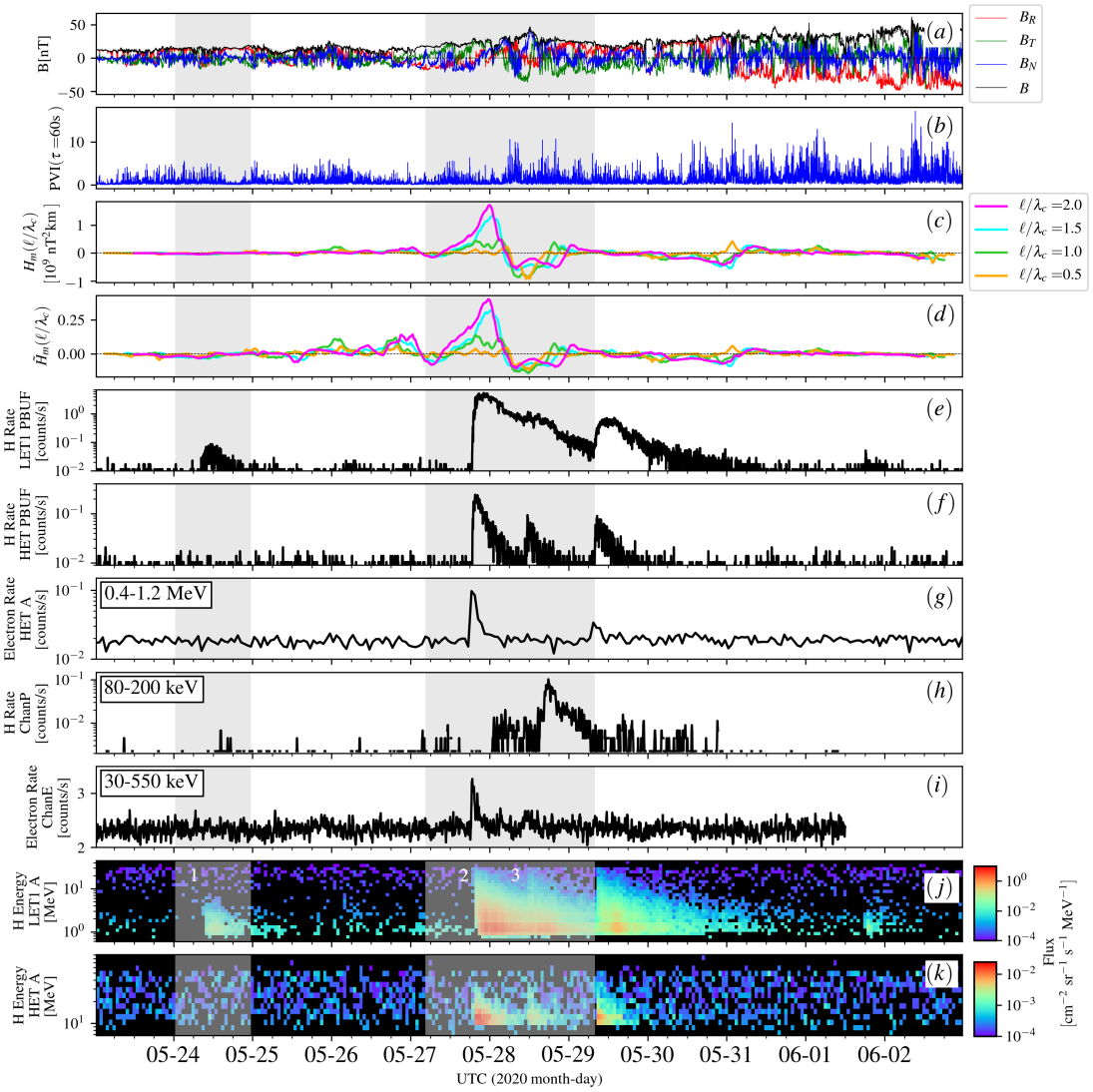


Figure 3.19: Period from 2020 May 24th, to June 2nd, during which $\tau_c \sim 6$ hours. The stacked panels show (a) magnetic field measured by FIELDS resampled at 1-second cadence, (b) the PVI signal computed with a time lag of 60 seconds, (c) the magnetic helicity of fluctuations, and (d) its normalized version, (e) EPI-Hi LET1 proton count rate at 60-second resolution, (f) EPI-Hi HET proton count rate at 60-second resolution, (g) EPI-Hi HET A electron count rate in the energy range 0.4-1.2 MeV at 1-hour resolution, (h) EPI-Lo proton count rate in the energy range 80-200 keV at 300-second resolution, (i) EPI-Lo electron count rate in the energy range 30-550 keV at 300-second resolution, (j) EPI-Hi LET1 A proton flux at 1-hour resolution, and (k) EPI-Hi HET A proton flux at 1-hour resolution.

helical structures that were obscured before. In this case, the energetic proton population appearing from 9:00 to 15:00 is confined between – and excluded from

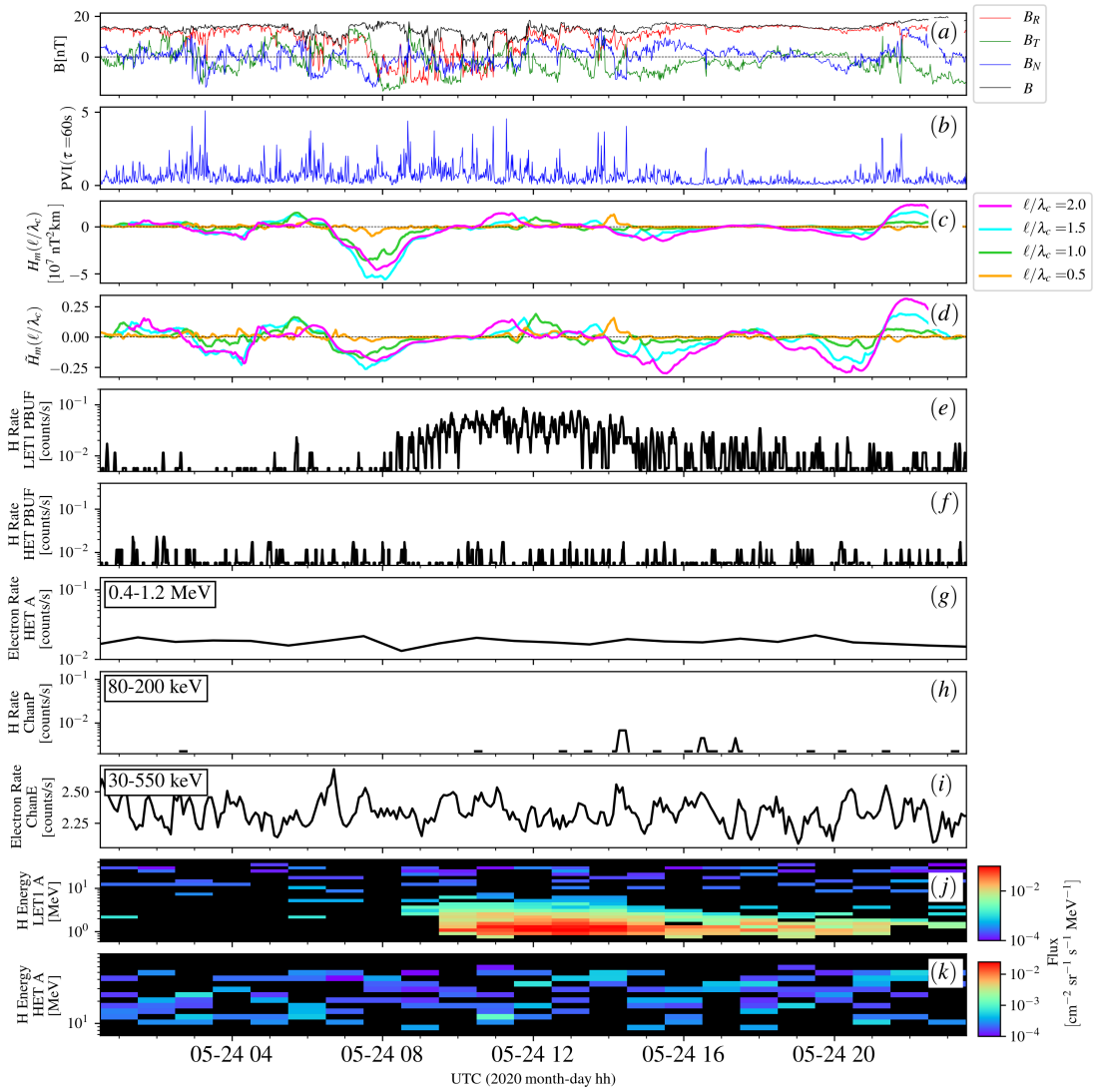


Figure 3.20: 2020 May 24th from 00:30 to 23:30 UTC, $\tau_c \sim 38$ minutes. The panels are arranged in the same fashion as in Fig. 3.19. The energetic proton population is confined between and excluded from the two negative helicity peaks.

– the two helical structures. During this event, the helical field lines appear to act as excluding boundaries for the particles which have suppressed transport across the structures. We may imagine this population to be squeezed and advected between these flux ropes. This kind of exclusionary behavior is reminiscent of the phenomenon of SEP *dropouts* that have been associated with topological strictures, and that are frequently observed at 1 au and in simulations (Mazur et al., 2000; Ruffolo et al., 2003; Tooprakai et al., 2016). The exclusion of the energetic protons from regions to the left of 08:00 is likely associated with the onset of the SEP event,

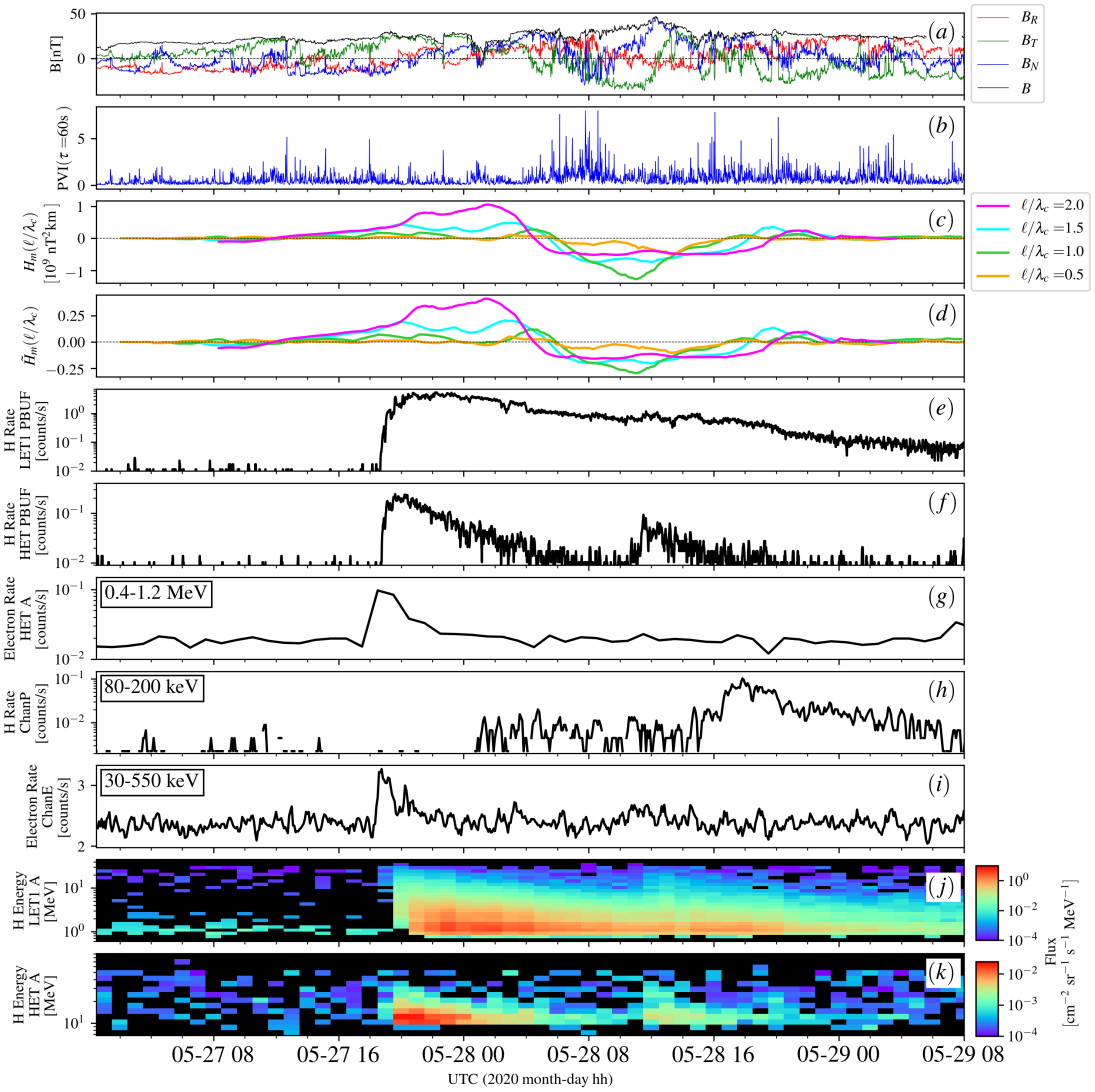


Figure 3.21: Period from 2020 May 27th 04:30 to 29th 08:00, during which $\tau_c \sim 4$ hours. The panels are arranged in the same fashion as in Fig. 3.19.

but could also possibly provide information about the flux tubes through which the earliest particles in the event are transported. The spreading of particles following onset is typically associated with diffusive transport (e.g., Dröge et al. (2016)). In this case the helical structure near 16:00 may be inhibiting diffusion into the relatively quiet region (in terms of PVI) that resides between the helical structures at 16:00 and 22:00. Phenomena such as this have been observed in simulations and have been interpreted as temporary topological trapping (Tooprakai et al., 2016) possibly accompanied by suppressed diffusive transport (Chuychai et al., 2005).

The picture given by Fig. 3.21 examines an approximately 2-day period be-

ginning on 2020 May 27th, and is complementary to the one of Fig. 3.20. Events 3 and 4 shown here, can be better distinguished in the HET signal of EPI-Hi, in which two separated populations clearly appear. In LET1, the signal of the first event does not fully decline before the onset of the second one. This local analysis shows that there are two adjacent flux tubes of opposite-sign helicity. One can notice that the abrupt onset of EP coincides with the appearance of the flux tube, suggesting that the spacecraft has suddenly experienced a different environment, passing from the ambient solar wind to a confined plasma. In this case, contrary to the previous, each energetic population is confined within a different helical structure. The lower-energy counterparts (panels (h) and (i)) are not concentrated in the positive helicity flux rope between 05-27 16:00 and 05-28 04:00, nor in the negative-helicity flux rope between 05-28 04:00 and 05-28 20:00. Rather, one sees an enhancement of EPi-Lo 80–200 keV protons in association with the trailing edge of the negative-helicity flux tube.

The two different, but complementary, descriptions emerging from the events in Fig. 3.20 and Fig. 3.21 are not in contrast one another, rather they confirm the same vision. The analysis of the two periods suggests that helical flux tubes act as difficult-to-penetrate boundaries for particles in either directions. Particles that are outside have difficulty breaking into the region of helical field lines and populate the core of the flux rope. As in the moss model (Kittinaradorn et al., 2009), particles can impinge at flux rope boundaries and get energized by discontinuities and reconnection events. On the other hand, particles that are originally confined within the structure can experience coherent energization processes due to inner reconnection events or flux rope topological evolution (le Roux et al., 2015; le Roux et al., 2015; le Roux et al., 2018; Du et al., 2018).

We therefore find evidence for existence of transport boundaries at or near edges of solar energetic particle enhancements, where the boundaries are characterized by helical flux ropes accompanied at their edges by clusters of enhanced PVI events. This elaborates on previous findings near 1 au (J. A. Tessein et al., 2016) and indicates that the channeling of SEPs occurs closer to the Sun than has been previously observed.

# Discussion and conclusion

In the works done during this PhD, different problems of astrophysical plasmas have been investigated with different approaches. The synergistic use of theories, simulations, and observations granted a deeper understanding of the physical phenomena of interest.

In the first Chapter, we described and compared two of the most commonly used approaches for plasma physics simulations: (I) the hybrid and (II) the full kinetic PIC algorithms. We used three different values of the plasma $\beta$, in order to describe relevant scenarios for heliospheric plasmas: the solar atmosphere ($\beta \lesssim 0.1$), the outer regions such as the fast/slow solar wind ($\beta \simeq 1$), and the turbulent magnetosheath ($\beta \gg 1$). We used three HPIC simulations and performed several with the FPIC algorithm. With the latter, we investigated how different numerical parameters (with same physical conditions) affect the energy conservation and the spectral properties of turbulence. We found that, increasing the number of particles per cell gives better results, for what concerns energy conservation, than increasing the resolution (the number of cells used to discretize the computational domain). The power spectra of electric and magnetic fields are consistent with the Kolmogorov prediction in the inertial range $S(k) \sim k^{-5/3}$. The magnetic field spectrum exhibits a steeper power law at smaller (kinetic) scales, with a scaling $S(k) \sim k^{-8/3}$. The results were comparable within the two codes. Regarding the electric field, the differences between the two algorithms are more appreciable. At smaller scales ($kd_i > 1$), and at low $\beta$, the electric field spectrum of the full PIC simulation is larger than that of the corresponding hybrid simulation. This is probably due to the fact that in the full kinetic case, the electric field retains the contribution of small-scale effects, such as the electron pressure-divergence term.

In the second Chapter, we focused on the description of diffusion and acceleration of ions in plasma turbulence, using the above-mentioned self-consistent simulations. First, we have observed the motion of ions moving self-consistently

in the turbulent electromagnetic field, and found that it is very erratic. Particles can be trapped in magnetic vortices or scattered away by current sheets, wandering like a pollen in the atmosphere, or field lines in the solar corona (Rappazzo et al., 2017). We have then proved that this type of motion, achieved after long time intervals, can be described in the realm of the Brownian diffusion theory. Subsequently, a number of diffusion theories have been described in the search for an analytical form of the diffusion coefficient that is not provided by that of the Brownian motion. The investigated theories give a functional form of the diffusion coefficient, each in its own field of application. The NLGC theory is the most precise in giving an estimate for the diffusion coefficient. We simplified the problem using a 2.5D geometry, which can be a valid approximation to understand the nature of strongly anisotropic (magnetized) fluctuations (Shebalin et al., 1983; Dmitruk et al., 2004; Matthaeus & Lamkin, 1986). We have then "reduced" the NLGC theory to the 2D case. This 2D-NLGC theory has been found to be valuable in describing the diffusion coefficient of particles moving in self-consistent turbulent fields.

For what concerns the acceleration process, the PDFs show that acceleration nature depends on the plasma $\beta$. Acceleration is a stochastic variable for high-$\beta$ plasmas, whereas it is distributed with power-law tails for low $\beta$. We have found that the electric field component parallel to the magnetic field is correlated with particle acceleration. The "anomalously" accelerated particles, i.e. the particles with non-Gaussian acceleration values, are connected to regions with large parallel electric field. This has been seen, qualitatively, by spotting these particles over the parallel electric field map and, quantitatively, by computing conditional statistics. It is worth noting that only a small percentage of particles is anomalous and affected by the acceleration mechanism. Therefore, this result is consistent with the average free-streaming behavior in the out-of-plane direction. The distribution of particles kinetic energy shows interesting features. In low-$\beta$ plasmas the originally thermal distribution develops power-law tails contrary to that of high-$\beta$ which does not significantly evolve in time. We further analyzed the energization process and found that particles moving in the low-$\beta$ plasma experience a break of their magnetic moment that, instead, remains a constant of the motion for high-$\beta$ particles. Additional investigation pointed out a sort of resonance between particles and turbulence characteristic lengths. Indeed, when the Larmor radius is of the order of the current sheets thickness, particles can actively interact with small-

scale intense structures and undergo a coherent acceleration process that result in net energy gain. The resonant interaction between particles and turbulence is the responsible for magnetic moment non-conservation. On the other hand, high-$\beta$ particles have gyration radii much larger than current sheets and therefore, they do not spend considerable time interacting with them. Their acceleration process is stochastic rather than coherent, and no net energy gain is measured. This observation led us to introducing the concept of diffusion in the velocity space. We have shown that energized particles roam in the velocity space in a more ergodic fashion; particles that are accelerated but not energized, instead, have trajectories confined on isoenergetic shells. Unfortunately, we still lack a fundamental theory to determine the diffusion coefficient in velocity space (Miller et al., 1990; Miller & Roberts, 1995), and we leave this work for future studies.

Finally, we compared diffusion and acceleration processes using the HPIC and FPIC algorithms. Ions, in both cases, and at each $\beta$, reach a diffusive behavior at asymptotic times and always follows the 2D-NLGC prescription. The similarity between the hybrid and the full PIC code is not surprising, since diffusion is mostly governed by large, energy-containing scales, and is less sensitive to microphysics. In both approaches we found that particles are better energized in low-$\beta$ simulations because of the scale-resonance process. The difference lies in the effective overall energy gain. Energy distribution of ions in (low-$\beta$) HPIC simulations develops much higher tails than in FPIC. This could be due to some "competition" between ions and electrons (that are treated kinetically in FPIC) resulting in a different partitioning of the energy. Indeed, it is important to notice that, in FPIC, other mechanisms might preferentially heat the electrons rather than the ions, even though the unphysical mass ratio used here cannot clarify completely the possible competition taking place between the two species (Daughton et al., 2011). We, therefore, restricted our comparison to the ion and sub-ion scales and will treat the sub-electron scales in future works.

In this complex, collisionless environment, the interaction between particles and coherent structures such as magnetic islands, reconnecting regions and waves patterns, play a fundamental role (Velli et al., 1989; Marsch, 2006; Kasper et al., 2008; Osman et al., 2010). The turbulent heating might help explain the larger-than-expected temperature of the solar wind as it expands through the heliosphere (Smith et al., 2001), as well as the diffusion of solar energetic particles (Jokipii & Levy, 1977; Isenberg, 2005; J. Tessein et al., 2013).

These results are also particularly relevant for recent observations of non-Maxwellian velocity distribution functions in the turbulent magnetosheath (Burch et al., 2016; Servidio et al., 2017; Yamada et al., 2018), where it has been suggested that the interaction with coherent structures produces non-thermal features. Particle diffusion due to turbulence is particularly relevant in the higher corona, where turbulence enhances the diffusivity of plasma elements, as observed for cometary-tail particles (DeForest et al., 2015). In future and ongoing works we plan to study diffusion and acceleration phenomena in 3D simulations. The 2.5D assumption might affect the power spectrum of the magnetic fluctuations, in particular at (and beyond) the typical proton scales, especially for high $\beta$. As evidenced in the last Section of the second Chapter, the spectral properties, and the scaling of turbulent field have direct influence on particle distributions. Through the investigation of fully 3D simulations, we will be able to create a direct link between the Eulerian properties of the fields with the Lagrangian ones of particles. Using Eulerian field measurements, we might infer Lagrangian properties of particles that are not possible to measure in space plasmas; also conversely, using imaging instruments, it might be possible to observe Lagrangian quantities and obtain information on turbulence properties in regions that cannot be accessed (yet) by spacecraft.

In the last Chapter, we investigated coherent structures in space plasmas at different scales. We extensively used the PVI technique that has been largely applied in the past decade to detect small-scale magnetic discontinuities (Greco et al., 2008; Servidio, Greco, et al., 2011; Chhiber, Goldstein, et al., 2020). Large-PVI events have been demonstrated to be associated with coherent structures such as current sheets that contribute to the intermittent properties of turbulence (Dudok de Wit et al., 2013; Matthaeus et al., 2015). With a novel study, we demonstrated the possibility to use this technique in conjunction with Grad-Shafranov reconstruction algorithms (Sonnerup et al., 1987; Hau & Sonnerup, 1999; Hu, 2017). Because of the different scales the two techniques focuses on, the GS reconstruction and the PVI provide complementary information when implemented together with a single-spacecraft time record of magnetic field. The results obtained demonstrate that these two methods can be employed together, and their synergistic use reveals an overall finer description of flux tube structures. The GS method is sensitive to the large-scale magnetic flux tube structure, i.e., the core currents and O-points, but is not very sensitive to the sharp boundaries,

mostly current sheets and X-points. The PVI method has the opposite sensitivity, providing, principally, information about localized structures that contribute to intermittency, i.e., the flux tube boundaries and associated current sheets. The two methods identify structure boundaries independently, so the result of this procedure provides a reasonable interpretation of the local topology of the magnetic field in the region surrounding the observed data. An important issue related to single-spacecraft is the estimate of electric current density. This quantity can be measured using the curlometer technique (Dunlop et al., 2002) in closely-spaced multispacecraft missions that are equipped with highly sensitive instruments such as MMS/Fast Plasma Investigation instrument (FPI) (Pollock et al., 2016). It is not possible to apply the curlometer to single spacecraft data as it requires spatial directional derivatives. However, using the presented method, one may estimate currents based on these combined approaches: GS reconstruction provides a 2D picture of the weaker flux tube core currents, while the PVI can be used to estimate the most intense currents. Through the combined GS/PVI method, we have provided additional observational evidence that solar wind discontinuities are coherent structures associated with the interaction of adjacent magnetic flux tubes (Greco et al., 2008). In particular, this type of strong-current structures at small scales is readily interpreted as a manifestation of the intermittent nature of fully developed MHD turbulence (Dudok de Wit et al., 2013; Matthaeus et al., 2015).

In the search for large-scale coherent structures in the solar wind, the GS method is one of the many that look for particular kinds of equilibria. Guided by the basic solution of MHD equation that predict equilibrium magnetic field lines to arrange in helix-like configurations, and by magnetic helicity to be an invariant of turbulent systems (Matthaeus & Goldstein, 1982), we have developed a new technique for flux tube detection. It can be classified as a "detection" rather than "identification" technique since it is not devoted to any particular class of equilibria, but rather it exploits the helical nature of such structures. We, again, chose to employ the PVI method for the detection of discontinuities and to use it in conjunction with a real-space method to systematically evaluate magnetic helicity concentrations – which may be recognized as signatures of helical flux ropes. The presented combination has the advantage of being relatively free of assumptions concerning the types of structures that are being identified. PVI is unbiased concerning discontinuity types, and readily detects tangential and rotational discontinuities, shocks, etc. Likewise, the only assumption in developing the

real-space helicity approach is that the statistics of the fluctuations are spatially homogeneous (or, for a time series, time stationary). No assumptions about two-dimensionality or other spatial symmetry are required, in contrast to the standard GS method. We have then conducted a campaign of MHD simulations where the technique has been tested. The simulations provided experimental proof of magnetic helicity to be conserved in turbulence and to concentrate in flux tube cores. The technique has then been applied to PSP data where we found the same results obtained in the simulations. We may conclude that the proposed pair of methods also has the practical advantages in the lack of assumptions and ease of implementation for locating flux ropes and their boundaries in data streams, such as typical single spacecraft solar wind data, as well as in the analysis of very large simulation data sets. We have then developed a GS solver that makes use of this detection technique. The solver exploits the helicity property as a first stage of analysis to locate possible flux ropes and then locally performs a GS reconstruction. The algorithm has been tested in the MHD simulations and preliminary results show that it is able to work on continuous streams of data performing both detection and local reconstruction efficiently.

For future work, it will be desirable to carry out statistical surveys of helical flux ropes and their boundaries using the combined $H_m$–PVI method. There would be considerable scientific value, for example regarding issues of relevance to space weather, in carrying out such surveys at 1 au using extensive data sets such as those available from the ACE and Wind spacecraft. Likewise, surveys of helical flux ropes using additional PSP and Solar Orbiter data will be useful in characterizing the magnetic field helical structure of the inner heliosphere, where this information may be of value in understanding the origin of the solar wind. Such surveys may be facilitated using the present approach due to its simplicity of implementation.

At last, we wanted to conclude this journey, merging the large-scale structure of plasma turbulence with the small-scale kinetic physics described at the beginning. We combined PSP measurements of magnetic field (from FIELDS) and energetic particles (from IS$\odot$IS EPI-Hi and EPI-Lo) from 2020 May 24th to June 3rd. During this interval, it is present a series of consecutive energetic particles events. We perform the $H_m$–PVI analysis to correlate particle populations with helical structures. A global overview suggests the presence of large-scale helical structures overlapping with the most energetic events. More local analyses re-

vealed two complementary but consistent scenarios. The event of May 24th shows the energetic population to be located in the region of space *between* two helical structures. On the other hand, the events during May 27th-28th are trapped *within* two adjacent (and possibly interacting) helical structures. Both events suggest that helical field lines act as "hard" walls for energetic particles. By applying the novel detection technique, we were able to identify structured flux tubes that can provide conduits for energetic particle transport and possible trapping and acceleration (Dudok de Wit et al., 1995; J. Tessein et al., 2013; Khabarova et al., 2016).

The work presented in this thesis aims to contribute to the understanding of plasma turbulence in our neighboring space and possibly extend the gained knowledge to the unexplorable (for the moment) universe. We started describing the micro-physics of charged particle that diffuse in the interplanetary space and are accelerated by explosive events. We developed an analytical theory that describes diffusion taking into account the properties of the turbulent medium. The investigation of acceleration processes shed some light on the possible events that can make particles gain energy. At the other end of the spectrum, we investigated the large-scale structures that populate our heliosphere. We used the GS method to reveal the 2D topology of the magnetic field and developed a synergistic approach to describe these structures at a finer level. We also developed a novel technique that can detect flux ropes with ease in large databases. Finally, large scales and small scales were joined with the observational evidence of energetic particle populations that are modulated by the presence of large- and small-scale coherent structures.

# References


Abe, S., & Thurner, S. (2005). Anomalous diffusion in view of einstein's 1905 theory of brownian motion. *Physica A: Statistical Mechanics and its Applications*, *356*(2), 403-407. doi: https://doi.org/10.1016/j.physa.2005.03.035

Alexandroff, P., & Hopf, H. (2013). *Topologie I.* Springer-Verlag. doi: 10.1007/978-3-662-02021-0

Alexandrova, O., Carbone, V., Veltri, P., & Sorriso-Valvo, L. (2008). Small-scale energy cascade of the solar wind turbulence. *The Astrophysical Journal*, *674*(2), 1153.

Alexandrova, O., Saur, J., Lacombe, C., Mangeney, A., Mitchell, J., Schwartz, S. J., & Robert, P. (2009). Universality of solar-wind turbulent spectrum from mhd to electron scales. *Physical review letters*, *103*(16), 165003.

Ambrosiano, J., Matthaeus, W. H., Goldstein, M. L., & Plante, D. (1988). Test particle acceleration in turbulent reconnecting magnetic fields. *Journal of Geophysical Research: Space Physics*, *93*(A12), 14383–14400.

Bale, S. D., Badman, S. T., Bonnell, J. W., Bowen, T. A., Burgess, D., Case, A. W., ... Wygant, J. R. (2019, December). Highly structured slow solar wind emerging from an equatorial coronal hole. *Nature*, *576*(7786), 237-242. doi: 10.1038/s41586-019-1818-7

Bale, S. D., Goetz, K., Harvey, P. R., Turin, P., Bonnell, J. W., Dudok de Wit, T., ... Wygant, J. R. (2016, Dec 01). The fields instrument suite for solar probe plus. *Space Science Reviews*, *204*(1), 49-82. doi: 10.1007/s11214-016-0244-5

Bale, S. D., Kellogg, P. J., Mozer, F. S., Horbury, T. S., & Reme, H. (2005, June). Measurement of the Electric Fluctuation Spectrum of Magnetohydrodynamic Turbulence. *Physical Review Letters*, *94*(21), 215002. doi: 10.1103/PhysRevLett.94.215002

Batchelor, G. (1976). Brownian diffusion of particles with hydrodynamic interaction. *Journal of Fluid Mechanics*, *74*(1), 1–29.

Bieber, J. W., & Matthaeus, W. H. (1997, August). Perpendicular Diffusion and Drift at Intermediate Cosmic-Ray Energies. *The Astrophysical Journal*, *485*, 655-659. doi: 10.1086/304464

Bieber, J. W., Matthaeus, W. H., Shalchi, A., & Qin, G. (2004, May). Nonlinear guiding center theory of perpendicular diffusion: General properties and comparison with observation. *Geophysical Research Letters*, *31*(10), L10805. doi: 10.1029/2004GL020007

Bieber, J. W., Wanner, W., & Matthaeus, W. H. (1996). Dominant two-dimensional solar wind turbulence with implications for cosmic ray transport. *Journal of Geophysical Research: Space Physics*, *101*(A2), 2511–2522.

Biferale, L., Boffetta, G., Celani, A., Devenish, B. J., Lanotte, A., & Toschi, F. (2005). Lagrangian statistics of particle pairs in homogeneous isotropic turbulence. *Physics of Fluids*, *17*(11), 115101. doi: 10.1063/1.2130742

Birdsall, C. K., & Langdon, A. B. (2004). *Plasma physics via computer simulation.* CRC press.

Blasi, P. (2013, November). The origin of galactic cosmic rays. *The Astronomy and Astrophysics Review*, *21*, 70. doi: 10.1007/s00159-013-0070-7

Boffetta, G., & Celani, A. (2000). Pair dispersion in turbulence. *Physica A: Statistical Mechanics and its Applications*, *280*(1), 1-9. doi: https://doi.org/10.1016/S0378-4371(99)00613-5

Boffetta, G., & Sokolov, I. M. (2002, Feb). Relative dispersion in fully developed turbulence: The richardson's law and intermittency corrections. *Phys. Rev. Lett.*, *88*, 094501. doi: 10.1103/PhysRevLett.88.094501

Bohm, D. (1949). The characteristics of electrical discharges in magnetic fields. *Qualitative Description of the Arc Plasma in a Magnetic Field*.

Borovsky, J. E. (2008, August). Flux tube texture of the solar wind: Strands of the magnetic carpet at 1 AU? *Journal of Geophysical Research (Space Physics)*, *113*, A08110. doi: 10.1029/2007JA012684

Borovsky, J. E. (2010). On the variations of the solar wind magnetic field about the parker spiral direction. *Journal of Geophysical Research: Space Physics*, *115*(A9).

Bruno, R. (2019, May). Intermittency in Solar Wind Turbulence From Fluid to Kinetic Scales. *Earth and Space Science*, *6*(5), 656-672. doi: 10.1029/2018EA000535

Bruno, R., Bavassano, B., Bianchini, L., Pietropaolo, E., Villante, U., Carbone,

V., & Veltri, P. (1999, Dec). Solar Wind Intermittency Studied via Local Intermittency Measure. In A. Wilson & et al. (Eds.), *Magnetic fields and solar processes* (Vol. 9, p. 1147).

Bruno, R., & Carbone, V. (2016). *Turbulence in the solar wind* (Vol. 928). Springer. doi: 10.1007/978-3-319-43440-7

Bruno, R., Carbone, V., Veltri, P., Pietropaolo, E., & Bavassano, B. (2001, October). Identifying intermittency events in the solar wind. *Planetary and Space Science*, *49*(12), 1201-1210. doi: 10.1016/S0032-0633(01)00061-7

Büchner, J., Dum, C., & Scholer, M. (2003). *Space plasma simulation* (Vol. 615). Springer Science & Business Media.

Burch, J. L., Torbert, R. B., Phan, T. D., Chen, L.-J., Moore, T. E., Ergun, R. E., ... Chandler, M. (2016). Electron-scale measurements of magnetic reconnection in space. *Science*, *352*(6290). doi: 10.1126/science.aaf2939

Burlaga, L. (1988). Magnetic clouds and force-free fields with constant alpha. *Journal of Geophysical Research: Space Physics*, *93*(A7), 7217–7224.

Burlaga, L. F. (1969, April). Directional Discontinuities in the Interplanetary Magnetic Field. *Solar Physics*, *7*(1), 54-71. doi: 10.1007/BF00148406

Califano, F., Galeotti, L., & Mangeney, A. (2006, August). The Vlasov-Poisson model and the validity of a numerical approach. *Physics of Plasmas*, *13*(8), 082102. doi: 10.1063/1.2215596

Cartwright, M. L., & Moldwin, M. B. (2010, August). Heliospheric evolution of solar wind small-scale magnetic flux ropes. *Journal of Geophysical Research (Space Physics)*, *115*, A08102. doi: 10.1029/2009JA014271

Chandran, B. D. G., Li, B., Rogers, B. N., Quataert, E., & Germaschewski, K. (2010, September). Perpendicular Ion Heating by Low-frequency Alfvén-wave Turbulence in the Solar Wind. *The Astrophysical Journal*, *720*, 503-515. doi: 10.1088/0004-637X/720/1/503

Chandran, B. D. G., & Maron, J. L. (2004, March). Acceleration of Energetic Particles by Large-Scale Compressible Magnetohydrodynamic Turbulence. *The Astrophysical Journal*, *603*(1), 23-27. doi: 10.1086/377078

Chandrasekhar, S. (1943, Jan). Stochastic problems in physics and astronomy. *Rev. Mod. Phys.*, *15*, 1–89. doi: 10.1103/RevModPhys.15.1

Chen, S., Doolen, G. D., Kraichnan, R. H., & She, Z.-S. (1993, February). On statistical correlations between velocity increments and locally averaged dissipation in homogeneous turbulence. *Physics of Fluids*, *5*, 458-463. doi:

10.1063/1.858897

Chen, S., & Kraichnan, R. H. (1989). Sweeping decorrelation in isotropic turbulence. *Physics of Fluids A: Fluid Dynamics (1989-1993)*, *1*(12), 2019–2024.

Chen, Y., Hu, Q., Zhao, L., Kasper, J. C., Bale, S. D., Korreck, K. E., ... Whittlesey, P. L. (2020, November). Small-scale Magnetic Flux Ropes in the First Two Parker Solar Probe Encounters. *The Astrophysical Journal*, *903*(1), 76. doi: 10.3847/1538-4357/abb820

Chhiber, R., Chasapis, A., Bandyopadhyay, R., Parashar, T. N., Matthaeus, W. H., Maruca, B. A., ... Gershman, D. J. (2018, Dec). Higher-Order Turbulence Statistics in the Earth's Magnetosheath and the Solar Wind Using Magnetospheric Multiscale Observations. *Journal of Geophysical Research (Space Physics)*, *123*(12), 9941-9954. doi: 10.1029/2018JA025768

Chhiber, R., Goldstein, M. L., Maruca, B. A., Chasapis, A., Matthaeus, W. H., Ruffolo, D., ... Raouafi, N. (2020, feb). Clustering of intermittent magnetic and flow structures near parker solar probe's first perihelion—a partial-variance-of-increments analysis. *The Astrophysical Journal Supplement Series*, *246*(2), 31. doi: 10.3847/1538-4365/ab53d2

Chhiber, R., Matthaeus, W., Cohen, C., Ruffolo, D., Sonsrettee, W., Tooprakai, P., ... others (2020). Magnetic field line random walk and solar energetic particle path lengths: Stochastic theory and psp/isois observation. *Astronomy & Astrophysics*. doi: https://doi.org/10.1051/0004-6361/202039816

Chhiber, R., Ruffolo, D., Matthaeus, W. H., Usmanov, A. V., Tooprakai, P., Chuychai, P., & Goldstein, M. L. (2021, feb). Random walk and trapping of interplanetary magnetic field lines: Global simulation, magnetic connectivity, and implications for solar energetic particles. *The Astrophysical Journal*, *908*(2), 174. doi: 10.3847/1538-4357/abd7f0

Chuychai, P., Ruffolo, D., Matthaeus, W. H., & Rowlands, G. (2005, November). Suppressed Diffusive Escape of Topologically Trapped Magnetic Field Lines. *The Astrophysical Journal Letters*, *633*(1), L49-L52. doi: 10.1086/498137

Cohen, C., Christian, E., Cummings, A., Davis, A., Desai, M., de Nolfo, G., ... others (2020). Parker solar probe observations of he/h abundance variations in sep events inside 0.5 au. *Astronomy & Astrophysics*. doi: 10.1051/0004-6361/202039299

Corrsin, S. (1959). Progress report on some turbulent diffusion research. In H. Landsberg & J. Van Mieghem (Eds.), (Vol. 6, p. 161-164). Elsevier. doi:

https://doi.org/10.1016/S0065-2687(08)60102-8

Dalena, S., Greco, A., Rappazzo, A. F., Mace, R. L., & Matthaeus, W. H. (2012, Jul). Magnetic moment nonconservation in magnetohydrodynamic turbulence models. *Phys. Rev. E*, *86*, 016402.

Dasso, S., Milano, L. J., Matthaeus, W. H., & Smith, C. W. (2005, dec). Anisotropy in fast and slow solar wind fluctuations. *The Astrophysical Journal*, *635*(2), L181–L184. doi: 10.1086/499559

Daughton, W., Roytershteyn, V., Karimabadi, H., Yin, L., Albright, B. J., Bergen, B., & Bowers, K. J. (2011, July). Role of electron physics in the development of turbulent magnetic reconnection in collisionless plasmas. *Nature Physics*, *7*, 539-542. doi: 10.1038/nphys1965

DeForest, C. E., Matthaeus, W. H., Howard, T. A., & Rice, D. R. (2015, October). Turbulence in the Solar Wind Measured with Comet Tail Test Particles. *The Astrophysical Journal*, *812*, 108. doi: 10.1088/0004-637X/812/2/108

De Hoffmann, F., & Teller, E. (1950, Nov). Magneto-hydrodynamic shocks. *Phys. Rev.*, *80*, 692–703. doi: 10.1103/PhysRev.80.692

Dmitruk, P., Matthaeus, W. H., & Seenu, N. (2004, December). Test Particle Energization by Current Sheets and Nonuniform Fields in Magnetohydrodynamic Turbulence. *The Astrophysical Journal*, *617*, 667-679. doi: 10.1086/425301

Dmitruk, P., Matthaeus, W. H., Seenu, N., & Brown, M. R. (2003, oct). Test particle acceleration in three-dimensional magnetohydrodynamic turbulence. *The Astrophysical Journal*, *597*(1), L81–L84. doi: 10.1086/379751

Drake, J., Swisdak, M., Che, H., & Shay, M. (2006). Electron acceleration from contracting magnetic islands during reconnection. *Nature*, *443*(7111), 553–556.

Drake, J. F., Cassak, P. A., Shay, M. A., Swisdak, M., & Quataert, E. (2009, July). A Magnetic Reconnection Mechanism for Ion Acceleration and Abundance Enhancements in Impulsive Flares. *The Astrophysical Journal Letters*, *700*(1), L16-L20. doi: 10.1088/0004-637X/700/1/L16

Drake, J. F., Opher, M., Swisdak, M., & Chamoun, J. N. (2010, February). A Magnetic Reconnection Mechanism for the Generation of Anomalous Cosmic Rays. *The Astrophysical Journal*, *709*, 963-974. doi: 10.1088/0004-637X/709/2/963

Dröge, W., Kartavykh, Y. Y., Dresing, N., & Klassen, A. (2016, August). Multi-spacecraft Observations and Transport Modeling of Energetic Electrons for

a Series of Solar Particle Events in August 2010. *The Astrophysical Journal*, *826*(2), 134. doi: 10.3847/0004-637X/826/2/134

Du, S., Guo, F., Zank, G. P., Li, X., & Stanier, A. (2018, oct). Plasma energization in colliding magnetic flux ropes. *The Astrophysical Journal*, *867*(1), 16. doi: 10.3847/1538-4357/aae30e

Dudok de Wit, T., Alexandrova, O., Furno, I., Sorriso-Valvo, L., & Zimbardo, G. (2013, Oct 01). Methods for characterising microphysical processes in plasmas. *Space Science Reviews*, *178*(2), 665-693. doi: 10.1007/s11214-013-9974-9

Dudok de Wit, T., Benkadda, S., Gabbai, P., & Verga, A. D. (1995, Dec). Transport and self-organization in dissipative drift-wave turbulence. *Phys. Rev. E*, *52*, 6753–6758. doi: 10.1103/PhysRevE.52.6753

Dundovic, A., Pezzi, O., Blasi, P., Evoli, C., & Matthaeus, W. H. (2020, July). Novel aspects of cosmic ray diffusion in synthetic magnetic turbulence. *arXiv e-prints*, arXiv:2007.09142.

Dunlop, M., Balogh, A., Glassmeier, K.-H., & Robert, P. (2002). Four-point cluster application of magnetic field analysis tools: The curlometer. *Journal of Geophysical Research: Space Physics*, *107*(A11), SMP–23.

Ebersohn, F. H., Sheehan, J., Longmier, B. W., & Shebalin, J. (2014, July). Quasi-one-dimensional code for particle-in-cell simulation of magnetic nozzle expansion. *50th AIAA/ASME/SAE/ASEE Joint Propulsion Conference*. doi: 10.2514/6.2014-4027

Einaudi, G., Velli, M., Politano, H., & Pouquet, A. (1996). Energy release in a turbulent corona. *The Astrophysical Journal Letters*, *457*(2), L113. doi: 10.1086/309893

Einstein, A. (1905). Über die von der molekularkinetischen Theorie der Wärme geforderte Bewegung von in ruhenden Flüssigkeiten suspendierten Teilchen. *Annalen der Physik*, *322*, 549-560. doi: 10.1002/andp.19053220806

Farge, M. (1992). Wavelet transforms and their applications to turbulence. *Annual review of fluid mechanics*, *24*(1), 395–458.

Farge, M., & Schneider, K. (2015, December). Wavelet transforms and their applications to MHD and plasma turbulence: a review. *Journal of Plasma Physics*, *81*(6), 435810602. doi: 10.1017/S0022377815001075

Feng, H. Q., Wu, D. J., Lin, C. C., Chao, J. K., Lee, L. C., & Lyu, L. H. (2008, December). Interplanetary small- and intermediate-sized magnetic flux

ropes during 1995-2005. *Journal of Geophysical Research (Space Physics)*, *113*(A12), A12105. doi: 10.1029/2008JA013103

Fermi, E. (1949, April). On the Origin of the Cosmic Radiation. *Physical Review*, *75*(8), 1169-1174. doi: 10.1103/PhysRev.75.1169

Fermi, E. (1954, January). Galactic Magnetic Fields and the Origin of Cosmic Radiation. *The Astrophysical Journal*, *119*, 1. doi: 10.1086/145789

Fox, N. J., Velli, M. C., Bale, S. D., Decker, R., Driesman, A., Howard, R. A., ... Szabo, A. (2016). The solar probe plus mission: humanity's first visit to our star. *Space Science Reviews*, *204*(1-4), 7–48. doi: 10.1007/s11214-015-0211-6

Franci, L., Cerri, S. S., Califano, F., Landi, S., Papini, E., Verdini, A., ... Hellinger, P. (2017, Nov). Magnetic Reconnection as a Driver for a Sub-ion-scale Cascade in Plasma Turbulence. *The Astrophysical Journal*, *850*(1), L16. doi: 10.3847/2041-8213/aa93fb

Franci, L., Landi, S., Matteini, L., Verdini, A., & Hellinger, P. (2015, October). High-resolution Hybrid Simulations of Kinetic Plasma Turbulence at Proton Scales. *The Astrophysical Journal*, *812*, 21. doi: 10.1088/0004-637X/812/1/21

Franci, L., Landi, S., Verdini, A., Matteini, L., & Hellinger, P. (2018, January). Solar Wind Turbulent Cascade from MHD to Sub-ion Scales: Large-size 3D Hybrid Particle-in-cell Simulations. *The Astrophysical Journal*, *853*, 26. doi: 10.3847/1538-4357/aaa3e8

Frisch, U. (1995). *Turbulence: the legacy of AN Kolmogorov*. Cambridge university press.

Ghosh, S., Hossain, M., & Matthaeus, W. H. (1993). The application of spectral methods in simulating compressible fluid and magnetofluid turbulence. *Comp. Phys. Comm.*, *74*, 18.

Glassmeier, K. H., Motschmann, U., Dunlop, M., Balogh, A., Acuña, M. H., Carr, C., ... Buchert, S. (2001, Oct). Cluster as a wave telescope - first results from the fluxgate magnetometer. *Annales Geophysicae*, *19*(10), 1439-1447. doi: 10.5194/angeo-19-1439-2001

González, A. O., Domingues, M., Mendes, O., Kaibara, M., & Prestes, A. (2015). Grad-shafranov reconstruction: Overview and improvement of the numerical solution used in space physics. *Brazilian Journal of Physics*, *45*(5), 493–509. doi: 10.1007/s13538-015-0342-y

Gosling, J. T. (1990). Coronal mass ejections and magnetic flux ropes in interplanetary space. In *Physics of magnetic flux ropes* (p. 343-364). American Geophysical Union (AGU). doi: https://doi.org/10.1029/GM058p0343

Gosling, J. T., & Szabo, A. (2008). Bifurcated current sheets produced by magnetic reconnection in the solar wind. *Journal of Geophysical Research: Space Physics*, *113*(A10). doi: https://doi.org/10.1029/2008JA013473

Gottlieb, D., & Orszag, S. A. (1977). *Numerical analysis of spectral methods: Theory and applications*. SIAM.

Grad, H., & Rubin, H. (1958). Hydromagnetic equilibria and force-free fields. *Journal of Nuclear Energy (1954)*, *7*(3-4), 284–285.

Greco, A., Chuychai, P., Matthaeus, W. H., Servidio, S., & Dmitruk, P. (2008, October). Intermittent MHD structures and classical discontinuities. *Geophysical Research Letters*, *35*, L19111. doi: 10.1029/2008GL035454

Greco, A., Matthaeus, W. H., Perri, S., Osman, K. T., Servidio, S., Wan, M., & Dmitruk, P. (2018, February). Partial Variance of Increments Method in Solar Wind Observations and Plasma Simulations. *Space Science Reviews*, *214*(1), 1. doi: 10.1007/s11214-017-0435-8

Greco, A., Matthaeus, W. H., Servidio, S., Chuychai, P., & Dmitruk, P. (2009, February). Statistical Analysis of Discontinuities in Solar Wind ACE Data and Comparison with Intermittent MHD Turbulence. *The Astrophysical Journall*, *691*, L111-L114. doi: 10.1088/0004-637X/691/2/L111

Greco, A., Matthaeus, W. H., Servidio, S., & Dmitruk, P. (2009, October). Waiting-time distributions of magnetic discontinuities: Clustering or Poisson process? *Phys. Rev. E*, *80*(4), 046401.

Greco, A., & Perri, S. (2014, April). Identification of High Shears and Compressive Discontinuities in the Inner Heliosphere. *The Astrophysical Journal*, *784*(2), 163. doi: 10.1088/0004-637X/784/2/163

Greco, A., Perri, S., Servidio, S., Yordanova, E., & Veltri, P. (2016, Jun). The Complex Structure of Magnetic Field Discontinuities in the Turbulent Solar Wind. *The Astrophysical Journal*, *823*(2), L39. doi: 10.3847/2041-8205/823/2/L39

Green, M. S. (1951, August). Brownian Motion in a Gas of Noninteracting Molecules. *The Journal of Chemical Physics*, *19*, 1036-1046. doi: 10.1063/1.1748449

Guo, F., Li, H., Daughton, W., Li, X., & Liu, Y.-H. (2016). Particle acceleration

during magnetic reconnection in a low-beta pair plasma. *Physics of Plasmas*, *23*(5), 055708. doi: 10.1063/1.4948284

Guo, F., Liu, Y.-H., Daughton, W., & Li, H. (2015, jun). Particle acceleration and plasma dynamics during magnetic reconnection in the magnetically dominated regime. *The Astrophysical Journal*, *806*(2), 167. doi: 10.1088/0004-637x/806/2/167

Hada, T., Koga, D., & Yamamoto, E. (2003, April). Phase coherence of MHD waves in the solar wind. *Space Science Reviews*, *107*(1), 463-466. doi: 10.1023/A:1025506124402

Hasegawa, H., Denton, R. E., Nakamura, R., Genestreti, K. J., Nakamura, T. K. M., Hwang, K.-J., ... Saito, Y. (2019, January). Reconstruction of the Electron Diffusion Region of Magnetotail Reconnection Seen by the MMS Spacecraft on 11 July 2017. *Journal of Geophysical Research (Space Physics)*, *124*, 122-138. doi: 10.1029/2018JA026051

Hau, L.-N., & Sonnerup, B. U. Ö. (1999, April). Two-dimensional coherent structures in the magnetopause: Recovery of static equilibria from single-spacecraft data. *Journal of Geophysical Research*, *104*, 6899-6918. doi: 10.1029/1999JA900002

Hayashi, T., & Sato, T. (1978). Magnetic reconnection: Acceleration, heating, and shock formation. *Journal of Geophysical Research: Space Physics*, *83*(A1), 217–220. doi: 10.1029/JA083iA01p00217

Haynes, C. T., Burgess, D., & Camporeale, E. (2014, March). Reconnection and Electron Temperature Anisotropy in Sub-proton Scale Plasma Turbulence. *The Astrophysical Journal*, *783*, 38. doi: 10.1088/0004-637X/783/1/38

Horbury, T. S., Forman, M. A., & Oughton, S. (2005, nov). Spacecraft observations of solar wind turbulence: an overview. *Plasma Physics and Controlled Fusion*, *47*(12B), B703–B717. doi: 10.1088/0741-3335/47/12b/s52

Hoshino, M., Mukai, T., Terasawa, T., & Shinohara, I. (2001). Suprathermal electron acceleration in magnetic reconnection. *Journal of Geophysical Research: Space Physics*, *106*(A11), 25979-25997. doi: https://doi.org/10.1029/2001JA900052

Howes, G., Dorland, W., Cowley, S., Hammett, G., Quataert, E., Schekochihin, A., & Tatsuno, T. (2008). Kinetic simulations of magnetized turbulence in astrophysical plasmas. *Physical Review Letters*, *100*(6), 065004.

Howes, G. G. (2017, May). A prospectus on kinetic heliophysics. *Physics of*

*Plasmas*, *24*(5), 055907. doi: 10.1063/1.4983993

Howes, G. G., McCubbin, A. J., & Klein, K. G. (2018, Feb). Spatially localized particle energization by Landau damping in current sheets produced by strong Alfvén wave collisions. *Journal of Plasma Physics*, *84*(1), 905840105. doi: 10.1017/S0022377818000053

Hu, Q. (2017, Aug 01). The grad-shafranov reconstruction in twenty years: 1996–2016. *Science China Earth Sciences*, *60*(8), 1466-1494. doi: 10.1007/s11430-017-9067-2

Hu, Q. (2017, June). The Grad-Shafranov Reconstruction in Twenty Years: 1996 - 2016. *Sci. China Earth Sciences*, *60*, 1466-1494. doi: doi:10.1007/s11430-017-9067-2

Hu, Q., & Sonnerup, B. U. (2002). Reconstruction of magnetic clouds in the solar wind: Orientations and configurations. *Journal of Geophysical Research: Space Physics*, *107*(A7), SSH–10.

Hu, Q., Zheng, J., Chen, Y., le Roux, J., & Zhao, L. (2018, November). Automated Detection of Small-scale Magnetic Flux Ropes in the Solar Wind: First Results from the Wind Spacecraft Measurements. *The Astrophysical Journal Supplement Series*, *239*, 12. doi: 10.3847/1538-4365/aae57d

Isenberg, P. A. (2005, April). Turbulence-driven Solar Wind Heating and Energization of Pickup Protons in the Outer Heliosphere. *The Astrophysical Journal*, *623*, 502-510. doi: 10.1086/428609

Jacobs, C., Roussev, I. I., Lugaz, N., & Poedts, S. (2009, April). The Internal Structure of Coronal Mass Ejections: Are all Regular Magnetic Clouds Flux Ropes? *The Astrophysical Journal Letters*, *695*(2), L171-L175. doi: 10.1088/0004-637X/695/2/L171

Jokipii, J. (1966). Cosmic-ray propagation. i. charged particles in a random magnetic field. *The Astrophysical Journal*, *146*, 480.

Jokipii, J. (1973). Turbulence and scintillations in the interplanetary plasma. *Annual Review of Astronomy and Astrophysics*, *11*(1), 1–28.

Jokipii, J., & Parker, E. (1969, March). Stochastic aspects of magnetic lines of force with application to cosmic-ray propagation. *The Astrophysical Journal*, *155*, 777.

Jokipii, J. R., & Levy, E. H. (1977, April). Effects of particle drifts on the solar modulation of galactic cosmic rays. *The Astrophysical Journal Letters*, *213*, L85-L88. doi: 10.1086/182415

Kasper, J. C., Abiad, R., Austin, G., Balat-Pichelin, M., Bale, S. D., Belcher, J. W., ... Zank, G. (2016, Dec 01). Solar wind electrons alphas and protons (sweap) investigation: Design of the solar wind and coronal plasma instrument suite for solar probe plus. *Space Science Reviews*, *204*(1), 131-186. doi: 10.1007/s11214-015-0206-3

Kasper, J. C., Lazarus, A. J., & Gary, S. P. (2008, Dec). Hot solar-wind helium: Direct evidence for local heating by alfvén-cyclotron dissipation. *Phys. Rev. Lett.*, *101*, 261103. doi: 10.1103/PhysRevLett.101.261103

Khabarova, O., Zank, G. P., Li, G., le Roux, J. A., Webb, G. M., Dosch, A., & Malandraki, O. E. (2015, August). Small-scale Magnetic Islands in the Solar Wind and Their Role in Particle Acceleration. I. Dynamics of Magnetic Islands Near the Heliospheric Current Sheet. *The Astrophysical Journal*, *808*(2), 181. doi: 10.1088/0004-637X/808/2/181

Khabarova, O., Zharkova, V., Xia, Q., & Malandraki, O. E. (2020, May). Counter-streaming Strahls and Heat Flux Dropouts as Possible Signatures of Local Particle Acceleration in the Solar Wind. *The Astrophysical Journal Letters*, *894*(1), L12. doi: 10.3847/2041-8213/ab8cb8

Khabarova, O. V., & Zank, G. P. (2017). Energetic particles of kev–mev energies observed near reconnecting current sheets at 1 au. *The Astrophysical Journal*, *843*(1), 4. doi: 10.3847/1538-4357/aa7686

Khabarova, O. V., Zank, G. P., Li, G., Malandraki, O. E., le Roux, J. A., & Webb, G. M. (2016). Small-scale magnetic islands in the solar wind and their role in particle acceleration. ii. particle energization inside magnetically confined cavities. *The Astrophysical Journal*, *827*(2), 122.

Kittinaradorn, R., Ruffolo, D., & Matthaeus, W. (2009). Solar moss patterns: heating of coronal loops by turbulence and magnetic connection to the footpoints. *The Astrophysical Journal Letters*, *702*(2), L138.

Kivelson, M. G., & Russell, C. T. (1995). *Introduction to space physics*. Cambridge University Press.

Klein, K.-L., Krucker, S., Lointier, G., & Kerdraon, A. (2008). Open magnetic flux tubes in the corona and the transport of solar energetic particles. *A&A*, *486*(2), 589-596. doi: 10.1051/0004-6361:20079228

Klimontovich, Y. L. (1997, January). Physics of collisionless plasma. *Physics Uspekhi*, *40*(1), 21-51. doi: 10.1070/PU1997v040n01ABEH000200

Kraichnan, R. H., & Panda, R. (1988). Depression of nonlinearity in decaying

isotropic turbulence. *The Physics of fluids*, *31*(9), 2395–2397. doi: 10.1063/1.866591

Krishna Jagarlamudi, V., Dudok de Wit, T., Krasnoselskikh, V., & Maksimovic, M. (2019, January). Inherentness of Non-stationarity in Solar Wind. *The Astrophysical Journal*, *871*(1), 68. doi: 10.3847/1538-4357/aaef2e

Kubo, R. (1957, June). Statistical-Mechanical Theory of Irreversible Processes. I. *Journal of the Physical Society of Japan*, *12*, 570-586. doi: 10.1143/JPSJ.12.570

Lapenta, G. (2012). Particle simulations of space weather. *Journal of Computational Physics*, *231*(3), 795–821.

Lapenta, G. (2017, April). Exactly energy conserving semi-implicit particle in cell formulation. *Journal of Computational Physics*, *334*, 349-366. doi: 10.1016/j.jcp.2017.01.002

Lapenta, G., & Markidis, S. (2011, July). Particle acceleration and energy conservation in particle in cell simulations. *Physics of Plasmas*, *18*(7), 072101. doi: 10.1063/1.3602216

Lapenta, G., Markidis, S., Goldman, M. V., & Newman, D. L. (2015). Secondary reconnection sites in reconnection-generated flux ropes and reconnection fronts. *Nature Physics*, *11*(8), 690–695.

le Roux, J. A., Zank, G. P., Webb, G. M., & Khabarova, O. (2015, March). A Kinetic Transport Theory for Particle Acceleration and Transport in Regions of Multiple Contracting and Reconnecting Inertial-scale Flux Ropes. *The Astrophysical Journal*, *801*, 112. doi: 10.1088/0004-637X/801/2/112

Lepping, R. P., Acũna, M. H., Burlaga, L. F., Farrell, W. M., Slavin, J. A., Schatten, K. H., ... Worley, E. M. (1995, February). The Wind Magnetic Field Investigation. *Space Science Reviews*, *71*, 207-229. doi: 10.1007/BF00751330

le Roux, J. A., Webb, G. M., Zank, G. P., & Khabarova, O. (2015, sep). Energetic ion acceleration by small-scale solar wind flux ropes. *Journal of Physics: Conference Series*, *642*, 012015. doi: 10.1088/1742-6596/642/1/012015

le Roux, J. A., Zank, G. P., & Khabarova, O. V. (2018, sep). Self-consistent energetic particle acceleration by contracting and reconnecting small-scale flux ropes: The governing equations. *The Astrophysical Journal*, *864*(2), 158. doi: 10.3847/1538-4357/aad8b3

Longmire, C. L., & Rosenbluth, M. N. (1956, Aug). Diffusion of charged particles

across a magnetic field. *Phys. Rev.*, *103*, 507–510. doi: 10.1103/PhysRev.103.507

Luo, H., Kronberg, E. A., Nykyri, K., Trattner, K. J., Daly, P. W., Chen, G. X., ... Ge, Y. S. (2017). Imf dependence of energetic oxygen and hydrogen ion distributions in the near-earth magnetosphere. *Journal of Geophysical Research: Space Physics*, *122*(5), 5168–5180. doi: 10.1002/2016JA023471

Malandraki, O., Khabarova, O., Bruno, R., Zank, G. P., Li, G., Jackson, B., ... Engelbrecht, N. E. (2019, August). Current Sheets, Magnetic Islands, and Associated Particle Acceleration in the Solar Wind as Observed by Ulysses near the Ecliptic Plane. *The Astrophysical Journal*, *881*(2), 116. doi: 10.3847/1538-4357/ab289a

Markidis, S., Lapenta, G., & Rizwan-uddin. (2010). Multi-scale simulations of plasma with ipic3d. *Mathematics and Computers in Simulation*, *80*(7), 1509 - 1519. (Multiscale modeling of moving interfaces in materials) doi: https://doi.org/10.1016/j.matcom.2009.08.038

Marsch, E. (2006). Kinetic physics of the solar corona and solar wind. *JLR*, *3*.

Matthaeus, W. H., & Goldstein, M. L. (1982). Measurement of the rugged invariants of magnetohydrodynamic turbulence in the solar wind. *Journal of Geophysical Research*, *87*, 6011–6028. doi: 10.1029/JA087iA08p06011

Matthaeus, W. H., Goldstein, M. L., & Smith, C. (1982). Evaluation of magnetic helicity in homogeneous turbulence. *Physical Review Letters*, *48*(18), 1256.

Matthaeus, W. H., & Lamkin, S. L. (1986, August). Turbulent magnetic reconnection. *Physics of Fluids*, *29*, 2513-2534. doi: 10.1063/1.866004

Matthaeus, W. H., & Montgomery, D. (1980). Selective decay hypothesis at high mechanical and magnetic reynolds numbers. *New York Academy of Sciences, Annals*, *357*, 203–222. doi: 10.1111/j.1749-6632.1980.tb29687.x

Matthaeus, W. H., Parashar, T. N., Wan, M., & Wu, P. (2016, Aug). Turbulence and Proton-Electron Heating in Kinetic Plasma. *The Astrophysical Journal*, *827*(1), L7. doi: 10.3847/2041-8205/827/1/L7

Matthaeus, W. H., Qin, G., Bieber, J. W., & Zank, G. P. (2003, may). Nonlinear collisionless perpendicular diffusion of charged particles. *The Astrophysical Journal*, *590*(1), L53–L56. doi: 10.1086/376613

Matthaeus, W. H., Servidio, S., & Dmitruk, P. (2008, October). Comment on "Kinetic Simulations of Magnetized Turbulence in Astrophysical Plasmas". *Physical Review Letters*, *101*(14), 149501. doi: 10.1103/PhysRevLett.101

.149501

Matthaeus, W. H., Wan, M., Servidio, S., Greco, A., Osman, K. T., Oughton, S., & Dmitruk, P. (2015). Intermittency, nonlinear dynamics and dissipation in the solar wind and astrophysical plasmas. *Philosophical Transactions of the Royal Society A: Mathematical, Physical and Engineering Sciences*, *373*(2041), 20140154.

Matthews, A. P. (1994, May). Current Advance Method and Cyclic Leapfrog for 2D Multispecies Hybrid Plasma Simulations. *Journal of Computational Physics*, *112*, 102-116. doi: 10.1006/jcph.1994.1084

Mazur, J. E., Mason, G. M., Dwyer, J. R., Giacalone, J., Jokipii, J. R., & Stone, E. C. (2000, mar). Interplanetary magnetic field line mixing deduced from impulsive solar flare particles. *The Astrophysical Journal*, *532*(1), L79–L82. doi: 10.1086/312561

McComas, D. J., Alexander, N., Angold, N., Bale, S., Beebe, C., Birdwell, B., ... Wilson, P. (2016, Dec 01). Integrated science investigation of the sun (isis): Design of the energetic particle investigation. *Space Science Reviews*, *204*(1), 187-256. doi: 10.1007/s11214-014-0059-1

McComb, W. D. (1990). *The physics of fluid turbulence*. Oxford University Press.

McCracken, K. G., & Ness, N. F. (1966). The collimation of cosmic rays by the interplanetary magnetic field. *Journal of Geophysical Research (1896-1977)*, *71*(13), 3315-3318. doi: https://doi.org/10.1029/JZ071i013p03315

Melzani, M., Walder, R., Folini, D., Winisdoerffer, C., & Favre, J. M. (2014, October). The energetics of relativistic magnetic reconnection: ion-electron repartition and particle distribution hardness. *Astronomy & Astrophysics*, *570*, A112. doi: 10.1051/0004-6361/201424193

Meyer, P., Parker, E. N., & Simpson, J. A. (1956, Nov). Solar cosmic rays of february, 1956 and their propagation through interplanetary space. *Phys. Rev.*, *104*, 768–783. doi: 10.1103/PhysRev.104.768

Mignone, A., Bodo, G., Massaglia, S., Matsakos, T., Tesileanu, O., Zanni, C., & Ferrari, A. (2007, may). PLUTO: A numerical code for computational astrophysics. *The Astrophysical Journal Supplement Series*, *170*(1), 228–242. doi: 10.1086/513316

Miller, J. A., Guessoum, N., & Ramaty, R. (1990, October). Stochastic Fermi acceleration in solar flares. *The Astrophysical Journal*, *361*, 701-708.

Miller, J. A., & Roberts, D. A. (1995, October). Stochastic Proton Acceleration

by Cascading Alfven Waves in Impulsive Solar Flares. *The Astrophysical Journal*, *452*, 912.

Moldwin, M. B., Ford, S., Lepping, R., Slavin, J., & Szabo, A. (2000, January). Small-scale magnetic flux ropes in the solar wind. *Geophysical Research Letters*, *27*, 57-60. doi: 10.1029/1999GL010724

Moldwin, M. B., Phillips, J. L., Gosling, J. T., Scime, E. E., McComas, D. J., Bame, S. J., ... Forsyth, R. J. (1995, October). Ulysses observation of a noncoronal mass ejection flux rope: Evidence of interplanetary magnetic reconnection. *Journal of Geophysical Research*, *100*, 19903-19910. doi: 10 .1029/95JA01123

Morrison, P. (1956, Feb). Solar origin of cosmic-ray time variations. *Phys. Rev.*, *101*, 1397–1404. doi: 10.1103/PhysRev.101.1397

Möstl, C., Farrugia, C., Biernat, H., Leitner, M., Kilpua, E., Galvin, A., & Luhmann, J. (2009). Optimized grad–shafranov reconstruction of a magnetic cloud using stereo-wind observations. *Solar Physics*, *256*(1-2), 427–441. doi: 10.1007/s11207-009-9360-7

Müller, D., St. Cyr, O. C., Zouganelis, I., Gilbert, H. R., Marsden, R., Nieves-Chinchilla, T., ... Williams, D. (2020). The solar orbiter mission - science overview. *A&A*, *642*, A1. doi: 10.1051/0004-6361/202038467

Narita, Y., Glassmeier, K. H., Sahraoui, F., & Goldstein, M. L. (2010, Apr). Wave-Vector Dependence of Magnetic-Turbulence Spectra in the Solar Wind. *Physical Review Letters*, *104*(17), 171101. doi: 10.1103/PhysRevLett.104 .171101

Nelkin, M., & Tabor, M. (1990). Time correlations and random sweeping in isotropic turbulence. *Physics of Fluids A: Fluid Dynamics (1989-1993)*, *2*(1), 81–83.

Odstrcil, D. (2003). Modeling 3-d solar wind structure. *Advances in Space Research*, *32*(4), 497-506. (Heliosphere at Solar Maximum) doi: https:// doi.org/10.1016/S0273-1177(03)00332-6

Ogilvie, K. W., Chornay, D. J., Fritzenreiter, R. J., Hunsaker, F., Keller, J., Lobell, J., ... Gergin, E. (1995, February). SWE, A Comprehensive Plasma Instrument for the Wind Spacecraft. *Space Science Reviews*, *71*, 55-77. doi: 10.1007/BF00751326

Olshevsky, V., Servidio, S., Pucci, F., Primavera, L., & Lapenta, G. (2018, June). Properties of Decaying Plasma Turbulence at Subproton Scales. *The Astro-*

*physical Journal*, *860*, 11. doi: 10.3847/1538-4357/aac1bd

Ongena, J., Koch, R., Wolf, R., & Zohm, H. (2016). Magnetic-confinement fusion. *Nature Physics*, *12*(5), 398.

Ono, Y., Yamada, M., Akao, T., Tajima, T., & Matsumoto, R. (1996, Apr). Ion acceleration and direct ion heating in three-component magnetic reconnection. *Phys. Rev. Lett.*, *76*, 3328–3331. doi: 10.1103/PhysRevLett.76.3328

Orszag, S. A., & Patterson, G. S. (1972, January). Numerical Simulation of Three-Dimensional Homogeneous Isotropic Turbulence. *Physical Review Letters*, *28*(2), 76-79. doi: 10.1103/PhysRevLett.28.76

Osman, K., Matthaeus, W., Gosling, J., Greco, A., Servidio, S., Hnat, B., ... Phan, T. (2014). Magnetic reconnection and intermittent turbulence in the solar wind. *Physical Review Letters*, *112*(21), 215002.

Osman, K., Matthaeus, W., Greco, A., & Servidio, S. (2010). Evidence for inhomogeneous heating in the solar wind. *The Astrophysical Journal Letters*, *727*(1), L11. doi: 10.1088/2041-8205/727/1/l11

Oughton, S., Matthaeus, W., Wan, M., & Osman, K. (2015). Anisotropy in solar wind plasma turbulence. *Philosophical Transactions of the Royal Society A: Mathematical, Physical and Engineering Sciences*, *373*(2041), 20140152.

Panchev, S. (1971). *Random functions and turbulence.* New York: Pergammon Press.

Parashar, T., Goldstein, M., Maruca, B., Matthaeus, W., Ruffolo, D., Bandyopadhyay, R., ... others (2020). Measures of scale-dependent Alfvénicity in the first PSP solar encounter. *The Astrophysical Journal Supplement Series*, *246*(2), 58.

Parashar, T. N., Vasquez, B. J., & Markovskii, S. A. (2014, February). The role of electron equation of state in heating partition of protons in a collisionless plasma. *Physics of Plasmas*, *21*(2), 022301. doi: 10.1063/1.4863422

Parker, E. (1965). The passage of energetic charged particles through interplanetary space. *Planetary and Space Science*, *13*(1), 9 - 49. doi: https://doi.org/10.1016/0032-0633(65)90131-5

Parker, E. N. (1957, December). Sweet's Mechanism for Merging Magnetic Fields in Conducting Fluids. *Journal of Geophysical Research*, *62*, 509-520. doi: 10.1029/JZ062i004p00509

Parker, E. N. (1958, November). Dynamics of the Interplanetary Gas and Magnetic Fields. *The Astrophysical Journal*, *128*, 664. doi: 10.1086/146579

Paschmann, G., & Daly, P. W. (1998, January). Analysis Methods for Multi-Spacecraft Data. ISSI Scientific Reports Series SR-001, ESA/ISSI, Vol. 1. ISBN 1608-280X, 1998. *ISSI Scientific Reports Series*, *1*.

Pecora, F., Greco, A., Hu, Q., Servidio, S., Chasapis, A. G., & Matthaeus, W. H. (2019). Single-spacecraft identification of flux tubes and current sheets in the solar wind. *The Astrophysical Journal Letters*, *881*(1), L11. doi: doi.org/10.3847/2041-8213/ab32d9

Pecora, F., Pucci, F., Lapenta, G., Burgess, D., & Servidio, S. (2019). Statistical analysis of ions in two-dimensional plasma turbulence. *Solar Physics*, *294*(9), 114. doi: doi.org/10.1007/s11207-019-1507-6

Pecora, F., Servidio, S., Greco, A., & Matthaeus, W. H. (2020). Identification of coherent structures in space plasmas: The magnetic helicity-pvi method. *Astronomy & Astrophysics*. doi: 10.1051/0004-6361/202039639

Pecora, F., Servidio, S., Greco, A., Matthaeus, W. H., D. Burgess, C. T. H., Carbone, V., & Veltri, P. (2018). Ion Diffusion and Acceleration in Plasma Turbulence. *Journal of Plasma Physics*, *84*(6), 725840601. doi: doi.org/10.1017/S0022377818000995

Pegoraro, F., Kuvshinov, B. N., Rem, J., & Schep, T. J. (1997, January). Electron inertia and small-scale magnetic structures in a nonuniform collisionless plasma. *Advances in Space Research*, *19*(12), 1823-1826. doi: 10.1016/S0273-1177(97)00083-5

Perri, S., Goldstein, M. L., Dorelli, J. C., & Sahraoui, F. (2012, Nov). Detection of small-scale structures in the dissipation regime of solar-wind turbulence. *Phys. Rev. Lett.*, *109*, 191101. doi: 10.1103/PhysRevLett.109.191101

Perri, S., Servidio, S., Vaivads, A., & Valentini, F. (2017, July). Numerical Study on the Validity of the Taylor Hypothesis in Space Plasmas. *The Astrophysical Journal Supplement Series*, *231*, 4. doi: 10.3847/1538-4365/aa755a

Poedts, S., & Goedbloed, J. P. (1997, May). Nonlinear wave heating of solar coronal loops. *Astronomy & Astrophysics*, *321*, 935-944.

Poedts, S., Toth, G., Belien, A. J. C., & Goedbloed, J. P. (1997, May). Nonlinear MHD Simulations of Wave Dissipation in Flux Tubes. *Solar Physics*, *172*, 45-52. doi: 10.1023/A:1004924017304

Pollock, C., Moore, T., Jacques, A., Burch, J., Gliese, U., Saito, Y., ... Zeuch, M. (2016, March). Fast Plasma Investigation for Magnetospheric Multiscale. *Space Science Reviews*, *199*(1-4), 331-406. doi: 10.1007/s11214-016-0245-4

Pommois, P., Zimbardo, G., & Veltri, P. (2007, January). Anomalous, non-Gaussian transport of charged particles in anisotropic magnetic turbulence. *Physics of Plasmas*, *14*(1), 012311. doi: 10.1063/1.2434795

Pomoell, J., & Poedts, S. (2018). Euhforia: European heliospheric forecasting information asset. *J. Space Weather Space Clim.*, *8*, A35. doi: 10.1051/swsc/2018020

Rappazzo, A., Matthaeus, W., Ruffolo, D., Velli, M., & Servidio, S. (2017). Coronal heating topology: The interplay of current sheets and magnetic field lines. *The Astrophysical Journal*, *844*(1), 87.

Rappazzo, A., & Velli, M. (2011). Magnetohydrodynamic turbulent cascade of coronal loop magnetic fields. *Physical Review E*, *83*(6), 065401.

Richardson, L. F. (1926, April). Atmospheric Diffusion Shown on a Distance-Neighbour Graph. *Proceedings of the Royal Society of London Series A*, *110*, 709-737. doi: 10.1098/rspa.1926.0043

Rowan, M. E., Sironi, L., & Narayan, R. (2017, November). Electron and Proton Heating in Transrelativistic Magnetic Reconnection. *The Astrophysical Journal*, *850*(1), 29. doi: 10.3847/1538-4357/aa9380

Ruffolo, D., Matthaeus, W. H., Chhiber, R., Usmanov, A. V., Yang, Y., Bandyopadhyay, R., ... Kasper, J. C. (2020, oct). Shear-driven transition to isotropically turbulent solar wind outside the alfvén critical zone. *The Astrophysical Journal*, *902*(2), 94. doi: 10.3847/1538-4357/abb594

Ruffolo, D., Matthaeus, W. H., & Chuychai, P. (2003, November). Trapping of Solar Energetic Particles by the Small-Scale Topology of Solar Wind Turbulence. *The Astrophysical Journall*, *597*, L169-L172. doi: 10.1086/379847

Ruffolo, D., Matthaeus, W. H., & Chuychai, P. (2004, October). Separation of Magnetic Field Lines in Two-Component Turbulence. *The Astrophysical Journal*, *614*, 420-434. doi: 10.1086/423412

Ruffolo, D., Pianpanit, T., Matthaeus, W. H., & Chuychai, P. (2012, March). Random Ballistic Interpretation of Nonlinear Guiding Center Theory. *The Astrophysical Journal Letters*, *747*, L34. doi: 10.1088/2041-8205/747/2/L34

Salu, Y., & Montgomery, D. (1977). Turbulent diffusion from a quasi-kinematical point of view. *The Physics of Fluids*, *20*(1), 1-3. doi: 10.1063/1.861690

Sanada, T., & Shanmugasundaram, V. (1992, June). Random sweeping effect in isotropic numerical turbulence. *Physics of Fluids A*, *4*(6), 1245-1250. doi:

10.1063/1.858242

Schatten, K. H. (1971, Jan). Large-scale properties of the interplanetary magnetic field. *Reviews of Geophysics and Space Physics*, *9*, 773-812. doi: 10.1029/RG009i003p00773

Schekochihin, A. A., Cowley, S. C., Dorland, W., Hammett, G. W., Howes, G. G., Quataert, E., & Tatsuno, T. (2009, May). Astrophysical Gyrokinetics: Kinetic and Fluid Turbulent Cascades in Magnetized Weakly Collisional Plasmas. *The Astrophysical Journal Supplement Series*, *182*(1), 310-377. doi: 10.1088/0067-0049/182/1/310

Schekochihin, A. A., Parker, J. T., Highcock, E. G., Dellar, P. J., Dorland, W., & Hammett, G. W. (2016, April). Phase mixing versus nonlinear advection in drift-kinetic plasma turbulence. *Journal of Plasma Physics*, *82*(2), 905820212. doi: 10.1017/S0022377816000374

Schwadron, N., & McComas, D. (2021). Switchbacks explained: Super-parker fields—the other side of the sub-parker spiral. *The Astrophysical Journal*, *909*(1), 95.

Servidio, S., Carbone, V., Dmitruk, P., & Matthaeus, W. H. (2011, December). Time decorrelation in isotropic magnetohydrodynamic turbulence. *EPL (Europhysics Letters)*, *96*, 55003. doi: 10.1209/0295-5075/96/55003

Servidio, S., Chasapis, A., Matthaeus, W. H., Perrone, D., Valentini, F., Parashar, T. N., ... Burch, J. (2017, Nov). Magnetospheric multiscale observation of plasma velocity-space cascade: Hermite representation and theory. *Phys. Rev. Lett.*, *119*, 205101. doi: 10.1103/PhysRevLett.119.205101

Servidio, S., Greco, A., Matthaeus, W. H., Osman, K. T., & Dmitruk, P. (2011, September). Statistical association of discontinuities and reconnection in magnetohydrodynamic turbulence. *Journal of Geophysical Research (Space Physics)*, *116*, A09102. doi: 10.1029/2011JA016569

Servidio, S., Haynes, C. T., Matthaeus, W. H., Burgess, D., Carbone, V., & Veltri, P. (2016, Aug). Explosive particle dispersion in plasma turbulence. *Phys. Rev. Lett.*, *117*, 095101. doi: 10.1103/PhysRevLett.117.095101

Servidio, S., Matthaeus, W., & Dmitruk, P. (2008). Depression of nonlinearity in decaying isotropic mhd turbulence. *Physical review letters*, *100*(9), 095005.

Servidio, S., Matthaeus, W. H., Shay, M. A., Cassak, P. A., & Dmitruk, P. (2009, March). Magnetic Reconnection in Two-Dimensional Magnetohydrodynamic Turbulence. *Physical Review Letters*, *102*(11), 115003. doi:

10.1103/PhysRevLett.102.115003

Servidio, S., Matthaeus, W. H., Shay, M. A., Dmitruk, P., Cassak, P. A., & Wan, M. (2010). Statistics of magnetic reconnection in two-dimensional magnetohydrodynamic turbulence. *Physics of Plasmas*, *17*. doi: 10.1063/1.3368798

Servidio, S., Valentini, F., Perrone, D., Greco, A., Califano, F., Matthaeus, W. H., & Veltri, P. (2015, January). A kinetic model of plasma turbulence. *Journal of Plasma Physics*, *81*(1), 325810107. doi: 10.1017/S0022377814000841

Shafranov, V. D. (1966, jan). Equilibrium of a three-dimensional plasma filament in a longitudinal magnetic field under steady conditions. *Journal of Nuclear Energy. Part C, Plasma Physics, Accelerators, Thermonuclear Research*, *8*(2), 207–212. doi: 10.1088/0368-3281/8/2/312

Shalchi, A. (2015). Perpendicular diffusion of energetic particles in collisionless plasmas. *Physics of Plasmas (1994-present)*, *22*(1), 010704.

Shalchi, A., Bieber, J., & Matthaeus, W. (2004). Nonlinear guiding center theory of perpendicular diffusion in dynamical turbulence. *The Astrophysical Journal*, *615*(2), 805.

Shalchi, A., & Dosch, A. (2008, October). Nonlinear Guiding Center Theory of Perpendicular Diffusion: Derivation from the Newton-Lorentz Equation. *The Astrophysical Journal*, *685*, 971-975. doi: 10.1086/591518

Shebalin, J. V., Matthaeus, W. H., & Montgomery, D. (1983, June). Anisotropy in MHD turbulence due to a mean magnetic field. *Journal of Plasma Physics*, *29*, 525-547. doi: 10.1017/S0022377800000933

Smith, C. W., Matthaeus, W. H., Zank, G. P., Ness, N. F., Oughton, S., & Richardson, J. D. (2001). Heating of the low-latitude solar wind by dissipation of turbulent magnetic fluctuations. *Journal of Geophysical Research: Space Physics*, *106*(A5), 8253–8272. doi: doi:10.1029/2000JA000366

Sonnerup, B. U. Ö., & Guo, M. (1996). Magnetopause transects. *Geophysical Research Letters*, *23*, 3679-3682. doi: 10.1029/96GL03573

Sonnerup, B. U. Ö., Hasegawa, H., Denton, R. E., & Nakamura, T. K. M. (2016, May). Reconstruction of the electron diffusion region. *Journal of Geophysical Research (Space Physics)*, *121*, 4279-4290. doi: 10.1002/2016JA022430

Sonnerup, B. U. Ö., Papamastorakis, I., Paschmann, G., & Lühr, H. (1987). Magnetopause properties from ampte/irm observations of the convection electric field: Method development. *Journal of Geophysical Research: Space Physics*,

*92*(A11), 12137-12159. doi: https://doi.org/10.1029/JA092iA11p12137

Sorriso-Valvo, L., Carbone, F., Leonardis, E., Chen, C. H. K., Šafránková, J., & Němeček, Z. (2017, March). Multifractal analysis of high resolution solar wind proton density measurements. *Advances in Space Research*, *59*(6), 1642-1651. doi: 10.1016/j.asr.2016.12.024

Subedi, P., Sonsrettee, W., Blasi, P., Ruffolo, D., Matthaeus, W., Montgomery, D., ... Chhiber, R. (2017, March). Charged particle diffusion in isotropic random magnetic fields. *The Astrophysical Journal*, *837*, 140. doi: 10.3847/1538-4357/aa603a

Tautz, R. C., & Shalchi, A. (2010). On the widespread use of the corrsin hypothesis in diffusion theories. *Physics of Plasmas*, *17*(12), 122313. doi: 10.1063/1.3530185

Taylor, G. I. (1922). Diffusion by continuous movements. *Proceedings of the London mathematical society*, *2*(1), 196–212.

Taylor, J. B. (1974). Relaxation of toroidal plasma and generation of reverse magnetic fields. *Physical Review Letters*, *33*(19), 1139.

Taylor, J. B., & McNamara, B. (1971, July). Plasma Diffusion in Two Dimensions. *Physics of Fluids*, *14*, 1492-1499. doi: 10.1063/1.1693635

Telloni, D., Bruno, R., D'Amicis, R., Pietropaolo, E., & Carbone, V. (2012). Wavelet analysis as a tool to localize magnetic and cross-helicity events in the solar wind. *The Astrophysical Journal*, *751*(1), 19.

Telloni, D., D'Amicis, R., Bruno, R., Carbone, F., Perrone, D., Zank, G. P., ... Adhikari, L. (2020). Detection capability of flux ropes during the solar orbiter mission. *The Astrophysical Journal Letters*, *899*(2), L25.

TenBarge, J. M., Howes, G. G., & Dorland, W. (2013, September). Collisionless Damping at Electron Scales in Solar Wind Turbulence. *The Astrophysical Journal*, *774*(2), 139. doi: 10.1088/0004-637X/774/2/139

Tessein, J., Matthaeus, W. H., Wan, M., Osman, K., Ruffolo, D., & Giacalone, J. (2013). Association of suprathermal particles with coherent structures and shocks. *The Astrophysical Journal Letters*, *776*(1), L8.

Tessein, J. A., Ruffolo, D., Matthaeus, W. H., & Wan, M. (2016). Local modulation and trapping of energetic particles by coherent magnetic structures. *Geophysical Research Letters*, *43*(8), 3620–3627.

Tessein, J. A., Ruffolo, D., Matthaeus, W. H., Wan, M., Giacalone, J., & Neugebauer, M. (2015, oct). Effect of coherent structures on energetic particle

intensity in the solar wind at 1 au. *The Astrophysical Journal*, *812*(1), 68. doi: 10.1088/0004-637x/812/1/68

Tooprakai, P., Seripienlert, A., Ruffolo, D., Chuychai, P., & Matthaeus, W. (2016). Simulations of lateral transport and dropout structure of energetic particles from impulsive solar flares. *The Astrophysical Journal*, *831*(2), 195.

Trenchi, L., Bruno, R., Telloni, D., D'amicis, R., Marcucci, M. F., Zurbuchen, T. H., & Weberg, M. (2013, may). Solar energetic particle modulations associated with coherent magnetic structures. *The Astrophysical Journal*, *770*(1), 11. doi: 10.1088/0004-637x/770/1/11

Usoskin, I. G., Schüssler, M., Solanki, S. K., & Mursula, K. (2005). Solar activity, cosmic rays, and earth's temperature: A millennium-scale comparison. *Journal of Geophysical Research: Space Physics*, *110*(A10). doi: https://doi.org/10.1029/2004JA010946

Valentini, F., Servidio, S., Perrone, D., Califano, F., Matthaeus, W., & Veltri, P. (2014). Hybrid vlasov-maxwell simulations of two-dimensional turbulence in plasmas. *Physics of Plasmas*, *21*(8), 082307.

Valentini, F., Trávníček, P., Califano, F., Hellinger, P., & Mangeney, A. (2007). A hybrid-vlasov model based on the current advance method for the simulation of collisionless magnetized plasma. *Journal of Computational Physics*, *225*(1), 753 - 770. doi: http://doi.org/10.1016/j.jcp.2007.01.001

Van Allen, J. A. (2000). On the modulation of galactic cosmic ray intensity during solar activity cycles 19, 20, 21, 22 and early 23. *Geophysical Research Letters*, *27*(16), 2453-2456. doi: https://doi.org/10.1029/2000GL003792

Vásconez, C. L., Pucci, F., Valentini, F., Servidio, S., Matthaeus, W. H., & Malara, F. (2015, December). Kinetic Alfvén Wave Generation by Large-scale Phase Mixing. *The Astrophysical Journal*, *815*(1), 7. doi: 10.1088/0004-637X/815/1/7

Velli, M., Grappin, R., & Mangeney, A. (1989, October). Turbulent cascade of incompressible unidirectional Alfvén waves in the interplanetary medium. *Physical Review Letters*, *63*(17), 1807-1810. doi: 10.1103/PhysRevLett.63.1807

Velli, M., Pucci, F., Rappazzo, F., & Tenerani, A. (2015, April). Models of coronal heating, turbulence and fast reconnection. *Philosophical Transactions of the Royal Society of London Series A*, *373*(2042), 20140262-20140262. doi: 10.1098/rsta.2014.0262

Veltri, P. (1999, March). MHD turbulence in the solar wind: self-similarity, intermittency and coherent structures. *Plasma Physics and Controlled Fusion*, *41*, A787-A795. doi: 10.1088/0741-3335/41/3A/071

Verbeke, C., Pomoell, J., & Poedts, S. (2019, July). The evolution of coronal mass ejections in the inner heliosphere: Implementing the spheromak model with EUHFORIA. *Astronomy & Astrophysics*, *627*, A111. doi: 10.1051/0004-6361/201834702

Verkhoglyadova, O. P., & Le Roux, J. A. (2005, October). Anomalous and classical diffusion of cosmic rays due to nonlinear two-dimensional structures and random magnetic fields. *Journal of Geophysical Research (Space Physics)*, *110*(A10), A10S03. doi: 10.1029/2004JA010871

Verscharen, D., Klein, K. G., & Maruca, B. A. (2019). The multi-scale nature of the solar wind. *Living Reviews in Solar Physics*, *16*(1), 5.

Verscharen, D., Parashar, T. N., Gary, S. P., & Klein, K. G. (2020, May). Dependence of kinetic plasma waves on ion-to-electron mass ratio and light-to-Alfvén speed ratio. *Monthly Notices of the Royal Astronomical Society*, *494*(2), 2905-2911. doi: 10.1093/mnras/staa977

Wan, M., Matthaeus, W. H., Roytershteyn, V., Parashar, T. N., Wu, P., & Karimabadi, H. (2016). Intermittency, coherent structures and dissipation in plasma turbulence. *Physics of Plasmas*, *23*(4), 042307. doi: 10.1063/1.4945631

Wan, M., Rappazzo, A. F., Matthaeus, W. H., Servidio, S., & Oughton, S. (2014). Dissipation and reconnection in boundary-driven reduced magnetohydrodynamics. *The Astrophysical Journal*, *797*(1), 63.

Wang, B., Kuo, J., Bae, S. C., & Granick, S. (2012). When brownian diffusion is not gaussian. *Nature materials*, *11*(6), 481.

Webb, D., Cliver, E., Crooker, N., St. Cyr, O., & Thompson, B. (2000). Relationship of halo coronal mass ejections, magnetic clouds, and magnetic storms. *Journal of Geophysical Research: Space Physics*, *105*(A4), 7491–7508. doi: 10.1029/1999JA000275

Winske, D. (1985, October). Hybrid simulation codes with application to shocks and upstream waves. *Space Science Review*, *42*, 53-66. doi: 10.1007/BF00218223

Woltjer, L. (1958). A theorem on force-free magnetic fields. *Proceedings of the National Academy of Sciences of the United States of America*, *44*(6), 489.

Yamada, M., Chen, L.-J., Yoo, J., Wang, S., Fox, W., Jara-Almonte, J., ... others (2018). The two-fluid dynamics and energetics of the asymmetric magnetic reconnection in laboratory and space plasmas. *Nature communications*, *9*(1), 5223. doi: 10.1038/s41467-018-07680-2

Yoo, J., Yamada, M., Ji, H., & Myers, C. E. (2013, May). Observation of ion acceleration and heating during collisionless magnetic reconnection in a laboratory plasma. *Phys. Rev. Lett.*, *110*, 215007. doi: 10.1103/PhysRevLett.110.215007

Yu, W., Farrugia, C. J., Lugaz, N., Galvin, A. B., Leitner, M., Moestl, C., ... Wilson, L. B., III (2014, December). On Modeling Flux Rope-type Small Interplanetary Transients by Non-Force Free Methods. *AGU Fall Meeting Abstracts*, SH31A-4105.

Zhao, L.-L., Zank, G. P., Adhikari, L., Hu, Q., Kasper, J. C., Bale, S. D., ... Klein, K. G. (2020, feb). Identification of magnetic flux ropes from parker solar probe observations during the first encounter. *The Astrophysical Journal Supplement Series*, *246*(2), 26. doi: 10.3847/1538-4365/ab4ff1

Zhdankin, V., Uzdensky, D. A., Werner, G. R., & Begelman, M. C. (2019, Feb). Electron and ion energization in relativistic plasma turbulence. *Phys. Rev. Lett.*, *122*, 055101. doi: 10.1103/PhysRevLett.122.055101

Zheng, J., & Hu, Q. (2018, January). Observational Evidence for Self-generation of Small-scale Magnetic Flux Ropes from Intermittent Solar Wind Turbulence. *The Astrophysical Journal Letters*, *852*, L23. doi: 10.3847/2041-8213/aaa3d7

Zheng, J., Hu, Q., Chen, Y., & Le Roux, J. (2017). Automated detection of small-scale magnetic flux ropes and their association with shocks. In *Journal of physics: Conference series* (Vol. 900, p. 012024).

Zhou, Y., Praskovsky, A. A., & Vahala, G. (1993, July). A non-Gaussian phenomenological model for higher-order spectra in turbulence. *Physics Letters A*, *178*(1-2), 138-142. doi: 10.1016/0375-9601(93)90740-Q

Zimbardo, G., Pommois, P., & Veltri, P. (2006, March). Superdiffusive and Subdiffusive Transport of Energetic Particles in Solar Wind Anisotropic Magnetic Turbulence. *The Astrophysical Journal Letters*, *639*(2), L91-L94. doi: 10.1086/502676